

ATTOSECOND TRANSIENT ABSORPTION SPECTROSCOPY
OF ATOMS AND MOLECULES

by

YAN CHENG

M.S., Kansas State University, 2011
B.S., University of Science and Technology of China, 2009

A dissertation submitted in partial fulfillment of the requirements
for the degree of Doctor of Philosophy
in the Department of Physics
in the College of Sciences
at the University of Central Florida
Orlando, Florida

Fall Term
2015

Major Professor: Zenghu Chang

ABSTRACT

One of the most fundamental goals of attosecond science is to observe and to control the dynamic evolutions of electrons in matter. The attosecond transient absorption spectroscopy is a powerful tool to utilize attosecond pulse to measure electron dynamics in quantum systems directly. In this work, isolated single attosecond pulses are used to probe electron dynamics in atoms and to study dynamics in hydrogen molecules using the attosecond transient absorption spectroscopy technique. The target atom/molecule is first pumped to excited states and then probed by a subsequent attosecond extreme ultraviolet (XUV) pulse or by a near infrared (NIR) laser pulse. By measuring the absorbed attosecond XUV pulse spectrum, the ultrafast electron correlation dynamics can be studied in real time. The quantum processes that can be studied using the attosecond transient absorption spectroscopy include the AC stark shift, multi-photon absorption, intermediate states of atoms, autoionizing states, and transitions of vibrational states in molecules. In all experiments, the absorption changes as a function of the time delay between the attosecond XUV probe pulse and the dressing NIR laser pulse, on a time scale of sub-cycle laser period, which reveals attosecond electron dynamics. These experiments demonstrate that the attosecond transient absorption spectroscopy can be performed to study and control electronic and nuclear dynamics in quantum systems with high temporal and spectral resolution, and it opens door for the study of electron dynamics in large molecules and other more complex systems.

ACKNOWLEDGMENTS

Today is October 4th, 2015, Sunday. The sunshine in Florida is beautiful, with the blue sky. Not too many people are around in the Physical Science building on a Sunday morning, and it is a good time to think about my stories since I came to the U.S. in 2009. Although I don't know where I will be landing after thirty or fifty years, I will never forget the wonderful people I have been working and staying with during the past six years, and they will be what really matters to me.

First I would like to thank my adviser and mentor Dr. Zenghu Chang who has been giving me enormous guidance, encouragement and help. Dr. Chang is extremely knowledgeable and has taught me how to conduct research effectively. Dr. Chang comes to the lab every day to discuss the experimental results and progress with us, and provides prompt feedback and suggestions. In addition, our weekly group meetings have provided me with great opportunities to discuss the experiments in depth with him and other colleagues, as well as enabled me to practice my presentation skill. Dr. Chang is also an excellent model for how to manage a research team and research projects.

The attosecond transient absorption experiments were mainly performed together with Dr. Michael Chini, Dr. He Wang and Dr. Xiaowei Wang. Dr. Chini taught me most of the experimental details of the attosecond transient absorption experiments, I learned a lot from him. In my heart Dr. Chini is my second mentor during the past six years. Dr. He Wang was the one who first introduced me to attosecond science, and has provided me numerous help in my research projects and in life. Dr. Xiaowei Wang helped me a lot with programming, Zemax and Solidworks. Dr. Chini, Dr. Xiaowei Wang and I spent many days and late nights in the lab to perform experiments. In addition, the theoretical simulations were contributed from Dr.

Fernando Martín, Dr. Alberto González-Castrillo, .Dr. Alicia Palacios, Dr. Luca Argenti, Dr. Xiao-Min Tong, Dr. Di Zhao, Dr. Dmitry Telnov, Dr. Peng-Cheng Li, Dr. John Heslar, Dr. Shih-I Chu, Dr. Feng He, Dr. Chang-Huang Zhang, Dr. Uwe Thumm, Dr. Suxing Hu.

I had the fortune to work with many excellent researchers in our research group. I would like to thank Dr. Kun Zhao who answered many of my questions, Dr. Sabih Kan and Max Moller, who worked with me on the 400 nm laser driven high harmonic ellipticity dependence experiment, Dr. Yi Wu, Eric Cunningham and Dr. Baozhen Zhao, who gave me tremendous help with lasers. I would like to acknowledge Dr. Qi Zhang, Dr. Shouyuan Chen, Dr. Yanchun Yin, Dr. Xiaoming Ren, Yang Wang, Jie Li, Andrew Chew, Julius Biedermann, Dr. Jianhua Zeng, Dr. Xianglin Wang, Peng Xu, Dr. Huaping Zang, who helped me massively in both the lab and my everyday life. In addition, I would like to thank my committee members Dr. Lee Chow, Dr. Haripada Saha and Dr. Eric W. Van Stryland.

Finally I would like acknowledge my parents and my wife, Dehui. This work could not have been done without their help, support, understanding and encouragement. Ever since high school, I have been living in schools and I do not see my parents often. I call them every other few days to share with them my life, my happiness and my sadness. Time goes by quickly and they are no long as young as they used to be. Although they may never understand the English I wrote here, I want to let them know how much I love them. My wife Dehui has been with me since my undergraduate years, we share each other's happiness and fight difficult times together. I cannot thank her enough for her support and confidence on me since I know sometimes how difficult it can be for her. There might be many more difficulties in the future, together we can do it!

This material is based upon work supported by the National Science Foundation, Department of Energy, Army Research Office, Air Force Office of Scientific Research, and the DARPA PULSE program by a grant from AMRDEC.

TABLE OF CONTENTS

| | |
|--|------|
| LIST OF FIGURES | viii |
| LIST OF TABLES | xvii |
| CHAPTER 1 - INTRODUCTION..... | 1 |
| 1.1 Principle of High Harmonic Generation (HHG)..... | 2 |
| 1.2 The Laser System..... | 5 |
| 1.3 Few-cycle Femtosecond Pulses | 7 |
| 1.4 Isolated Attosecond Pulse..... | 8 |
| 1.4.1 Polarization Gating | 9 |
| 1.4.2 Double Optical Gating | 11 |
| CHAPTER 2 - ATTOSECOND TRANSIENT ABSORPTION SPECTROSCOPY..... | 15 |
| 2.1 The Attosecond Transient Absorption Experimental Setup | 16 |
| 2.2 Theory of Attosecond Transient Absorption Spectroscopy..... | 28 |
| CHAPTER 3 - SUB-CYCLE ELECTRON DYNAMICS IN HELIUM AND NEON ATOMS . | 32 |
| 3.1 Sub-cycle Electron Dynamics in Helium..... | 32 |
| 3.2 Sub-cycle Electron Dynamics and Quantum Interferences of Attosecond Transient Absorption of Neon Atoms..... | 48 |
| CHAPTER 4 - ATTOSECOND TIME-RESOLVED AUTOIONIZATION OF ARGON AND KRYPTON ATOMS | 58 |
| 4.1 Attosecond time resolved autoionization of argon | 58 |
| 4.2 Quantum Beats in Attosecond Transient Absorption of Krypton Autoionizing States | 67 |
| CHAPTER 5 - COHERENT PHASE-MATCHED VUV GENERATION BY BELOW THRESHOLD HARMONIC GENERATION | 78 |
| 5.1 Below Threshold Harmonic Generation..... | 79 |
| 5.2 Coherent VUV Emission | 83 |
| 5.3 Phase Matching Mechanisms..... | 87 |
| CHAPTER 6 - ATTOSECOND TRANSIENT ABSORPTION SPECTROSCOPY IN HYDROGEN MOLECULES | 95 |
| 6.1 Excited Vibrational States of Molecular Hydrogen..... | 96 |
| 6.2 Simultaneous Observation of Electron and Nuclear Dynamics in Hydrogen Molecules... | 98 |

| | |
|--|-----|
| 6.3 Theoretical Simulation of Attosecond Transient Absorption Spectroscopy of Molecular Hydrogen | 102 |
| 6.4 Quantum Control in Attosecond Spectroscopy | 116 |
| CHAPTER 7 - FINAL REMARKS | 118 |
| APPENDIX A: LIST OF PUBLICATIONS | 120 |
| Peer-Reviewed Journal Publications | 121 |
| Invited Book Chapters | 123 |
| Invited talks..... | 124 |
| Selected Conference Presentations | 125 |
| APPENDIX B: COPYRIGHT PERMISSIONS | 126 |
| LIST OF REFERENCES | 136 |

LIST OF FIGURES

| | |
|---|----|
| Figure 1-1 The three step model for high harmonic generation. Adapted from [2] | 3 |
| Figure 1-2 Layout of the FAST laser system..... | 6 |
| Figure 1-3 The FAST laser amplified pulse spectrum..... | 7 |
| Figure 1-4 FROG retrieval of a 4 fs pulse from the FAST laser system and the hollow core fiber compressor | 8 |
| Figure 1-5 The ellipticity dependence of high harmonic generation yield. Adapted from [20] | 9 |
| Figure 1-6 Polarization gating scheme. Adapted from [22]. | 10 |
| Figure 1-7 Optical components for polarization gating. Adapted from [23]. | 11 |
| Figure 1-8 Attosecond pulse generation in polarization gating (a) and double optical gating (b). Adapted from [26]..... | 13 |
| Figure 1-9 Optic components for double optical gating. Adapted from [24] | 13 |
| Figure 1-10 Optics for creating the field for generalised double optical gating. Adapted from [27]..... | 14 |
| Figure 2-1 Schematic of the attosecond transient absorption setup. Adapted from [29]..... | 17 |
| Figure 2-2 (a) Top view of the XUV spectrometer. (b) Focal “plane” of the XUV grating for different incidence angles. Each plane covers a spectrum range from 11 nm (triangles) to 62 nm (squares), and the 40 nm components (circles) are also marked in each focal pl ane. For 86.5° incidence angle, the spectrum from 40 to 60 nm is approximately in a vertical plane (MCP plane). The axes are defined in (a).(c) Dependence of grating image distance of 40 nm XUV light on object distance and incidence angle. Adapted from [29]..... | 20 |
| Figure 2-3 Spatial profile of the focused spectrum on the MCP if the incident angle is set to be 86.5°. The six peaks (from left to right) are helium 1s2p, 1s3p, 1s4p absorption lines and argon 3s3p ⁶ 4p, 3s3p ⁶ 5p and 3s3p ⁶ 6p autoionization lines respectively. Both spatial and spectral FWHM is labeled for each peak. Adapted from [29] | 21 |
| Figure 2-4 (a) Transmission of XUV pulses through a 35 torr argon cell (red solid curve) or a 50 torr helium cell (blue curve with filled area). Five argon autoionization peaks and seven helium absorption dips are identified in the figure. (b) Wavelengths of the 12 spectral lines (squares) identified in (a), and the linear fitting (red dashed line). Adapted from [29]..... | 24 |

Figure 2-5 Comparison between measured absorption cross section (dots) and argon autoionization Fano profile convoluted by a Gaussian function with FWHM of 60 meV (solid curve). Adapted from [29] 26

Figure 2-6 Image of the electron distribution of a single microchannel pore, with corresponding lineouts (symbols) along the x (dispersion) and y (position) axes. Gaussian fits (solid curve) to the measured distribution give FWHM resolution of 131 μm and 151 μm along the x and y axes, respectively. The error comes from the Gaussian fit. Adapted from [29] 27

Figure 3-1 (a), Schematic of experimental setup for attosecond transient absorption. (b), Helium $1snp$ energy level diagram showing schematic XUV spectrum and states accessible for excitation by the attosecond pulse. (c), Measured absorbance spectrum as a function of the dressing laser intensity when the attosecond XUV pulse overlaps in time with the peak of the NIR laser pulse. The dotted lines trace the Stark-shifted absorption lines. At an intensity of $\sim 2.5 \times 10^{12} \text{ W/cm}^2$, several new absorption features appear in the vicinity of the $1s2p$ state, which dynamically evolve as the laser intensity is increased. Adapted from [48]. 34

Figure 3-2 Two-color multi-photon absorption in time-resolved absorption. The absorption in the vicinity of the $1s2p$ state at lower dressing laser intensities of a, $7 \times 10^{11} \text{ W/cm}^2$ and b, $5 \times 10^{12} \text{ W/cm}^2$ allow for experimental identification of the virtual states appearing in the laser-dressed absorption. Adapted from [48]. 37

Figure 3-3 (a), Schematic diagram of two-color two- and three-photon absorption pathways to the $1s3d$ (green), $1s4s$ (blue), and $1snp$ (red) excited states. The solid arrow indicates the single-photon excitation of the $1s2p$ and $1snp$ (red) states, whereas the dotted arrows indicate XUV absorption via two-color multi-photon excitation to $1snp$ states with $n \geq 6$. Dashed lines indicate absorption lines corresponding to laser-induced virtual states. (b), Normalized photoabsorption cross-sections based on TDSE simulation of helium when the attosecond XUV pulse overlaps in time with the peak of the NIR laser field. By removing the $1s2s$ and $1s4s$ states (blue) or $1s3s$ and $1s3d$ states (green) from the calculation, we can confirm that the additional absorption lines are due to multi-photon excitation to those excited states. Adapted from [48]. 38

Figure 3-4 a, Time-delay-dependent absorbance spectrum with a dressing laser intensity of 10^{13} W/cm^2 . With the strong dressing laser field, quantum-optical interferences can be observed in the absorption at negative delays. Near zero delay, the attosecond and NIR laser pulses

overlap, and the absorption is dominated by the sub-cycle AC Stark and ponderomotive energy level shifts. b, Absorbance lineouts in the vicinity of the transient virtual states. The absorbance (data points) was obtained by integrating the signal in the vicinity (± 50 meV) of the virtual intermediate states, and the error bars indicate the standard deviation of the absorbance in that region. The solid lines serve to guide the eye. While the absorbance near the $3s^-$, $3d^-$, $2s^+$, and $4s^-$ virtual states oscillates with half-cycle periodicities, the absorbance near the np^{2-} absorption feature oscillates with a quarter-cycle periodicity. Adapted from [48]. 40

Figure 3-5 Simulated time-delay-dependent absorbance spectrum with a dressing laser intensity of 10^{13} W/cm². The spectrogram can be divided into two regions to separate the effects of quantum-optical interferences and sub-cycle energy level dynamics. Adapted from [48]... 41

Figure 3-6 (a) Fourier transform analysis of region b in Figure 3-5, which spans $-40 fs < \tau_D < -20 fs$. The FT spectrogram obtained from the experimental data is shown in the left panel, while the right panel shows that obtained from the simulated data. The dashed 45-degree lines indicate the two-path quantum-optical interference. (b), Fourier transform analysis of region c, which spans $-13 fs < \tau_D < 7 fs$. Half- and quarter-cycle oscillations are evident above and below the ionization potential, and the oscillation frequency no longer follows the 45-degree lines associated with the two-path interference. Adapted from [48]. 42

Figure 3-7 Interference in the delay-dependent absorption near 19.68 eV with a dressing laser frequency $\omega_L = 1.7$ eV. The full calculation in (a) includes the contributions from 16 bound states, and the half-cycle interference oscillations are indicated by the yellow box. In (b), the calculation has been repeated after removing the $1s2p$, $1s4p$, $1s5p$, $1s6p$, and $1s7p$ states. The presence of the interference oscillation near 19.68 eV suggests that it does not result from quantum “which-way” interference, as no “direct” pathway is possible. In (c) the power spectrum $P\omega^2$ of the atomic dipole radiation is plotted for the same conditions as in (a), with all states included. The lack of the interference oscillations indicates an optical interference mechanism, as explained in the text. 44

Figure 3-8 Comparison of “which-way” and optical interference models. (a) In the “which-way” interference, the final state can be excited both by the attosecond pulse alone (“direct”) and by the combined attosecond and NIR laser fields (“indirect”). Each of these excitation

pathways induces a time-dependent dipole, $P_{dir}(\omega_2)$ and $P_{ind}(\omega_2)$ respectively, which both oscillate with the frequency $\omega_2 = E_f - E_0$. Depending on the delay, these two components may add up constructively or destructively, leading to a modulation of the measured signal. (b) In the optical interference, there is no state with energy E_f , and therefore the component of the attosecond spectrum (pale blue shaded) with frequency ω_2 does not induce dipole emission on its own. When the NIR laser is present, the state with energy E_i forms sidebands resulting in the emission with frequency ω_2 . This laser-induced dipole radiation (“emitted”) will interfere with the “transmitted” components of the attosecond spectrum with frequency ω_2 , leading to a delay-dependent modulation in the measured signal. Blue arrows indicate atomic transitions initiated by the attosecond pulse (with spectrum indicated by the pale blue shaded area), while red arrows indicate transitions resulting from the NIR pulse. Magenta sinusoidal arrows indicate the dipole emission with frequency ω_2 , while the pale blue sinusoidal arrow indicates the transmitted component of the attosecond spectrum. 47

Figure 3-9 Measured absorption cross section of neon atoms (black curve with gray filled area) and atomic energy levels of interest. The electron configurations are marked for each identified. Adapted from [63] 49

Figure 3-10 Measured delay-dependent absorbance spectra with a dressing laser intensity of (a) $\sim 10 \text{ TW/cm}^2$ and (b) $\sim 75 \text{ TW/cm}^2$ (b). Panels (c) and (d) show the calculated absorption cross sections for dressing laser pulses 4 fs in duration and with the same intensities as in panels (a) and (b). Adapted from [63]..... 51

Figure 3-11 Diagram of direct and indirect pathways resulting in quantum interferences in the (a) 3s and (b) 4p⁺ absorption lines. Energy levels indicated by black lines are accessible by one XUV photon absorption, while gray levels are forbidden by selection rules. Dashed gray energy levels in (b) indicate Floquet-like sidebands of the 4p energy level. Adapted from [63]..... 53

Figure 3-12 Measured absorption cross sections in the vicinity of the 3s (black) and 4p⁺ (gray) absorption lines. The dots indicate the experimentally obtained data points, whereas the solid lines are smoothed to show the major features. Whereas half-cycle ($\sim 1.3 \text{ fs}$) oscillations can be observed in the 3s absorption lines extending to large negative delays,

| | |
|--|----|
| oscillations in the $4p^+$ absorption can only be observed for delays between 0 and -7 fs. | |
| Adapted from [63]..... | 55 |
| Figure 3-13 Measured (a) and calculated (b) delay-dependent absorbance spectrum with isolated attosecond pulses filtered by indium filter which allows transmission of XUV pulses within the spectrum range from 11 eV to 17 eV. Autler-Town splitting instead of quantum interference was observed. Adapted from [63]..... | 56 |
| Figure 4-1 Energy diagram of the $3s3p^6np$ 1P autoionizing states in argon. The continuum spectrum of the attosecond pulse covers the 1P series of states. Adapted from [5]..... | 60 |
| Figure 4-2 Transmitted XUV spectrum indicating argon $3s3p^6np$ 1P autoionizing states. The spectrometer resolution was 50 meV. Adapted from [5]..... | 61 |
| Figure 4-3 Transmitted attosecond XUV spectra of argon in a strong NIR laser field with a peak intensity of (a) 5×10^{11} W/cm ² and (b) 10^{12} W/cm ² . Negative delays correspond to the attosecond pulse arriving on the target before the NIR laser pulse. The resonance peaks are shifted, broadened, and weakened when the two pulses overlap. (c), (d) Transmitted signal (solid) near the $3s3p^64p$ and $3s3p^65p$ states for 5×10^{11} W/cm ² and 10^{12} W/cm ² , respectively, and calculated exponential decay convoluted with 4.5 fs Gaussian for best fit (dashed). Adapted from [5]..... | 63 |
| Figure 4-4 (a) Schematic representation of argon autoionizing states exposed to the strong NIR laser field. The blue arrows indicate the attosecond XUV excitation of the ground state to the $3s3p^6np$ 1P states as well as to the $Ar^+(3s^23p^5\epsilon l)$ continuum. The red arrows indicate the NIR laser coupling between the autoionizing states and the $Ar^{*+}(3s3p^6\epsilon l)$ continuum or to $3s3p^6nl$ autoionizing states. The configuration interaction (green arrows) couples all autoionizing states to the Ar^+ continuum. (b) Autoionization decay modified by NIR laser-induced coupling to the $Ar^{*+}(3s3p^6\epsilon l)$ continuum. Ionization by the NIR field truncates the autoionization decay, resulting in a shorter lifetime and a broader, shifted resonance peak. (c) Autoionization decay modified by NIR laser-induced coupling to $3s3p^6nl$ autoionizing states. Rabi oscillation between the two states results in AC Stark-like splitting. Adapted from [5]. | 64 |
| Figure 4-5 Simulated dipole radiation spectrum of laser-induced coupling of the $3s3p^64p$ and $3s3p^64d$ autoionizing states. The XUV laser had a pulse duration of 140 as and intensity of | |

| | |
|---|----|
| 10 ¹⁰ W/cm ² . The NIR laser had a pulse duration of 8 fs and intensity of (a) 5×10 ¹¹ W/cm ² and (b) 10 ¹² W/cm ² . Adapted from [5]. | 66 |
| Figure 4-6 Quantum beats in the delay-dependent absorption near the 1s2p excited state with a reduced excited state basis set consisting of the 1s2p, 1s3s, 1s5p, and 1s6p states. Relatively slow oscillations are present on the high-energy side of the 1s2p absorption line in (a) with periodicity equal to that of the quantum beating of the 1s5p and 1s6p state (white curve). The integrated absorbance from 21.25 to 21.28 eV in (b) clearly shows the quantum beat effect with a periodicity of 25.83 fs. Adapted from [77]. | 68 |
| Figure 4-7 Fourier transform analysis of the quantum beats in the vicinity of the 1s2p excited state. (a) For the reduced basis set, the dominant quantum beat arises from the 1s5p and 1s6p states. (b) When the full 16-state basis set is used, additional beat frequencies corresponding to each of the 1snp energy level differences $\Delta E_{n' p, np} = E_{n' p} - E_{np}$ can be observed. Adapted from [77]. | 69 |
| Figure 4-8 The atomic absorption cross section of krypton vs wavelength. Adapted from [78]. | 70 |
| Figure 4-9 The attosecond pulse spectrum with a 200 nm thick indium filter. | 71 |
| Figure 4-10 The measured transmitted attosecond VUV spectra of krypton as a function of the time delay between the isolated attosecond pulse and a NIR pulse with a peak intensity of 5×10 ¹² W/cm ² . Adapted from [79]. | 73 |
| Figure 4-11 The measured transmitted attosecond VUV spectra of krypton as a function of the time delay between the isolated attosecond pulse and a NIR pulse in the energy range of 14 – 15 eV with a peak intensity of 5 × 10 ¹² W/cm ² . Adapted from [79]. | 74 |
| Figure 4-12 the Fourier transform analysis of the measured time dependent transmitted attosecond VUV spectra of krypton. | 75 |
| Figure 4-13 The simplified model calculation that includes the ground state, the 5p and 7d state and three autoionizing states. | 76 |
| Figure 4-14 The calculated transmitted attosecond VUV spectra of krypton as a function of the time delay between the isolated attosecond pulse and a NIR pulse in the energy range of 14 – 15 eV. | 77 |
| Figure 5-1 Measured harmonic spectrum with an intensity of (3.3±0.3)×10 ¹³ W/cm ² and a target pressure-length product of 10 torr-mm. The spectrum is characterized by coherent line emissions (e.g.; RESs A and B) consistent with the labelled 3p ⁶ →3p ⁵ ns and 3p ⁵ nd | |

| | |
|---|----|
| resonances of argon (indicated by vertical white lines) in addition to the broadband high harmonics (e.g.; the 11 th harmonic, H11). Adapted from [95]. | 80 |
| Figure 5-2 Evolution of the resonance-enhanced structures with driving laser intensity. At low intensities (top), the resonance-enhanced structures dominate the spectrum, whereas the harmonics dominate at higher intensities (bottom). Adapted from [95]. | 82 |
| Figure 5-3 Argon and neon exhibit resonance-enhanced structures in the below-threshold harmonics generation, whereas the harmonics generated in xenon are structureless above the ionization threshold. Bound state resonances within the photon energy ranges of interest are indicated. Adapted from [95]. | 83 |
| Figure 5-4 a, Both the RESs (here, A and B) and the above-threshold harmonics exhibit narrow divergence angles of ~3 mrad FWHM, indicating laser-like spatial coherence of the VUV line emission. b, The efficiency of the coherent line emission depends strongly on the ellipticity of the driving laser, and indicates a sub-cycle generation mechanism. The ellipticity dependence is much stronger than that expected from recollision (blue solid line), but is consistent with harmonic generation during tunneling. Adapted from [95]. | 85 |
| Figure 5-5 The RESs exhibit a strong dependence on the carrier-envelope phase when the VUV generation is confined to a single half-cycle of the driving laser. Adapted from [95]. | 86 |
| Figure 5-6 The intensity of the RESs located at 14.05 eV (top), 14.80 eV (middle) and 15.30 eV (bottom) exhibits a 2π periodicity under the DOG, whereas much smaller changes are observed with the CEP for linearly polarized 5 fs pulses. Adapted from [95]. | 87 |
| Figure 5-7 a, The coherent VUV emission in the vicinity of the RESs scales quadratically with the target gas pressure-length product, indicating perfect phase-matching. The 11 th harmonic (H11) scales quadratically up to a pressure-length product of only ~20 torr-mm, due to the strong absorption cross-section of the neutral gas for photon energies just above the ionization threshold. Calibrated energy measurements of the RESs are indicated by open gray stars. b, Numerical simulation of the VUV emission in argon indicates that the phase-matching process results in spectrally narrow, energy-shifted RESs when compared with the single-atom emission. The shift of the phase-matched RESs relative to the bound state energies is indicated in the inset. Adapted from [95]. | 89 |
| Figure 5-8 Argon exhibits regions of anomalous dispersion (gray shading) in the vicinity of the atomic resonances, just above the resonance energies. Adapted from [95]. | 92 |

Figure 5-9 Since the amount of negative dispersion increases with the pressure, the phase-matched photon energy moves away from the resonance energy, and the RESs tend to shift to higher energy with increasing pressure. The dashed red lines represent a cubic spline fit of the most prominent RES peak energies. Adapted from [95]. 93

Figure 5-10 As the target pressure increases, the phase-matching occurs at higher energies and the RESs are observed to shift in energy. Adapted from [95]. 94

Figure 6-1 Attosecond absorption in neutral hydrogen molecules. a, the bound state manifold. The electronic and nuclear dynamics are encoded in the transient changes of the absorption lines with state selectivity. b, Absorption lines corresponding to the $B^1\Sigma_u^+ \leftarrow X^1\Sigma_g^+$, $C^1\Pi_u \leftarrow X$, and $D^1\Pi_u \leftarrow X$ bands of neutral hydrogen molecules can be observed in the attosecond spectrum. c, The spectral range of the attosecond VUV pulse was selected by using an indium foil filter 98

Figure 6-2 Experimentally measured time delay-dependent absorbance spectrum of hydrogen molecules. In the ***B1Σu*** state, absorption lines show fast oscillations with half the laser cycle period, while absorption line splitting and shifting are observed in ***C1Πu*** and ***D1Πu*** states, such features are attributed to electronic dynamics. These features revive as slow variations on the time scale of nuclear vibration. By performing the attosecond transient absorption experiment in hydrogen molecules, both the electronic and nuclear dynamics can be observed simultaneously. 100

Figure 6-3 ATAS reveals state-resolved electronic and nuclear dynamics. a, the measured delay dependent absorption spectrum of hydrogen molecules near delay zero. b, the ab initio quantum simulations. c and d are the measured and simulated delay dependent absorption spectrum in the vicinity of $C^1\Pi_u$ states, e and f are the measured and simulated delay dependent absorption spectrum near $B^1\Sigma_u^+$ states. Model calculations including only the $X^1\Sigma_g^+$ ground state and d, the $C^1\Pi_u$ and $J^1\Delta_g$ and f, $B^1\Sigma_u^+$ and $GK^1\Sigma_u^+$ excited states, reveal the mechanism behind the state-resolved absorption features. 103

Figure 6-4 Fourier transform analysis of measured (a) and simulated (b) delay dependent absorption spectrum. Quantum beats in the delay dependent absorption spectrum can be observed as crossings of Fourier lines associated with different laser-perturbed vibrational states. Consecutive vibrational levels cross when the Fourier frequency is equal to half of

| | |
|--|-----|
| their energy differences (blue stars), while intersections at larger Fourier frequencies indicate higher-order crossings (red stars)..... | 106 |
| Figure 6-5 Plot of the polarization in the time and energy domain for a single vibrational state. | 107 |
| Figure 6-6 ATAS spectrum obtained from the analytical model. Upper panel: only the $v=0$ state is included. Central panel: only $v=0$ and $v=1$ states are included. Bottom panel: all v 's are included. Adapted from [121]..... | 110 |
| Figure 6-7 ATAS spectrum obtained from the reduced TDSE calculations. Upper panel: only the $v=0$ state is included. Central panel: only $v=0$ and $v=1$ states are included. Bottom panel: all v 's are included. Adapted from [121]..... | 111 |
| Figure 6-8 Eigenvalues of the Floquet matrix as a function of IR intensity. Adapted from [121] | 113 |
| Figure 6-9 ATAS spectrum obtained from the reduced TDSE calculations. The intensity of the IR pulse is 10 times larger than that of Figure 6-7. Adapted from [121]..... | 114 |
| Figure 6-10 Left panel: Chirped and unchirped pulses used in the calculations. Right panel: Fourier transform of the two pulses. Adapted from [121]..... | 115 |
| Figure 6-11 ATAS spectrum obtained from the reduced TDSE calculations using the chirped pulses. Adapted from [121]..... | 115 |
| Figure 6-12 Quantum control in attosecond photochemistry. A weak, few-cycle NIR “control” pulse, which overlaps in time with the VUV attosecond pulse, modifies the attosecond excitation dynamics. The strong modulation of the ATAS indicates the modification of the initial wavepacket, suggesting a mechanism for attosecond quantum control. | 117 |

LIST OF TABLES

Table 2-1 Spectrum lines used to calibration the spectrometer. Adapted from [29] 23

CHAPTER 1 - INTRODUCTION

Over the last five decades, the development of ultrafast laser technology created new time scale for experimental observations [1, 2]. Molecular vibrations occur on a time scale of tens to hundreds of femtoseconds, and this is the characteristic time scale for the motion of atoms in molecules. The nuclear motion in molecules has been studied extensively by using the femtosecond pump-probe spectroscopy technique [3]. The motion of electrons in matter occurs on the attosecond time scale ($1 \text{ as} = 10^{-18} \text{ s}$). For example, the time it takes one electron in the first Bohr orbit to travel a Bohr radius is 24.2 as. Using femtosecond pump-probe spectroscopy technique is insufficient to track the dynamic evolution of electrons in matter. To study the fast electron dynamics in atoms and molecules, a light pulse shorter than the dynamics process itself is needed, and for this reason, an attosecond light source is required to study the electron dynamics. In recent years, advances of attosecond science has opened the new way for understanding and controlling ultrafast electron dynamics in atoms and molecules [4].

The attosecond transient absorption spectroscopy is a powerful tool [5] to utilize attosecond pulse for direct measurement of electron dynamics in quantum systems. In this thesis, I will discuss the generation of attosecond pulses, the fundamental principles and experimental setup of the attosecond transient absorption spectroscopy technique, and some experiments utilizing the technique to study the electron dynamics in helium, neon atoms, and in hydrogen, deuterium molecules.

The overall goal of my work is to study the electron dynamics in atoms and molecules using the attosecond transient absorption spectroscopy technique. This thesis will be organized as follows. Chapter one will be the discussion of high harmonic generation and gating techniques used to generate single attosecond pulses, including the polarization gating, double optical gating

and generalized double optical gating. In Chapter Two, I will discuss the experiment setup and theory of attosecond transient absorption spectroscopy. In Chapter Three, Four and Six, I will present the measurement of bound state electron dynamics in helium and neon atoms, autoionizing states dynamics in argon and krypton atoms, and the molecular dynamics in hydrogen and deuterium molecules. Chapter Five will be the below threshold harmonics generation. Chapter Seven will be the final remarks.

1.1 Principle of High Harmonic Generation (HHG)

Ferray et al [6] discovered high harmonic generation (HHG) in 1988 by focusing a Nd:YAG laser at 1064 nm central-wavelength to an intensity of $10^{13} \sim 10^{14} \text{ W/cm}^2$ in a noble gas target. The high harmonic generation radiation has very good temporal coherence [7] which makes it a good way to generate broadband XUV sources.

When an atomic or molecular medium is exposed to an intense femtosecond laser whose peak electric field strength is comparable to the Coulomb field, a train of attosecond pulses is generated through the process of high harmonic generation. This process was explained using the so-called three step model in a semi-classical way in 1994 [8]. First, the valence electron tunnels through the atomic potential barrier created by the ion charge and the applied strong oscillating laser electric field. After tunneling, the electron is accelerated in the laser field. The freed electron travels in the external laser field like a classical particle and one can calculate the electron's trajectory using Newton's law when two conditions, first introduced by Keldysh [9], are met. First, after the electron is liberated from the atom, it is no longer affected by the Coulomb potential of the atom. Second, during the evolution only the ground state of the atom is

considered. In the third step, a portion of the electrons recombines with the parent ion, producing an XUV photon. The three step model can be understood in a schematic of the model as shown in the figure below.

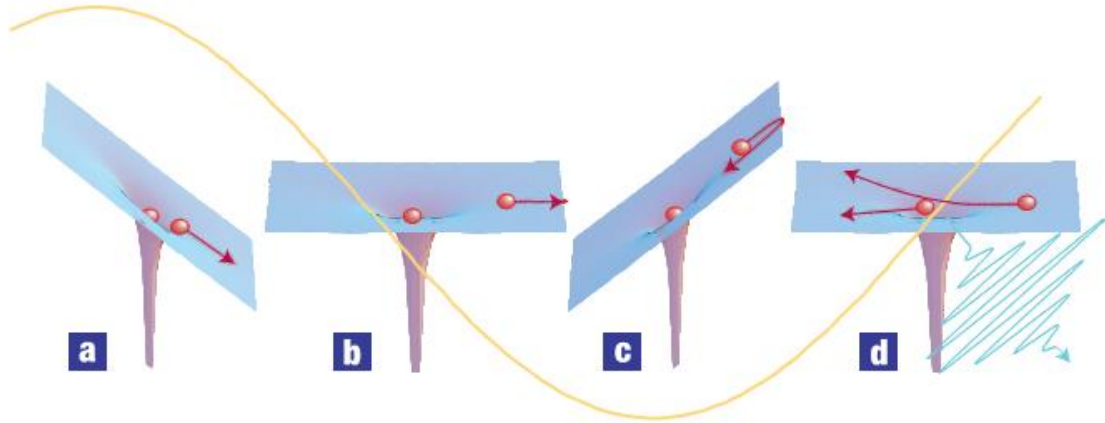


Figure 1-1 The three step model for high harmonic generation. Adapted from [2]

For simplicity, we consider the system moving in one dimension only, and assume the laser field to be monochromatic and linearly polarized [10]. The electric field is given by

$$\varepsilon(t) = E_0 \cos(\omega_0 t) \quad (1-1)$$

When the electron is released, its initial position is at $x_0 = 0$ and its initial velocity is $v_0 = 0$. We have assumed that the electron leaves the barrier with zero velocity, however, quantum mechanics never allows such precision [2]. The ionization process is assumed to be instantaneous. The electron is then affected by the laser field only and the Coulomb potential is neglected. Under the two conditions we discussed above, we can treat the electron classically and calculate the electron trajectory by using Newton's law. The equation of motion of the electron is

$$\frac{d^2x}{dt^2} = -\frac{e}{m_e} \varepsilon(t) = -\frac{e}{m_e} E_0 \cos(\omega_0 t) \quad (1-2)$$

where e and m_e are the electron charge and mass respectively.

Assuming the electron is freed at time t_0 , the solution of the differential equation is

$$v(t) = -\frac{eE_0}{m_e\omega_0} [\sin(\omega_0 t) - \sin(\omega_0 t_0)] \quad (1-3)$$

where $v(t)$ is the velocity of the electron.

When the electron returns to the parent ion, its position is at $x(t) = 0$, and using (2-3), the return time t_f can be found by solving the equation

$$x(t_f) = \frac{eE_0}{m_e\omega_0} \{[\cos(\omega_0 t_f) - \cos(\omega_0 t_0)] + \omega_0 \sin(\omega_0 t_0) (t_f - t_0)\} = 0 \quad (1-4)$$

The emitted photon energy is

$$\hbar\omega_X = I_p + 2U_p [\sin(\omega_0 t_f) - \sin(\omega_0 t_0)]^2 \quad (1-5)$$

where I_p is the ionization potential of the atom and $U_p = \frac{e^2 E_0^2}{4m\omega^2}$ is the pondermotive energy which is the average quivering energy the electron gains in the laser electric field.

Equation (1-5) does not have analytical solutions. We can solve the equation numerically. This solution can be fitted with an analytical function

$$\frac{t_f}{T_0} = \frac{1}{4} - \frac{3}{2\pi} \sin^{-1} \left(4 \frac{t_0}{T_0} - 1 \right) \quad (1-6)$$

We know that $\omega_0 = 2\pi/T_0$, Equation (1-6) can be rewritten as

$$\omega_0 t_f = \frac{\pi}{2} - 3 \sin^{-1} \left(2 \frac{\omega_0 t_0}{\pi} - 1 \right) \quad (1-7)$$

Plug (1-7) into (1-5), we have

$$\hbar\omega_x = I_p + 2U_p \left[\cos \left(3 \sin^{-1} \left(2 \frac{\omega_0 t_0}{\pi} - 1 \right) \right) - \sin(\omega_0 t_0) \right]^2 \quad (1-8)$$

And from (1-8) we can find that the highest released photon energy is

$$E_{cutoff} = I_p + 3.17U_p \quad (1-9)$$

when the electron is released at $\omega_0 t_0 = 0.05 \times 2\pi$ and returns at $\omega_0 t_f = 0.7 \times 2\pi$.

High harmonic generation process can also be understood quantum mechanically [11], however, the three step model is intuitive and convenient to use in experiments.

The HHG radiation is intrinsically an attosecond process and it occurs once every half laser cycle. For a multi-cycle driving laser pulse, a train of attosecond pulses will be generated with an interval of half an optical cycle. While attosecond pulse trains are useful in some applications [12-14], isolated single attosecond pulses are more desirable for experimentalists to perform pump-probe experiments to study electron dynamics in atoms and molecules and map out the time evolution of the system, especially for the cases where the pulse spacing (half an optical cycle) is shorter than the physical process to be studied.

1.2 The Laser System

The attosecond transient absorption experiments are performed using the Florida Attosecond Science and Technology (FAST) laser, which is a two-amplification-stage chirped pulse amplifier (CPA) laser system [15] as shown in the figure below. The first amplification stage is a multi-pass amplifier in which the seed pulse passes through the cryogenically-cooled [16] Ti:Sapphire crystal 14 times. Amplified spontaneous emission (ASE) is suppressed due to the geometry configuration. In the second amplification stage, the seed pulse pass through a

second cryogenically-cooled Ti:Sapphire crystal once. After the amplification, the pulses are compressed by a pair of grating.

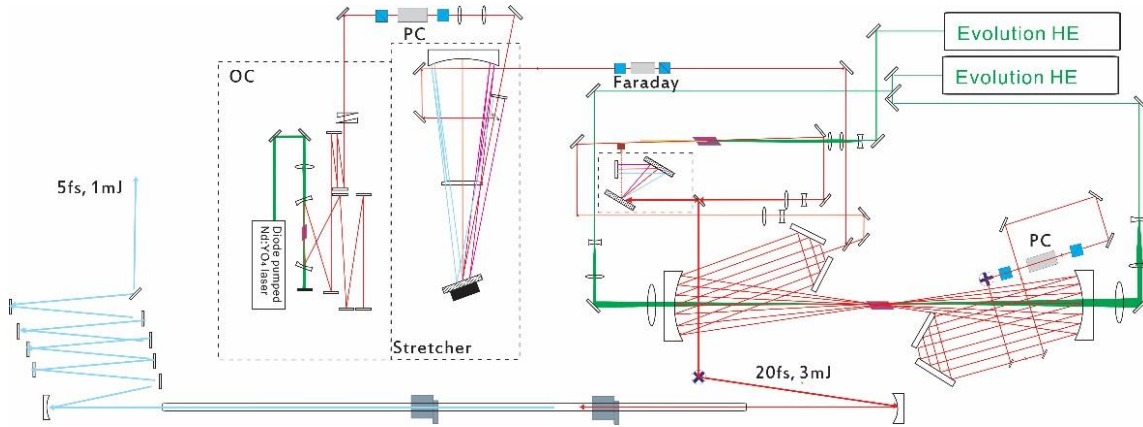


Figure 1-2 Layout of the FAST laser system

The spectrum of the amplified laser pulses is shown in the figure below, the spectrum covers from 725 nm to 830 nm. The laser system delivers laser pulses with energy up to 3 mJ. The central wavelength is 780 nm and the pulse duration is 20 fs. The amplified pulses are further sent into a hollow core fiber compressor to compress the pulse to be few-cycle in order to generate single attosecond pulses more efficiently. We will discuss the few-cycle femtosecond pulse generation in the next session.

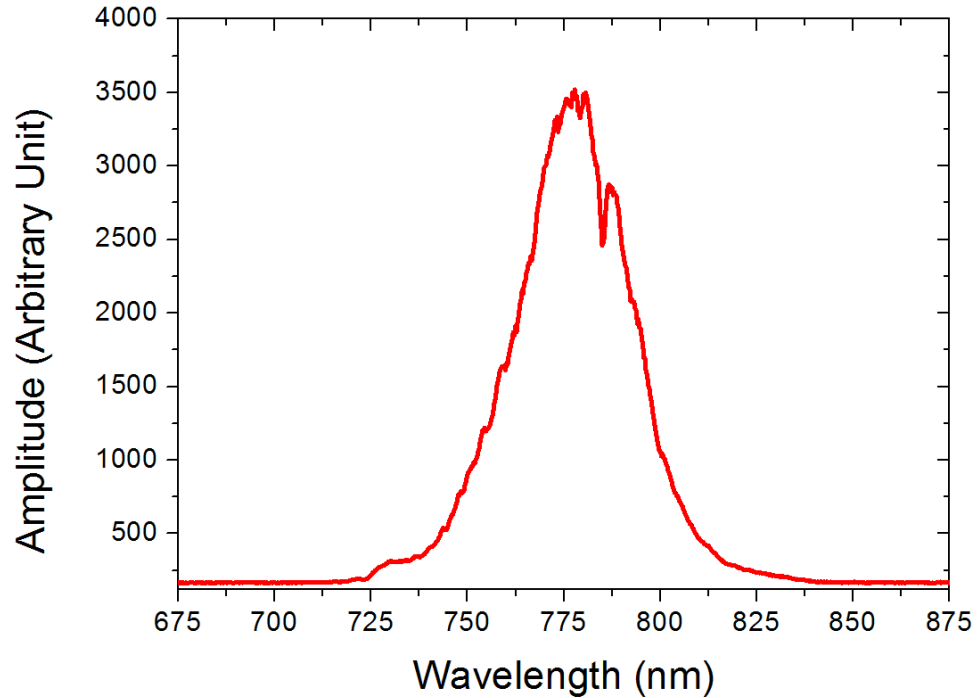


Figure 1-3 The FAST laser amplified pulse spectrum

1.3 Few-cycle Femtosecond Pulses

To produce few cycle femtosecond pulses, the multi-cycle pulses from the laser are sent into a neon gas-filled hollow core fiber [17] and a chirped mirror compressor [18]. Inside the hollow core fiber, the pulse spectral bandwidth is broadened due to the self-phase modulation [19] process in nonlinear optical media, neon in our case. The positive chirp introduced by the self-phase modulation process and material dispersion is compensated by using chirped mirrors. 1 mJ pulses as short as 4-6 fs centered at 730 nm are generated after the hollow core fiber and chirped mirror compressors. A FROG measurement of a compressed pulse from the FAST laser is shown in Figure 1-4.

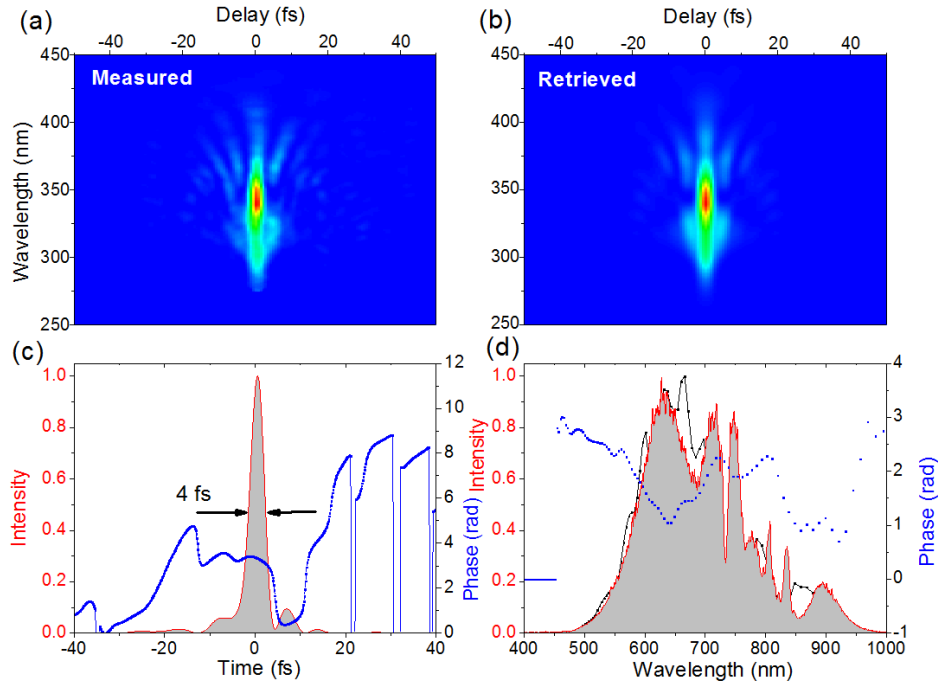


Figure 1-4 FROG retrieval of a 4 fs pulse from the FAST laser system and the hollow core fiber compressor.

1.4 Isolated Attosecond Pulse

When intense linearly polarized near infrared (NIR) laser pulses are focused in to a noble gas target, a train of attosecond pulses can be generated every half a laser cycle through the high harmonic generation process. Attosecond pulse trains are useful for some experiments, however, in order to study electron dynamics in atoms and molecules through pump-probe experiments, single attosecond pulses are more desirable. In this session, we will discuss different methods to generate isolated single attosecond pulses.

1.4.1 Polarization Gating

The high harmonic generation process strongly depends on the ellipticity of the driving pulses [20]. As the ellipticity of the driving pulses increases, high harmonic generation efficiency drops off dramatically. This ellipticity dependence can be explained using the three-step model [21]. The figure below shows the typical dependence of high harmonic generation yield as a function of driving laser field ellipticity. The high harmonic yield drops significantly as the ellipticity increases.

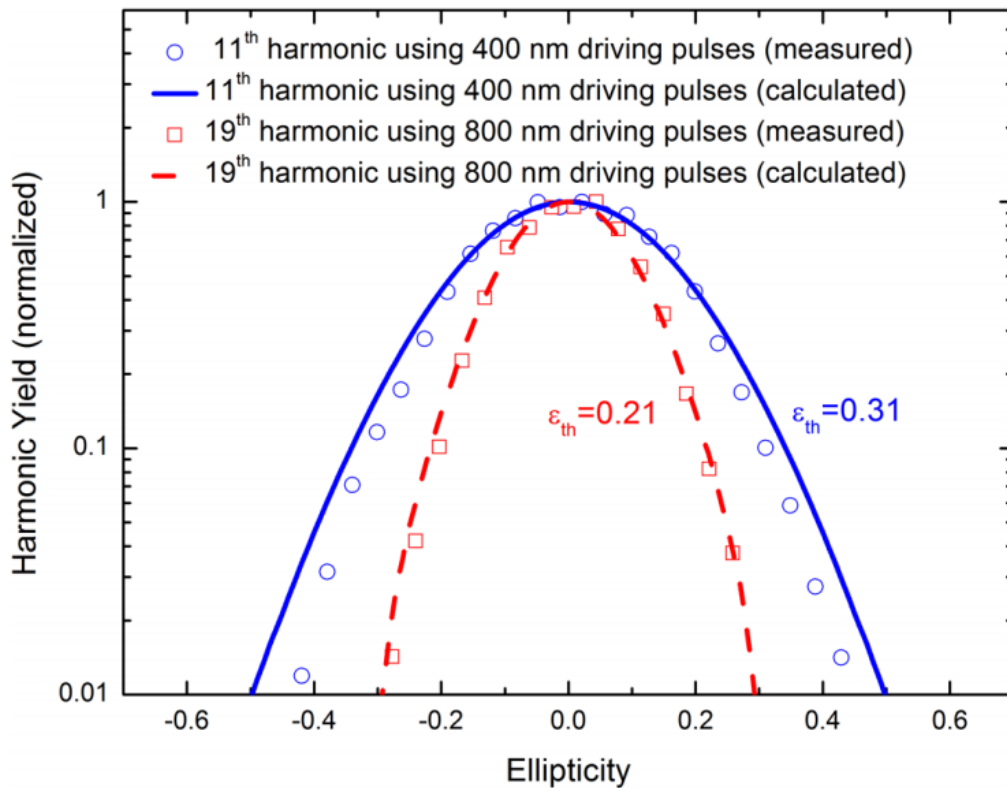


Figure 1-5 The ellipticity dependence of high harmonic generation yield. Adapted from [20]

In the polarization gating, in order to create a temporal gate, the polarization of the driving laser pulses changes from circularly polarized to linearly polarized and then changes back to circularly polarized again. Since the HHG radiation process occurs every half an optical cycle, in order to generate single attosecond pulses, the gate width should be equal or smaller to

the spacing between adjacent attosecond pulses, which is half a laser cycle. By combining a right circularly polarized and a left circularly polarized laser pulse with a time delay between them, we can create a pulse whose leading and trailing edges are circularly polarized and central part is linearly polarized. This is shown in the figure below.

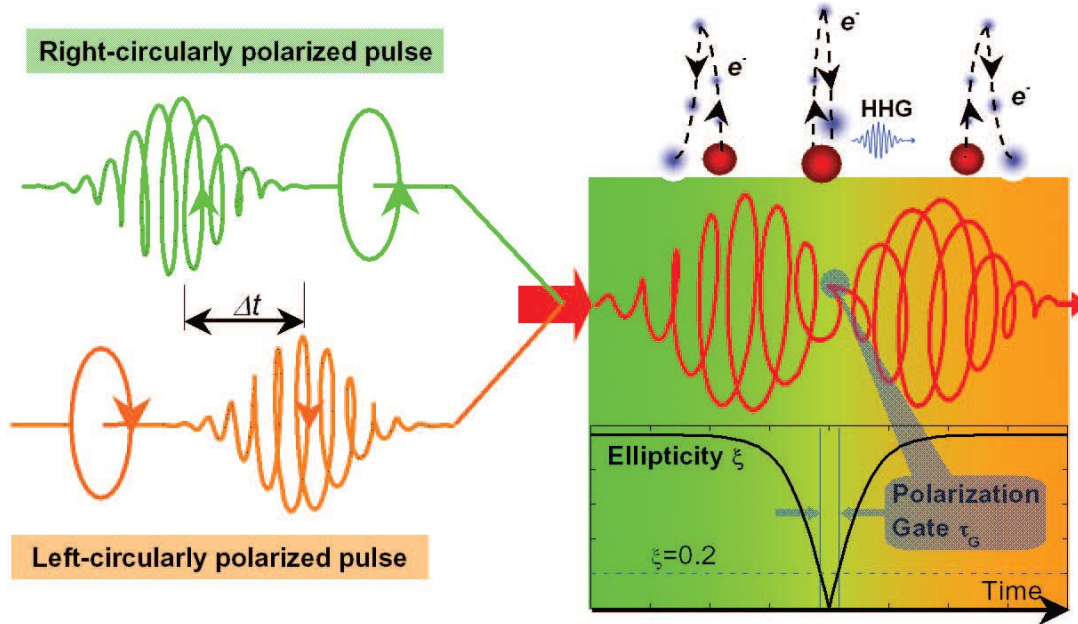


Figure 1-6 Polarization gating scheme. Adapted from [22].

The width of the temporal gate can be written as:

$$\delta t_G = \frac{\xi_{thr}}{\ln 2} \frac{\tau_L^2}{T_D} \quad (1-10)$$

where ξ_{thr} is the so-called threshold ellipticity at which the high harmonic yield becomes very small, usually $\xi_{thr} = 0.2$, τ_L is the pulse duration of the drive laser and T_D is the time delay between the two pulses. For polarization gating, the temporal gating width is half a laser cycle. In addition, in order to reach a reasonable high intensity within the gate, the time delay between the two pulses should not be larger than the pulse duration.

In experiments, we can create such ellipticity dependent pulses by using a quartz plate and a quarter wave plate the figure below.

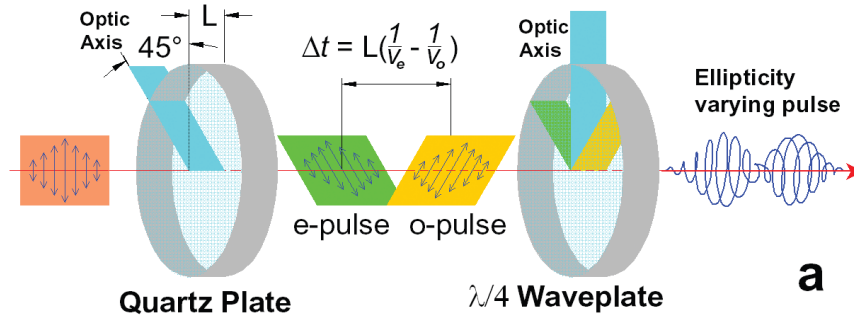


Figure 1-7 Optical components for polarization gating. Adapted from [23].

In practice, polarization gating was used to generate single attosecond pulses with a driving pulse duration of 5 fs or shorter and it was first demonstrated in 2006 [23]. However, it is challenging to generate such short driving pulse on a daily basis, and in the next session, we will introduce the Double Optical Gating (DOG) method in which laser pulses with longer pulse duration can be used to generate single attosecond pulses.

1.4.2 Double Optical Gating

From the previous discussions, we can find that polarization gating requires very short driving pulses. The double optical gating (DOG) technique has been proposed and experimentally investigated [24] to reduce the requirement for the input pulse. The double optical gating combines the two color gating [25] and polarization gating, and is a highly robust method for generating isolated single attosecond pulses on a daily basis.

In double optical gating, a weak second harmonic field is added to the driving laser field, and the symmetry of the driving laser field is broken. Using this driving laser field, the HHG

radiation process occurs every full laser cycle instead of every half laser cycle. This is illustrated in Figure 1-8. The color gradient in the figure shows the ellipticity of the driving pulse, the white color indicates that the drive pulse is linearly polarized and the blue color indicates circular polarization. The gating width is presented with two vertical lines. From this figure we can see that, when the gate width is one optical cycle, at least two attosecond pulses will be generated in polarization gating, while in double optical gating, only one attosecond pulse will be generated.

The polarization gate temporal width is given by [10]

$$\delta t_G = \frac{1}{\ln 2} \epsilon_{th} \frac{\tau^2}{T_D} \quad (1-11)$$

where ϵ_{th} is the threshold ellipticity which is defined as the ellipticity at which the high harmonic yield drop to 20% of its value when the driving pulse is linearly polarized, τ is the pulse duration of the driving pulse and T_D is the time delay between the two counter rotating pulses. We can see from Figure 1-8 that in double optical gating, attosecond pulses are generated every full cycle of the driving laser pulse instead of half laser cycle, so we can increase the gate width to one full optical cycle. By increasing the gate width, isolated single attosecond pulses can be generated from 10 fs driving pulses which is longer than polarization gating (5 fs). Generation and maintenance of 10 fs pulses are much easier.

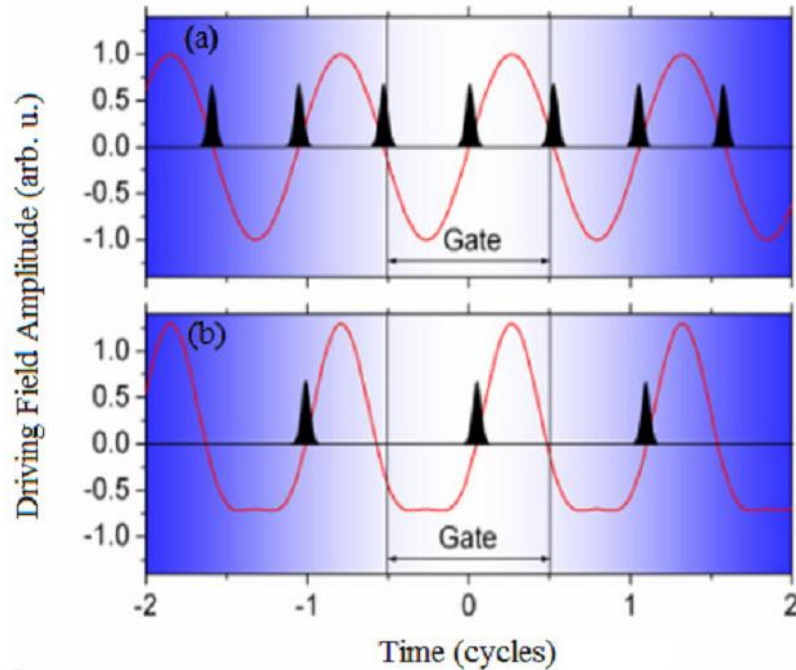


Figure 1-8 Attosecond pulse generation in polarization gating (a) and double optical gating (b). Adapted from [26]

The DOG scheme has another advantage, the ground state population on the leading edge can be reduced [24], thus the conversion efficiency can be increased as compared to polarization gating.

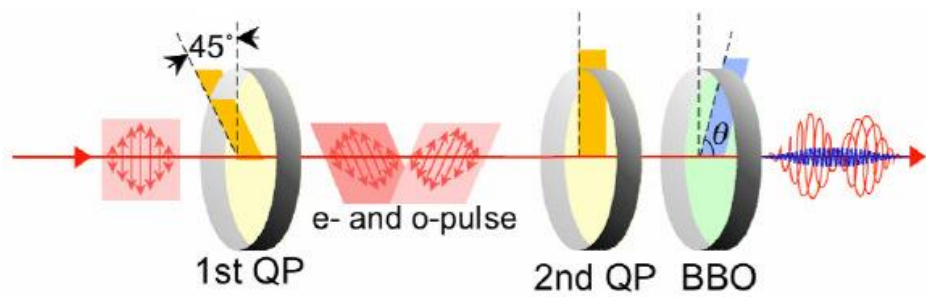


Figure 1-9 Optic components for double optical gating. Adapted from [24]

The driving pulse duration can be extended to even longer by using the generalized double optical gating technique [27]. In the generalized double optical gating, the ellipticity of

the counter-rotating pulses is less than one, the pulse has an elliptically polarized leading and trailing edge. This is accomplished by reflecting a portion of the driving field away by placing a Brewster window after the first quartz plate in the double optical gating optics, the gating field still remains the same. The setup is shown in Figure 1-10.

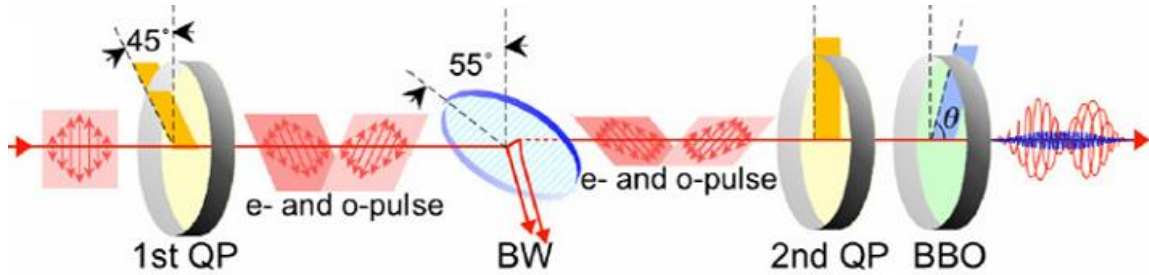


Figure 1-10 Optics for creating the field for generalized double optical gating. Adapted from [27]

The generalized double optical gating technique was demonstrated to be able to generate single attosecond pulse using 28 fs driving pulses [27]. In our attosecond transient absorption experiments, we will use the generalized double optical gating technique to generate single attosecond pulses.

CHAPTER 2 - ATTOSECOND TRANSIENT ABSORPTION SPECTROSCOPY

Over the decades, the development of ultrafast laser technology created new time scale for experimental observations. Molecular vibrations occur on a time scale of tens to hundreds of femtoseconds, and this is the characteristic time scale for the motion of atoms in molecules. The nuclear motion in molecules has been studied extensively by using the femtosecond pump-probe spectroscopy technique. The motion of electrons in matter occurs on the attosecond time scale ($1 \text{ as} = 10^{-18} \text{ s}$). For example, the time it takes one electron in the first Bohr orbit to travel a Bohr radius is 24.2 as. Using femtosecond pump-probe spectroscopy technique is insufficient to track the dynamic evolution of electrons in matter. To study the fast electron dynamics in atoms and molecules, a light pulse shorter than the dynamics process itself is needed, and for this reason, an attosecond light source is required to study electron dynamics. In recent years, advances of attosecond science has opened a new way for understanding and controlling ultrafast electron dynamics in atoms and molecules.

The attosecond transient absorption spectroscopy is a powerful tool [5] to utilize attosecond pulses for direct measurement of electron dynamics in quantum systems. In this chapter and the next few chapters, I will discuss the generation of attosecond pulses, the fundamental principles and experimental setup of the attosecond transient absorption spectroscopy technique, and some experiments utilizing the technique to study the electron dynamics in helium, neon atoms, and in hydrogen molecules.

2.1 The Attosecond Transient Absorption Experimental Setup

The attosecond transient absorption experimental setup is shown in Figure 2-1. Few-cycle NIR laser pulses are generated from a hollow core fiber compressor with chirped mirrors (UFI PC70). The beam is split and sent into two arms using a broadband beam splitter (LayerTec #108215). The broadband beam splitter reflects 50% and 80% of the laser pulses for s-polarization and p-polarization respectively. In one arm, the laser pulses generate single attosecond pulses using the generalized double optical gating (GDOG) from a rare gas (xenon/argon) filled cell with 1.0 mm inner diameter. The focal length of the focusing mirror is 500 mm (Newport 10DC1000ER.2). The entrance window is a 0.7 mm fused silica plate with AR coating (CVI W2-PW1-1005-UV-670-1064-0). An aluminum/indium filter (Lebow Company) is used to block the residue NIR pulses, select the proper XUV energy range and compensate the intrinsic chirp of the attosecond pulses. A toroidal mirror with 5 degree AOI is used to focus the XUV pulse. In the other arm, the beam passes through an optical delay line [28] and then recombines with the attosecond pulses. Both pulses are focused into the target gas cell filled with the gas to be studied.

The time delay between the XUV pulse and the NIR pulse is controlled by using a piezoelectric transducer stage. The optical path difference suffers from environmental noise such as air fluctuations as well as vibrations of optical tables and mechanical parts. Such instability can be suppressed by using a Mach-Zehnder optical interferometer in which a continuous wave laser field propagates in both arms. By stabilizing the interference pattern, the optical path length difference between the two arms can be locked to within 20 as RMS for the experiments. The details of this design can be found in [28]. This interferometer configuration is able to keep the stability when the delay between the two arms is changed.

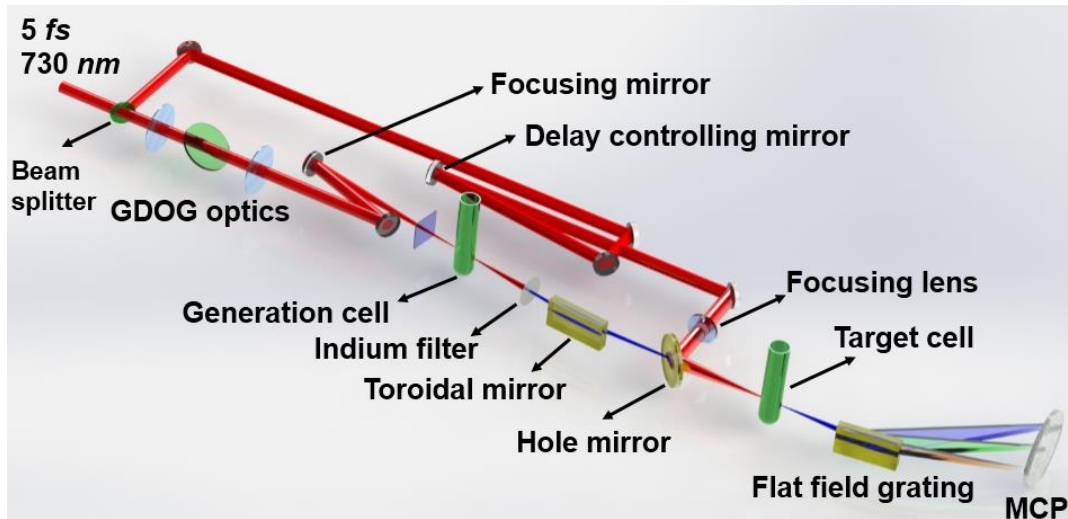


Figure 2-1 Schematic of the attosecond transient absorption setup. Adapted from [29]

High-order harmonics generation (HHG) from the interaction between ultrashort femtosecond laser pulses and gas jets is a novel source of extremely ultraviolet (XUV) radiation [6, 8, 30]. With proper gating methods [24, 27, 31, 32], HHG is also the main source of isolated attosecond pulses (IAP), which holds the promise to observe and control electron dynamics inside atoms and molecules in attosecond timescale. Recent advance in ultrafast dynamics observation with HHG and IAP [5, 33-35] have greatly relied on spectral resolved XUV measurement. From this point of view, XUV spectrometer is significantly important to attosecond technology, especially for attosecond transient absorption experiment [5, 35, 36], in which the transmitted spectrum of the XUV pulses is measured as a function of time delay between the XUV and near-infrared (NIR) laser pulses. Abundant ultrafast dynamics information is encoded in the transmitted XUV spectrum. The accuracy and resolution of the XUV spectrometer therefore plays a critical role in attosecond transient absorption experiment.

One of the advantages of the attosecond transient absorption spectroscopy technique is that the achievable spectrometer resolution is high [37]. Insufficient spectrometer resolution will broaden or even smear out the absorption peak features. In our case, the transmitted XUV spectra is recorded on a XUV spectrometer which has a resolution of ~ 50 meV near 28 eV [29].

The spectrometer consists of a flat field grazing incidence grating and a flat detector, the detector can be either a micro-channel plate (MCP) with a phosphor screen or an XUV charge-coupled device (CCD) camera. In order to focus various wavelength into a flat detector, the XUV grating has a spherical surface with variable line spaced grooves. The complex structure of the grating makes the focal length of each spectrum component very sensitive to the incident angle and objective distance which is the distance between XUV source and the center of grating.

The XUV grating used in the transient absorption setup is the Hitachi 001-0640 XUV grating with a flat field in the spectrum range of 11 – 62 nm. To quantitatively evaluate the sensitivity, we calculated the focal length of a Hitachi XUV grating for different incident angles and objective distance. The wavelength of the incident beam is assumed to be 40 nm. The result shows that 2 cm off in the objective distance will change the focal length by 5 mm and 0.5 degree error of the incident angle will result in 10 mm error of the focal length. Both of these small errors will dramatically enlarge the spatial width of spectral lines on MCP, which will worsen the resolution of the spectrometer. Therefore precisely assembling and carefully aligning is required to develop a XUV spectrometer with good performance, however, that doesn't guarantee all the parameters are perfectly set to be the designed value. Accurate calibration is indispensable to appraise and optimize the XUV spectrometer.

Usually, the XUV spectrometers are calibrated using the absorption edges of metal foils [37, 38], laser produced plasma [39, 40], or Electron Beam Ion Trap (EBIT) [41, 42]. Metal foils can only provide very few spectrum lines to benchmark the XUV spectrometer. The spectrum of XUV generated from plasma is either complicated or doesn't have sufficient intensity in the energy range of interest. And EBIT is not available for most of laboratories. In our attosecond transient absorption setup, the calibration is performed by measuring argon $3s3p^6np$ auto-ionization lines, as well as helium $1snp$ absorption lines. All of those lines are in the energy range of 20-30 eV. Besides, the line widths of the $3s3p^64p$, $3s3p^65p$ and $3s3p^66p$ states of argon are 80 meV, 28.2 meV and 12.6meV, respectively, which can be used to examine the resolution of the XUV spectrometer.

To perform attosecond transient experiment with Ar/He gas, we built a XUV spectrometer with spectrum range of 20 – 30 eV (40 – 62 nm). A Hitach 001-0640 XUV grating with a flat field in the spectrum range of 20-112 eV (11-62 nm) is installed in a vacuum chamber. The designed incident angle, objective distance and imaging distance is 85.3° , 350 mm and 469 mm, respectively. With the help of a proper adaptor, the grating is hold by a mirror mount, whose actuators are connected to rotary feedthroughs on the side flange of the vacuum chamber. This design allows further fine tuning of the grating even if the spectrometer is under vacuum. The dispersed XUV spectrum reaches the MCP after passing through an extension tube and a bellow, which makes the image distance – the distance between the center of the grating and MCP – adjustable in the range of 440 - 470 mm. The reason to have the incident angle and image distance adjustable is that: i) the dispersed spectrum is so sensitive to these parameters that small errors will lead to significant reduction of the resolution, as we addressed above; ii) the focus position of 40–62nm spectrum components are at the edge of the flat focal plane of the

grating, and they are not in a line parallel to flat focal plane in which the MCP is placed. So adjustment of incident angle and imaging distance is requisite otherwise the resolution for 40–62nm spectrum components is expected to be very low if we keep the designed incident angle and imaging distance.

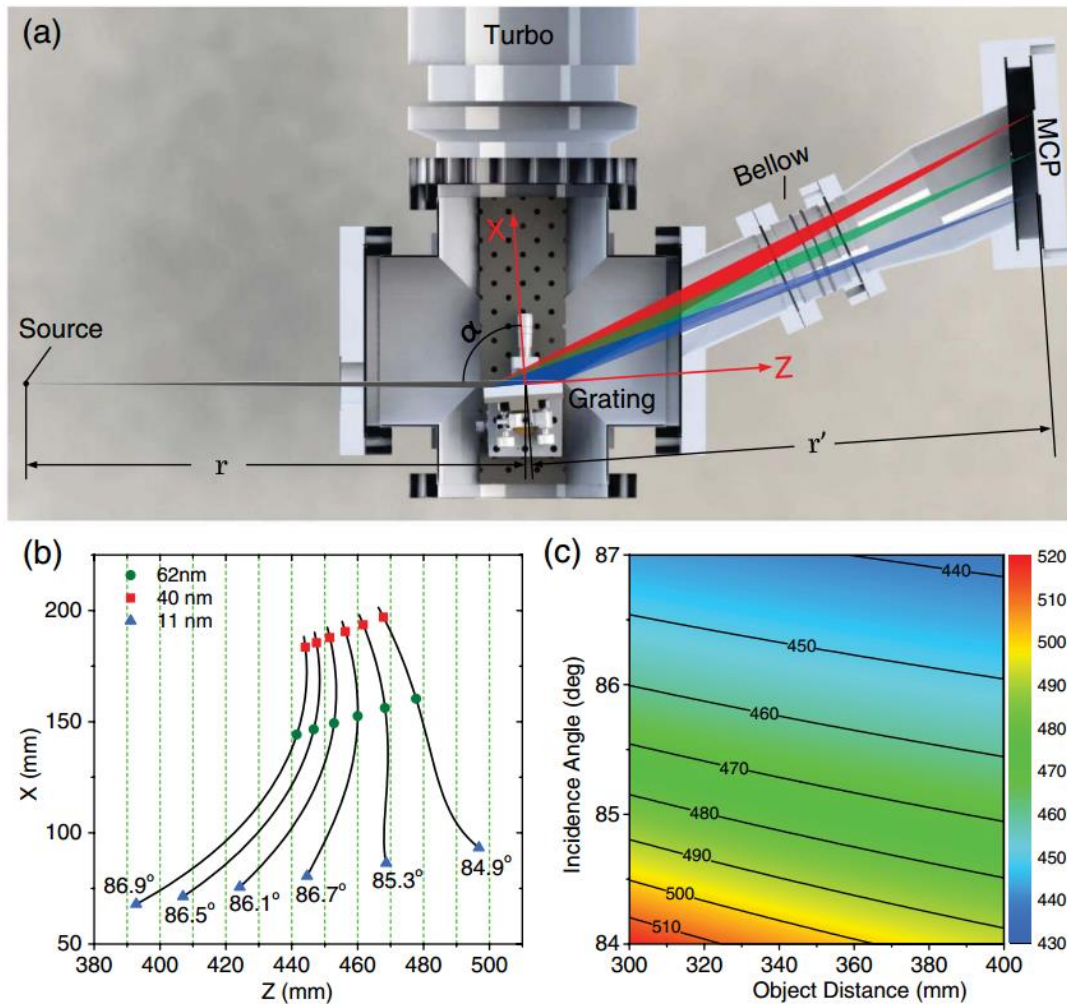


Figure 2-2 (a) Top view of the XUV spectrometer. (b) Focal “plane” of the XUV grating for different incidence angles. Each plane covers a spectrum range from 11 nm (triangles) to 62 nm (squares), and the 40 nm components (circles) are also marked in each focal plane. For 86.5° incidence angle, the spectrum from 40 to 60 nm is approximately in a vertical plane (MCP plane). The axes are defined in (a). (c) Dependence of grating image distance of 40 nm XUV light on object distance and incidence angle. Adapted from [29]

Simulation shows that changing the incident angle will indeed help to make the measured spectrum to be focused on a flat plane parallel to MCP. We plot the focus position for the spectrum component from 11 nm to 62 nm with different incident angle. The results indicate that the incident angle and imaging distance should be set to 86.5° and 448 mm respectively. To verify the resolution under this geometric configuration, ray tracing is carried out with Zemax [43]. The light source in the ray tracing consists of 6 difference wavelength component corresponding to three helium absorption lines (1s2p, 1s3p, 1s4p) and three argon autoionization lines (3s3p⁶4p, 3s3p⁶5p, 3s3p⁶6p). The spacial profile of the focused spectrum on the MCP is shown in the figure below. The horizontal axis is along the MCP surface, and the corresponding photon energy increases as the position axis increases, so the left three peaks are the helium absorption lines and the right three are the argon autoionization lines.

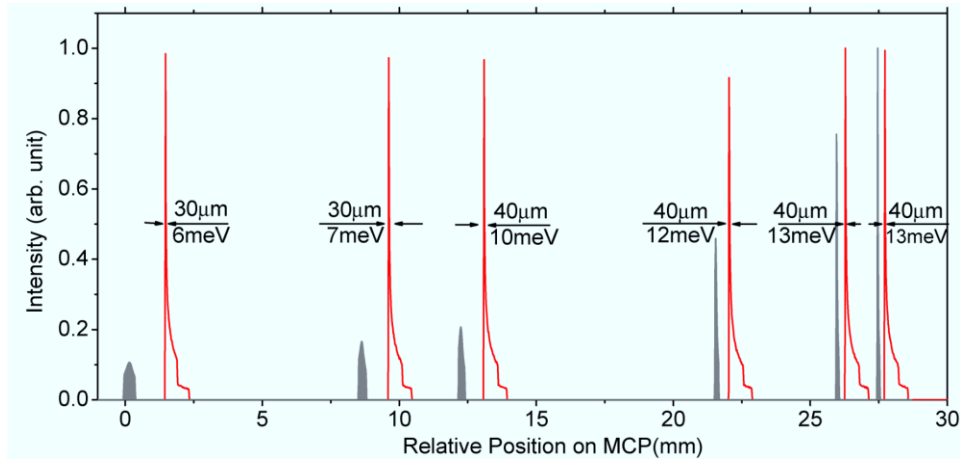


Figure 2-3 Spacial profile of the focused spectrum on the MCP if the incident angle is set to be 86.5° . The six peaks (from left to right) are helium 1s2p, 1s3p, 1s4p absorption lines and argon 3s3p⁶4p, 3s3p⁶5p and 3s3p⁶6p autoionization lines respectively. Both spacial and spectral FWHM is labeled for each peak. Adapted from [29]

The spacial full width at half maximum (FWHM) of each spectrum peak is between 30 μm and 40 μm , as labeled in the figure, which indicates that all the spectrum components are

well focused on the MCP plane since the size of each micro-channel of the MCP is just 32 nm. By taking into account the reciprocal linear dispersion of the grating, we can also estimate the spectral FWHM, which is equivalent to spectrometer resolution, since each line is monochromatic in the source. The spectrometer resolution is around 10meV, as labeled in the figure above, and it is slightly better for long wavelength components.

In the Experiment, transmitted XUV spectrum after both argon and helium was measured. The ionization potential of argon is 15.7 eV (79 nm), which is much lower than the measured energy of the spectrometer. Thus, all the measured spectrum will be strongly absorbed due to photon-ionization and the photon-ionization cross-section of argon is almost constant during the entire energy range [44] of our XUV spectrometer. So it is not expected to see any absorption structure there. However, lying in the energy range of the spectrometer there are several argon auto-ionization states [5, 45], and the interference between the direct ionization and the decay from auto-ionization states will result in Fano resonance profiles [46], which can be observed as transmission peaks in the absorption spectrum with resolution compatible line width. The ionization potential of helium (24.6 eV) is right in the spectrometer energy range, so a step-shape absorption spectrum is expected. Besides, the 1snp excitation states of helium will also leave their absorption mark on the measured spectrum. But without external disturbance, the 1snp excitation states are rather stable, and their lifetime can be as short as few nanoseconds [47] corresponding to few nano-eV linewidth in spectrum, which is immeasurable by the spectrometer. To see these absorption lines, moderately intense (10^{11} - 10^{13} W/cm²) NIR laser pulses need to be focused in the second cell to dress the helium atoms [35].

The transmission of XUV pulses after passing through argon or helium cell are presented in the figure below. The backing pressure of the second cell is 35 torr and 50 torr for argon and

helium respectively. In the argon transmission curve (red solid), five peaks corresponding to the five autoionization states listed in the table below are identified by the gray arrows. In helium absorption experiment, the intensity of dressing laser is set to be about 5×10^{12} W/cm² to broaden the 1snp lines. The step around 900th pixel in the helium transmission curve (blue line with filled area) is the ionization potential of helium. Below the ionization potential, only those photons with energy equal to 1snp excited states could be absorbed due to transition from ground state to the corresponding excited states. So the dips below 900th pixel which are marked by the black arrow indicate the position of helium 1snp states. All the spectrum lines we observed with the XUV spectrometer are listed in the table below.

Table 2-1 Spectrum lines used to calibration the spectrometer. Adapted from [29]

| States | | Energy (eV) | Measured Linewidth (meV) |
|--------|----------------------|-------------|--------------------------|
| He | 1s2p | 21.242 | 235.9 |
| | 1s3p | 23.113 | 144.3 |
| | 1s4p | 23.769 | 86.4 |
| | 1s5p | 24.073 | 69.7 |
| | 1s6p | 24.239 | 69.5 |
| | 1s7p | 24.338 | - |
| | 1s8p | 24.403 | - |
| Ar | 3s3p ⁶ 4p | 26.646 | 82.46 |
| | 3s3p ⁶ 5p | 28.023 | 81.02 |
| | 3s3p ⁶ 6p | 28.543 | 82.3 |
| | 3s3p ⁶ 7p | 28.793 | 81.7 |
| | 3s3p ⁶ 8p | 28.933 | - |

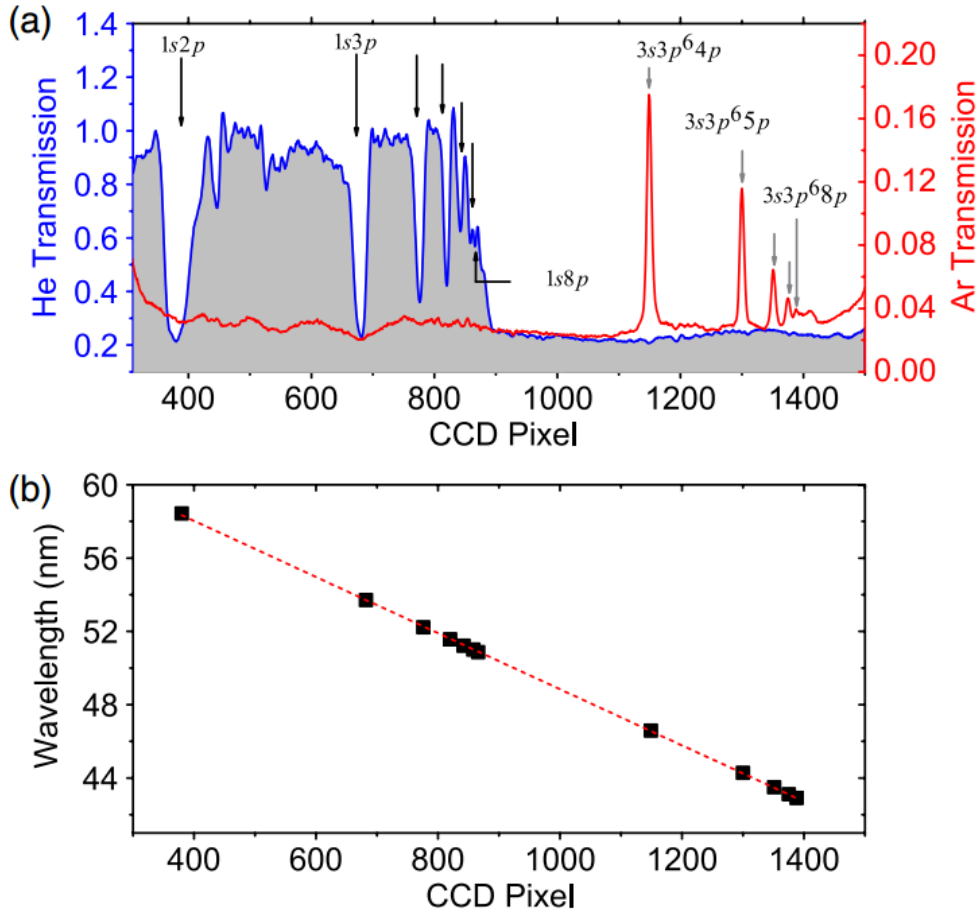


Figure 2-4 (a) Transmission of XUV pulses through a 35 torr argon cell (red solid curve) or a 50 torr helium cell (blue curve with filled area). Five argon autoionization peaks and seven helium absorption dips are identified in the figure. (b) Wavelengths of the 12 spectral lines (squares) identified in (a), and the linear fitting (red dashed line). Adapted from [29]

Now we have 12 known spectrum lines to calibrate the spectrometer. The wavelength of spectrum lines is plotted in Figure 2-4 (b) as a function of their pixel location on the CCD. In the narrow wavelength range of interest it is a reasonable assumption that the wavelength is proportional to pixel location. So the relationship between the wavelength and pixel location can be fit as:

$$\lambda = kx + \lambda_0 \quad (2-1)$$

By performing linear least square fitting for the 12 known spectrum dots, , we can get $k = -0.01531$, $\lambda_0 = 64.154$. The effective pixels of HHG spectrum on the CCD are in the range of 310-1500, so the wavelength range of the spectrometer is 41.19-59.41nm (20.87-30.10eV). After the calibration of the spectrometer, we can easily measure the FWHM of each spectrum lines by fitting the spectrum line with a Gaussian curve. The FWHM of each spectrum are listed in Table I (some peaks are too weak to be correctly fit). The actual linewidth of the first three argon autoionization states [5] are also listed in Table 2-1. By comparing them with the measured linewidth, we can see that the resolution of the spectrometer is 60 meV. But in the low energy range, the resolution is slightly better (~50 meV), which agrees with our previous estimation. Note that the linewidth of argon $3s3p^66p$ autoionization state is just 12.6 meV, which enable this method to examine the XUV spectrometers with energy resolution as high as 13 meV.

Although ray tracing result suggests a resolution as high as 10 meV, the resolution of our XUV spectrometer is calibrated to be 60 meV. The difference is caused by couple of issues. First, the XUV focal point in the absorption cell serves as the entrance slit to the spectrometer, so the spectrometer resolution is partially determined by the focal spot size of the soft x-ray beam at the sample position. While in the ray tracing, an ideally point source is used. Second, since the spectral data is finally read out through a CCD on which the MCP phosphor is imaged with a lens, both the CCD noise and imaging process will introduce some error to the spectrum data. Finally, a monochromatic point source will be imaged as a sharp peak with a broad outsole by the grating. The FWHM somehow is no longer a valid physical quantity to evaluate the width of the spectrum.

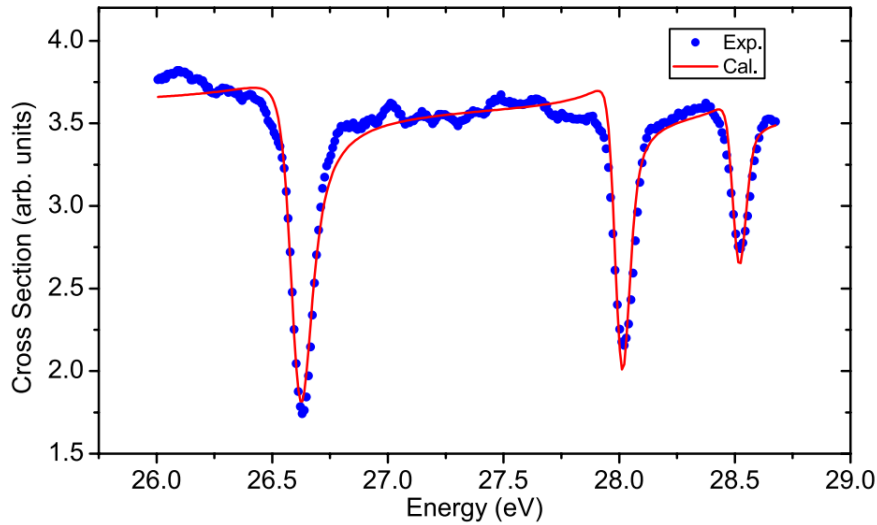


Figure 2-5 Comparison between measured absorption cross section (dots) and argon autoionization Fano profile convoluted by a Gaussian function with FWHM of 60 meV (solid curve). Adapted from [29]

In order to determine the resolution of our imaging system, we measured the image of the so-called “quantum noise”. When we apply a very high voltage (1800 V) to the front surface of the MCP, a stray electron will be amplified and form an electron avalanche, and the image observed on the phosphor screen is from a single microchannel pore. The image is shown in the figure below. The FWHM of the image is $131 (\pm 27) \mu\text{m}$ and $151 (\pm 33) \mu\text{m}$ along x and y axes respectively. Our spectrometer resolution was calibrated to be 60 meV which corresponds to a $190 (\pm 13) \mu\text{m}$ FWHM. We can see that the spectrometer resolution is mainly limited by the MCP imaging resolution.

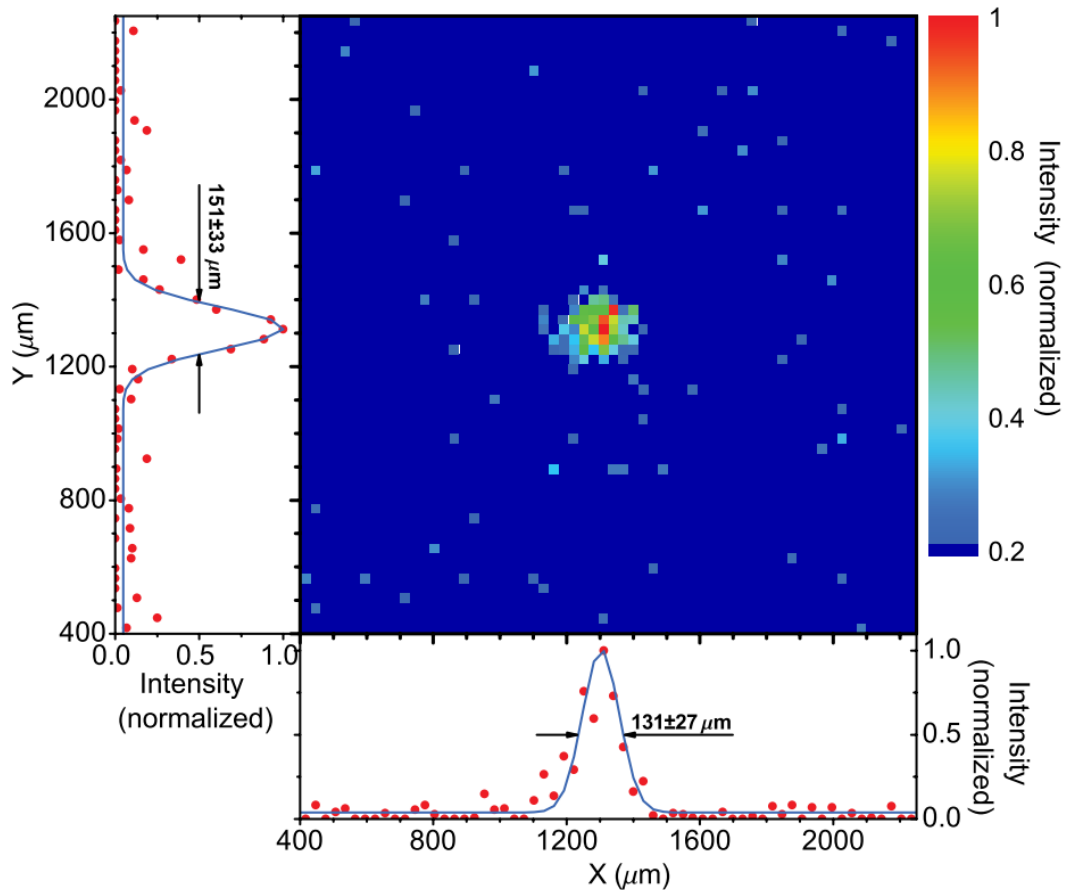


Figure 2-6 Image of the electron distribution of a single microchannel pore, with corresponding lineouts (symbols) along the x (dispersion) and y (position) axes. Gaussian fits (solid curve) to the measured distribution give FWHM resolution of 131 μm and 151 μm along the x and y axes, respectively. The error comes from the Gaussian fit. Adapted from [29]

We developed XUV spectrometer with energy range of 20-30 eV for attosecond transient absorption experiment and proposed a novel method to calibrate it. By measuring helium absorption lines and argon autoionization lines, the XUV spectrometer can be easily calibrated and the resolution can also be determined simultaneously. Since there are up to 12 known spectrum features which are located in the spectrometer energy range uniformly, the calibration is rather accurate. The resolution of our homemade XUV spectrometer is determined to be 60

meV, however, this method has the potential to evaluate the XUV spectrometer with a resolution as high as 13 meV.

The attosecond transient absorption spectroscopy technique also allows direct and simultaneous measurement of the excited state dynamics and quantum interference both above and below the ionization threshold, which is not possible by using the attosecond photoelectron spectroscopy [48].

2.2 Theory of Attosecond Transient Absorption Spectroscopy

The attosecond transient absorption spectroscopy setup is all-optical, which makes it much simpler than the attosecond streaking camera spectroscopy. However, interpreting the time-delay dependent absorption spectrum of target atoms and molecules is still challenging. In attosecond transient absorption spectroscopy experiments, the number of photons is relatively large (on the order of 10^{15} photons per pulse for NIR laser pulses and on the order of 10^7 photons per pulse for attosecond pulses), we can treat the laser-target interaction semi-classically in which the targets (atoms or molecules) are described quantum mechanically while the laser pulses are treated by classical electrodynamics.

The spectrum of laser pulses that go through a gas cell can be calculated using the Beer-Lambert Law when non-linear effects and temporal shaping of the input pulses can be neglected.

The transmitted spectrum:

$$I_{out}(\omega) = I_{in}(\omega) \exp \left\{ - \frac{4\pi\omega}{c} \mathbf{Im} \left[\frac{\tilde{P}(\omega)}{\tilde{\epsilon}_{in}(\omega)} \right] NL \right\} \quad (2-2)$$

where $I_{in}(\omega) = |\tilde{\epsilon}_{in}(\omega)|^2$ is the incident laser pulse intensity, $I_{out}(\omega) = |\tilde{\epsilon}_{out}(\omega)|^2$ is the transmitted laser pulse intensity, NL is the density-length product of the target, $\tilde{P}(\omega)$ is the polarization spectrum of the atom.

In experiments, absorbance $A(\omega)$, which is defined as the common logarithm of the ratio of incident to transmitted radiant power through a material [49], is given by

$$A(\omega) = \frac{4\pi\omega}{c} \mathbf{Im} \left[\frac{\tilde{P}(\omega)}{\tilde{\epsilon}_{in}(\omega)} \right] NL \quad (2-3)$$

The polarization spectrum is given by the Fourier transform of the time dependent dipole moment

$$P(t) = \langle \Psi(\mathbf{r}, t) | z | \Psi(\mathbf{r}, t) \rangle \quad (2-4)$$

$$P(\omega) = \int_{-\infty}^{\infty} d\omega P(t) e^{i\omega t} \quad (2-5)$$

So in order to calculate the absorption spectrum, we need to calculate the time dependent wavefunction with the combined XUV and NIR laser fields.

The laser field can be presented using the electric field \mathbf{F} and the vector potential \mathbf{A} .

$$\mathbf{F}(\mathbf{r}, t) = \mathbf{z} F_0 \cos(-\mathbf{k} \cdot \mathbf{r} + \omega_0 t + \varphi_0) \quad (2-6)$$

$$\mathbf{A}(\mathbf{r}, t) = - \int_{-\infty}^t dt' \mathbf{F}(t') = \mathbf{z} \frac{F_0}{\omega_0} \sin(-\mathbf{k} \cdot \mathbf{r} + \omega_0 t + \varphi_0) \quad (2-7)$$

where F_0 is the electric field strength, \mathbf{k} is the wave vector, ω_0 is the angular frequency, and φ_0 is the phase of the laser pulse.

By making the dipole approximation, the time dependent Schrödinger equation (TDSE) in the length gauge can be written as:

$$i \frac{\partial}{\partial t} \Psi(\mathbf{r}, t) = [H_0 - \mathbf{r} \cdot \mathbf{F}_X(t - \tau_D) - \mathbf{r} \cdot \mathbf{F}_L(t)] \Psi(\mathbf{r}, t) \quad (2-8)$$

where H_0 is the field-free Hamiltonian and $\Psi(\mathbf{r}, t)$ is the wavefunction of the target. $\mathbf{F}_X(t)$ and $\mathbf{F}_L(t)$ are the XUV and NIR laser field strength. τ_D is the time delay between the two pulses. In experiments, both the attosecond pulse and the NIR pulse are polarized along the same axis, without loss of generality, they are assumed to be polarized along z-axis. Then the interaction Hamiltonian $H'(t)$ can be written as

$$H'(t) = -zF_L(t) - zF_X(t - \tau_D) \quad (2-9)$$

which includes the interaction of the target with both the XUV laser field and the NIR laser field. The time dependent Hamiltonian is

$$H(t) = H_0 + H'(t) \quad (2-10)$$

where H_0 is the field free Hamiltonian. The wavefunction can be expanded with the set of Eigen functions of the stationary states $\Psi(\mathbf{r}, t) = \sum_j c_j(t) \psi_j(\mathbf{r})$, where $H_0 \psi_j(\mathbf{r}) = E_j \psi_j(\mathbf{r})$, $c_j(t)$ is the amplitude for the $\psi_j(\mathbf{r})$ state and E_j is the corresponding eigenenergy, and the time dependent Schrodinger equation can be rewritten:

$$i \frac{\partial}{\partial t} \sum_j c_j(t) \psi_j(\mathbf{r}) = \sum_j [E_j - zF_L(t) - zF_X(t - \tau_D)] c_j(t) \psi_j(\mathbf{r}) \quad (2-11)$$

Using the orthogonality of the stationary states $\langle \psi_a | \psi_j \rangle = \delta_{aj}$ and the dipole matrix element is defined as $d_{aj} = \langle \psi_a | z | \psi_j \rangle$, by projecting the Schrodinger equation onto the state $\psi_a(\mathbf{r})$, we can get a set of coupled differential equations:

$$i \dot{c}_a = E_a c_a(t) - \sum_{j \neq a} d_{aj} [F_L(t) + F_X(t - \tau_D)] c_j(t) \quad (2-12)$$

By using theoretical eigenstate energy values and dipole matrix elements, the equations can be solved numerically. Then we can calculate the polarization spectrum using equation (2-4) and (2-5), the absorbance is then given by:

$$A(\omega) = \ln \left(\frac{|\tilde{\epsilon}_{out}(\omega)|^2}{|\tilde{\epsilon}_{in}(\omega)|^2} \right) = \frac{4\pi\omega}{c} \mathbf{Im} \left[\frac{\tilde{P}(\omega)}{\tilde{\epsilon}_{in}(\omega)} \right] NL \quad (2-13)$$

In our case, programs written in LabVIEW and C++ are used to perform the calculation with typical desktop computers, we will discuss the calculation results in following chapters.

CHAPTER 3 - SUB-CYCLE ELECTRON DYNAMICS IN HELIUM AND NEON ATOMS

Note: Portions of this chapter were used or adapted with permission from the following:

(1) Michael Chini, Xiaowei Wang, Yan Cheng, Yi Wu, Di Zhao, Dmitry A. Telnov, Shih-I Chu & Zenghu Chang. Sub-cycle Oscillations in Virtual States Brought to Light. Scientific Reports 3, Article number: 1105 (2013)

(2) Xiaowei Wang, Michael Chini, Yan Cheng, Yi Wu, Xiao-Min Tong, and Zenghu Chang. Subcycle laser control and quantum interferences in attosecond photoabsorption of neon. Phys. Rev. A 87, 063413 (2013)

The attosecond transient absorption spectroscopy is a powerful tool to study electron dynamics and time resolved molecular dynamics. Visualizing the electron dynamics in chemical reactions is a scientific dream. With the advent of attosecond laser pulses, it is becoming possible. Attosecond pulses have been used to study atoms, molecules and solid state systems and hold the promise of allowing new forms of photochemistry. In this chapter, I will discuss the measurement of bound state electron dynamics in helium and neon atoms using the attosecond transient absorption spectroscopy.

3.1 Sub-cycle Electron Dynamics in Helium

Development and control of materials exhibiting novel optical phenomena such as negative refractive index [50], electromagnetic-induced transparency (EIT) [51] and tunable optical resonances [52] has led to significant advances in optical technology. One of the most fundamental goals of attosecond second science is to understand and to control the dynamic evolutions of electrons in matter. While the most exotic behaviors have been observed in

complex materials, these phenomena are rooted in well-known optical physics concepts and can also be studied at the fundamental level in atomic systems, using moderately intense ($<10^{13}$ W/cm²) lasers to control the electronic structure and therefore the optical properties.

Among the most fundamental optical properties of an atom is its absorption spectrum. Spectrally-resolved absorption has long been used to study atomic structure [53] and provides a “fingerprint” for identifying atomic and molecular species. With the addition of a moderately intense laser field, the absorption spectrum can be modified, allowing measurement of and demonstrating control over the electron dynamics in the atom on ultrafast timescales. Laser-dressed absorption measurements have recently demonstrated controllable EIT-like phenomena in atoms at extreme ultraviolet (XUV) [54] and x-ray [55] wavelengths. More recently, transient changes in the absorption of an isolated attosecond pulse in the presence of a synchronized few-cycle laser pulse were observed in valence electron wavepackets in field-ionized krypton [34], autoionizing states of argon [5] and Stark-shifted excited states of helium [35] allowing measurement of electron dynamics on the few-femtosecond and even sub-laser-cycle timescale. Here, we study the absorption of an isolated attosecond pulse in the vicinity of the helium absorption line manifold corresponding to excitation of an electron from the ground state ($1s^2$) to the $1snp$ excited states. When the attosecond pulse overlaps in time with a moderately intense ($\sim 10^{11}$ - 10^{13} W/cm²) few-cycle laser field, new absorption features appear below the ionization threshold that correspond to two-color multi-photon absorption to bound states inaccessible to the attosecond pulse alone. By changing the delay between the attosecond pulse and the laser field, the absorption strength of these features can be modulated on timescales as short as a quarter-cycle of the dressing laser field. We further observe strong half-cycle shifts of the ionization potential, corresponding to a sub-cycle ponderomotive energy shift.

The experiment was performed using the attosecond transient absorption technique [5], in which the absorption of an isolated attosecond pulse is measured in the presence of a delayed laser field as a function of the time delay. The experimental setup combines the high temporal resolution afforded by the isolated attosecond probe pulse in an actively stabilized interferometer [28] with the high spectral resolution of XUV absorption spectroscopy [37]. Compared to attosecond photoelectron spectroscopy [56], the attosecond transient absorption technique allows observation of bound state dynamics and quantum interferences with high fidelity in low-intensity laser fields, where the probability of ionization (and therefore the photoelectron yield) is small, as well as state selectivity in high-intensity laser fields where the contribution of multiple ionization channels complicates the interpretation of photoelectron spectra.

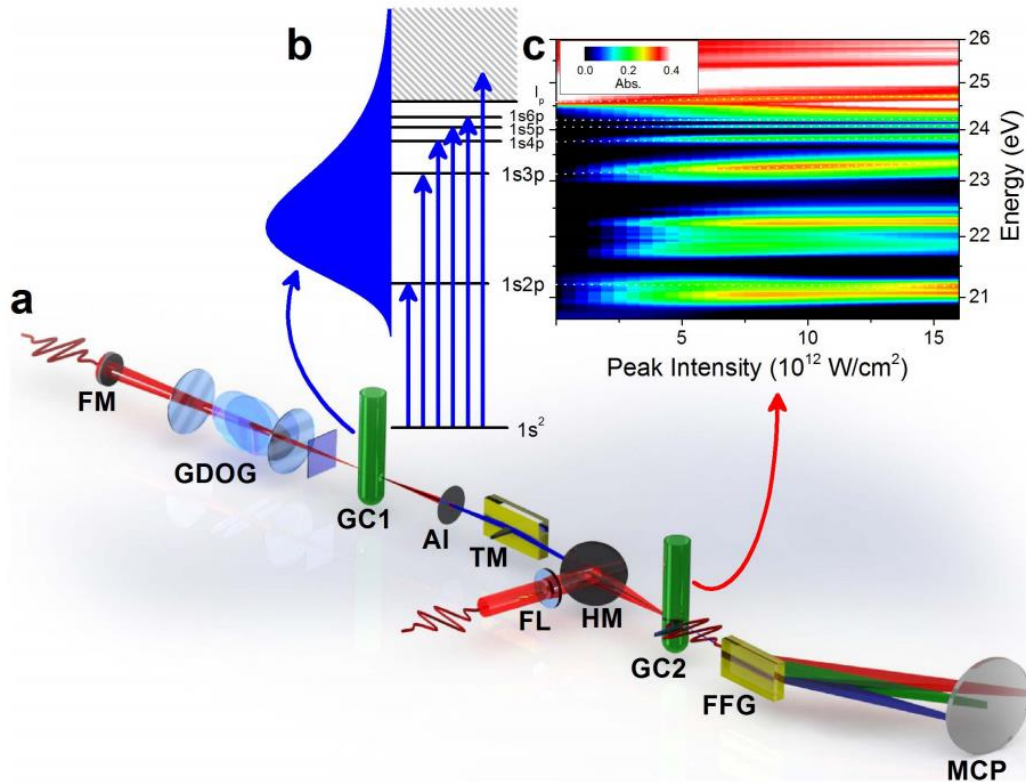


Figure 3-1 (a), Schematic of experimental setup for attosecond transient absorption. (b), Helium $1snp$ energy level diagram showing schematic XUV spectrum and states accessible for excitation by the attosecond pulse. (c), Measured absorbance spectrum as a function of the dressing laser intensity when the attosecond XUV pulse overlaps in time with the peak

of the NIR laser pulse. The dotted lines trace the Stark-shifted absorption lines. At an intensity of $\sim 2.5 \times 10^{12}$ W/cm², several new absorption features appear in the vicinity of the 1s2p state, which dynamically evolve as the laser intensity is increased. Adapted from [48].

Figure 3-1(b) shows the energy level diagram of the helium 1*sn*p excited states, which extend from 21 eV above the ground state to the first ionization potential at 24.58 eV [57], along with the absorbance measured as a function of the dressing laser intensity at a fixed time delay where the laser field overlaps with the attosecond pulse. As the intensity of the dressing laser is increased, the absorption in the vicinity of the 1*sn*p excited state manifold changes significantly [58-60]. For the 1s3p (23.09 eV) and higher-lying states (leading to the absorption edge at the ionization potential), these changes amount to energy shifts of the absorption lines, which correspond to AC Stark [35] and ponderomotive shifts. However the laser-dressed 1s2p absorption line, which was not observed in previous experiments, exhibits more complicated structure, including energy level splitting and formation of new absorption sub-structures (near 22 eV, becoming prominent at intensities above $\sim 2 \times 10^{12}$ W/cm²) in addition to a relatively small AC Stark shift. These complex features have previously been attributed to strong couplings between the 1s2p (21.22 eV) and 1*sn*l (*l* = *s*, *d*) states [59, 60], but the individual sub-structures could not be identified.

By scanning the time delay between the attosecond XUV and few-cycle NIR pulses, we can trace the dynamics of the individual sub-structures and elucidate their origins. The figure below shows the absorbance spectrum as a function of the time delay for dressing laser intensities of 7×10^{11} W/cm² and 5×10^{12} W/cm². Negative delays indicate that the attosecond pulse arrives on the target before the NIR pulse. While the new absorption sub-structures are most prominent near zero delay where the two pulses overlap, they can still be observed for large

negative delays. Furthermore, the absorption line energies and amplitudes change dynamically near zero delay, whereas they are relatively constant for larger negative delays. These dynamic features can allow us to identify the origins of each sub-structure.

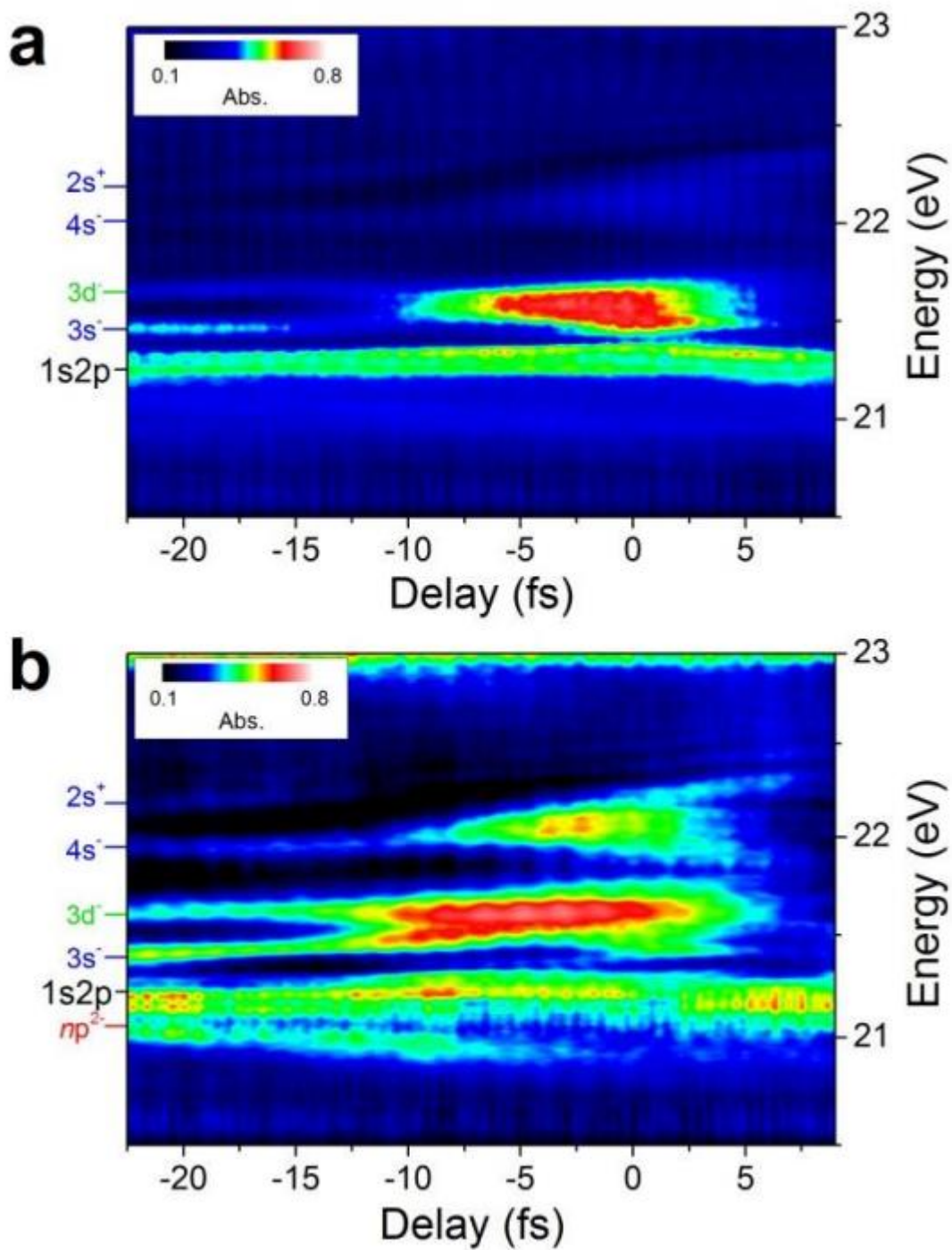


Figure 3-2 Two-color multi-photon absorption in time-resolved absorption. The absorption in the vicinity of the 1s2p state at lower dressing laser intensities of a, 7×10^{11} W/cm² and b, 5×10^{12} W/cm² allow for experimental identification of the virtual states appearing in the laser-dressed absorption. Adapted from [48].

The observed absorption sub-structures can each be assigned to an excitation pathway to a given $1snl$ excited state by the simultaneous absorption of an XUV photon and one or more NIR photons. The assignment of the excited states was confirmed by solution of the time-dependent Schrödinger equation in the two-color field.

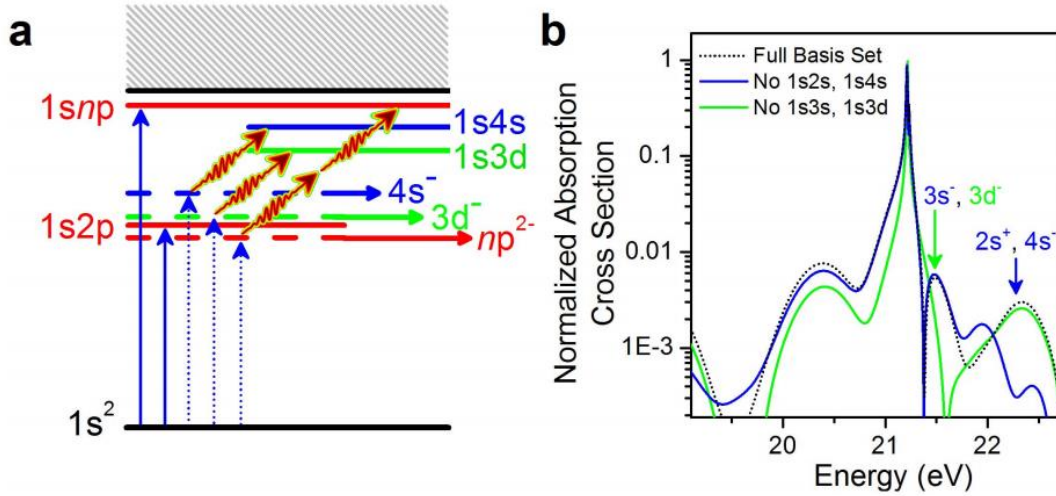


Figure 3-3 (a), Schematic diagram of two-color two- and three-photon absorption pathways to the $1s3d$ (green), $1s4s$ (blue), and $1snp$ (red) excited states. The solid arrow indicates the single-photon excitation of the $1s2p$ and $1snp$ (red) states, whereas the dotted arrows indicate XUV absorption via two-color multi-photon excitation to $1snp$ states with $n \geq 6$. Dashed lines indicate absorption lines corresponding to laser-induced virtual states. (b), Normalized photoabsorption cross-sections based on TDSE simulation of helium when the attosecond XUV pulse overlaps in time with the peak of the NIR laser field. By removing the $1s2s$ and $1s4s$ states (blue) or $1s3s$ and $1s3d$ states (green) from the calculation, we can confirm that the additional absorption lines are due to multi-photon excitation to those excited states. Adapted from [48].

Unlike the single-XUV photon absorption rate for excitation to the $1snp$ states in the absence of the laser field, which is proportional to the cycle-averaged intensity, the probability of two-color multi-photon absorption is highest when the attosecond pulse overlaps with a maximum or minimum of the instantaneous laser electric field. Therefore, we expect to see a strong half-cycle periodicity in the absorption lines corresponding to two-photon (XUV+NIR)

excitation to $1sns$ and $1snd$ states and quarter-cycle periodicity in the absorption lines corresponding to three-photon (XUV+NIR+NIR) excitation to $1snp$ states. The figure below shows the absorbance spectrum as a function of the time delay for a dressing laser intensity of 1×10^{13} W/cm². Negative delays indicate that the attosecond pulse arrives on the target *before* the NIR pulse. While the new absorption sub-structures are most prominent near zero delay where the two pulses overlap, they can still be observed for large negative delays. Additionally, absorption sub-structures above the ionization threshold (ns^+ and nd^+ , 25-28 eV) and below the $1s2p$ energy level ($2s^-$, ~19 eV) are revealed in the time-dependent measurement. As the time delay is scanned with attosecond precision, the absorption strength of each feature is modulated on timescales faster than the laser cycle period. We find that the absorption strength in the vicinity of the $2s^+$, $3s^-$, $4s^-$, and $3d^-$ absorption features is modulated with a half-cycle periodicity, whereas the absorption strength near the np^{2-} absorption feature oscillates with a quarter-cycle periodicity. Furthermore, the absorption line energies change dynamically near zero delay, revealing Autler-Townes splitting of the $1s2p$ absorption line in addition to sub-cycle AC Stark and ponderomotive energy level shifts of the $1s3p$ and higher-lying states.

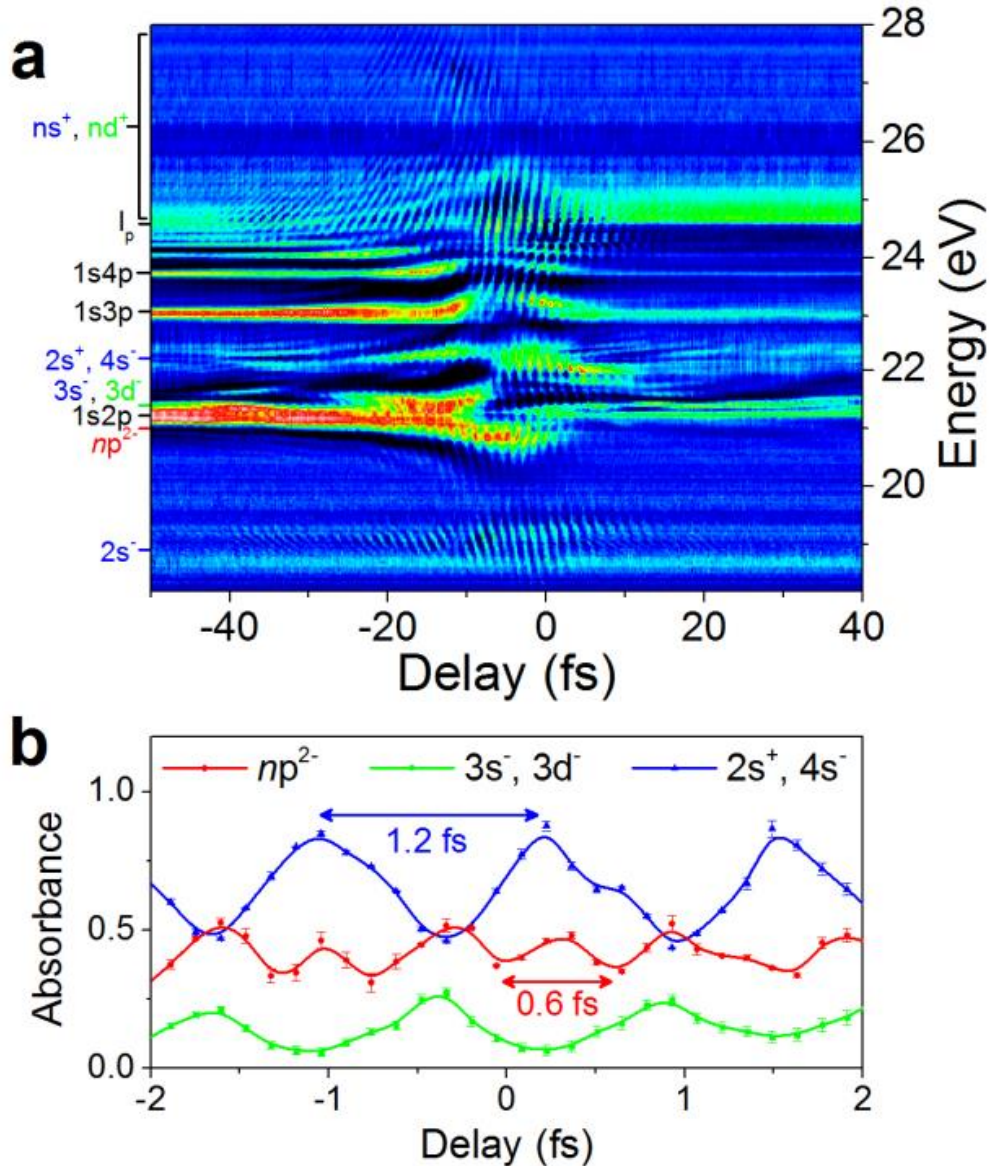


Figure 3-4 a, Time-delay-dependent absorbance spectrum with a dressing laser intensity of 10^{13} W/cm². With the strong dressing laser field, quantum-optical interferences can be observed in the absorption at negative delays. Near zero delay, the attosecond and NIR laser pulses overlap, and the absorption is dominated by the sub-cycle AC Stark and ponderomotive energy level shifts. **b**, Absorbance lineouts in the vicinity of the transient virtual states. The absorbance (data points) was obtained by integrating the signal in the vicinity (± 50 meV) of the virtual intermediate states, and the error bars indicate the standard deviation of the absorbance in that region. The solid lines serve to guide the eye. While the absorbance near the $3s^-$, $3d^-$, $2s^+$, and $4s^-$ virtual states oscillates with half-cycle periodicities, the absorbance near the np^{2-} absorption feature oscillates with a quarter-cycle periodicity. Adapted from [48].

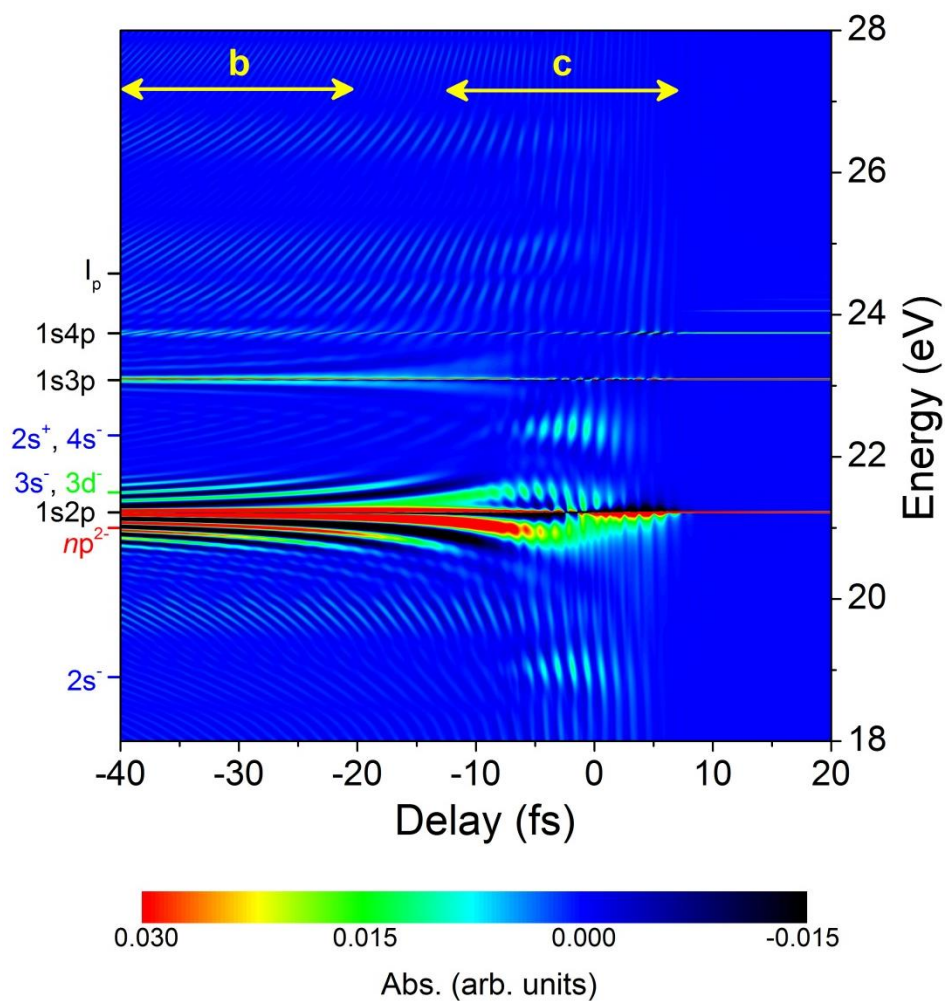


Figure 3-5 Simulated time-delay-dependent absorbance spectrum with a dressing laser intensity of 10^{13} W/cm². The spectrogram can be divided into two regions to separate the effects of quantum-optical interferences and sub-cycle energy level dynamics. Adapted from [48].

The relative strengths of the half-cycle and quarter-cycle periodicities can be evaluated by taking the Fourier transform along the delay axis for every energy and comparing the strengths of the different oscillatory components. The quarter-cycle oscillations, which are

clearly apparent for three-photon excitation to the $1snp$ ($n \geq 6$) excited states at an XUV photon energy near 21 eV, are the fastest dynamic feature observed so far pump-probe spectroscopy.

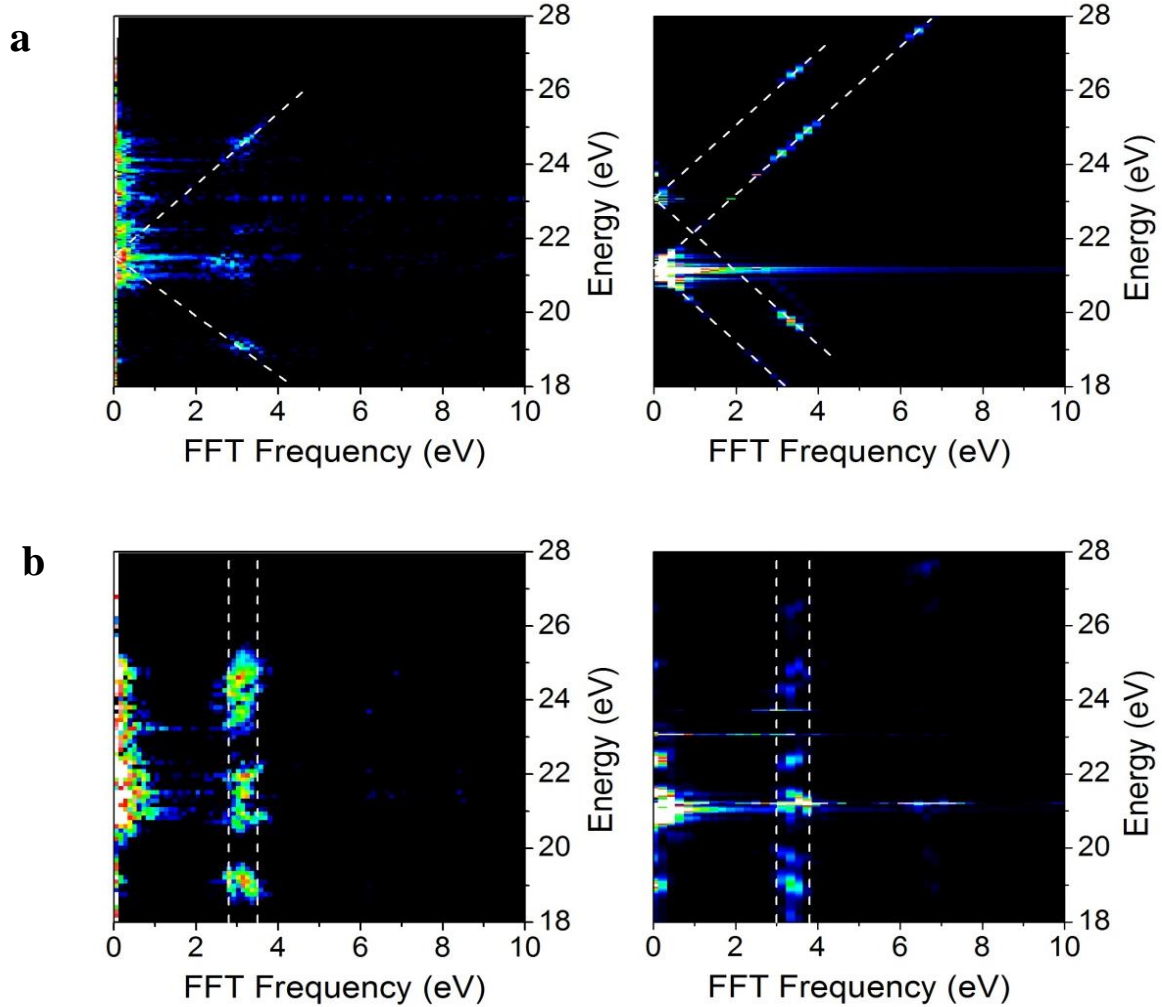


Figure 3-6 (a) Fourier transform analysis of region b in Figure 3-5, which spans $-40 fs < \tau_D < -20 fs$. The FT spectrogram obtained from the experimental data is shown in the left panel, while the right panel shows that obtained from the simulated data. The dashed 45-degree lines indicate the two-path quantum-optical interference. (b), Fourier transform analysis of region c, which spans $-13 fs < \tau_D < 7 fs$. Half- and quarter-cycle oscillations are evident above and below the ionization potential, and the oscillation frequency no longer follows the 45-degree lines associated with the two-path interference. Adapted from [48].

At higher intensities, the excited state dynamics become significantly more complicated, owing to the interactions of bound and continuum states with the strong field. At this intensity,

the $1snp$ excited states lie above the laser-suppressed Coulomb barrier and the excited state lifetime is therefore very short. However, discrete absorption lines are still present near zero delay. Additionally, we observe two distinct dynamic features in the continuum states above the ionization potential ($I_p = 24.58$ eV). At negative delays, we observe a weak modulation of the absorption, following hyperbolic lines which indicate the previously observed direct-indirect interference in the continuum states [56]. These absorption structures appear as 45° lines in the Fourier transform analysis, with Fourier frequencies equal to $E - E_{1s2p}$, where E is the photon energy and $E_{1s2p} = 21.22$ eV. The direct-indirect interferences can be seen extending to photon energies of nearly 28 eV due to the high spectral resolution of the XUV spectrometer.

The most dominant feature, however, can be seen near zero delay. Here, we observe a shift in the absorption threshold that exhibits a strong half-cycle oscillation. This energy shift corresponds to the ponderomotive shift of the ionization potential. In this region, the periodicity of the oscillation does not change with the XUV photon energy, indicating that it is not a result of the direct-indirect interference. Moreover, it is inconsistent with the quantum beating observed in electron spectroscopy [56], which appear at negative delays with Fourier frequencies corresponding to energy level differences $E_{1snp} - E_{1sn'p}$ ($n, n' \geq 2$ and $n \neq n'$). Instead, this half-cycle oscillation is a clear evidence of a sub-cycle ponderomotive shift which follows the instantaneous laser intensity, analogous to the sub-cycle AC Stark shift [34, 35]. However, whereas the measurement of the sub-cycle AC Stark shifts by transient absorption is necessarily convoluted due to the relatively long lifetimes of the laser-dressed excited states [34, 35, 61] resulting in a relatively small modulation depth, the sub-cycle ponderomotive shift can be observed more clearly, as it relies on continuum states without finite lifetimes.

We turn our attention to the oscillating spectral features below the helium excited state manifold. In the figure below, we plot the simulated transient absorption of helium (including all bound states) using a dressing laser with $\omega_L = 1.7$ eV, three cycles pulse duration, and peak intensity of 5×10^{12} W/cm².

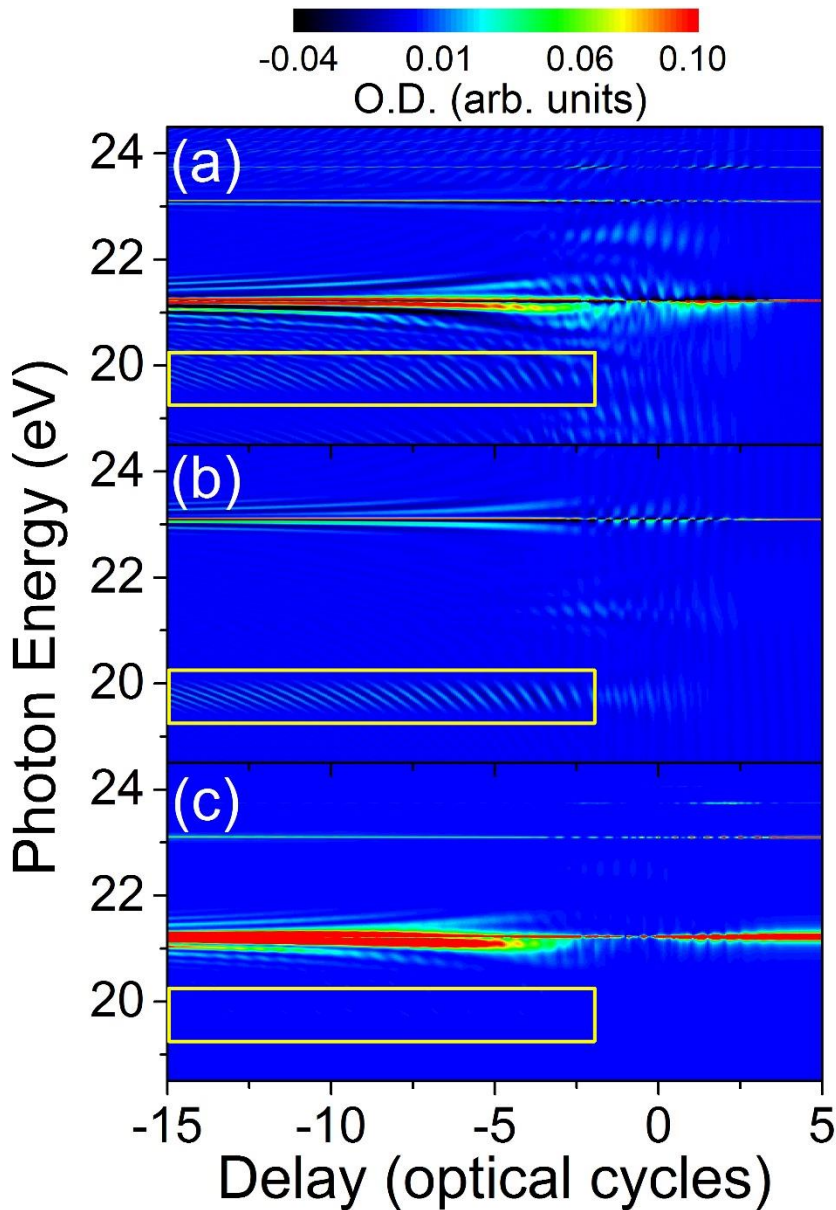


Figure 3-7 Interference in the delay-dependent absorption near 19.68 eV with a dressing laser frequency $\omega_L = 1.7$ eV. The full calculation in (a) includes the contributions from 16 bound states, and the half-cycle interference oscillations are indicated by the yellow box. In (b), the calculation has been repeated after removing the 1s2p, 1s4p, 1s5p, 1s6p, and 1s7p states. The presence of the interference oscillation near 19.68 eV suggests that it does not

result from quantum “which-way” interference, as no “direct” pathway is possible. In (c) the power spectrum $|\tilde{P}(\omega)|^2$ of the atomic dipole radiation is plotted for the same conditions as in (a), with all states included. The lack of the interference oscillations indicates an optical interference mechanism, as explained in the text.

We observe oscillations in the delay-dependent spectrogram which extend to large negative delays both near the ionization threshold (~ 24 to 25 eV) and below the $1s2p$ excited state energy (~ 19.5 to 20 eV). The features near the ionization threshold have been discussed in detail before [48, 62, 63], and have been attributed to quantum path interference in the population of $1snp$ Rydberg states. In this case, the high-lying $1snp$ states can be populated either directly by the attosecond pulse or indirectly via a three-photon (XUV+NIR+NIR) process wherein the attosecond pulse initially excites the $1s2p$ state. In the case of the low-energy feature, there is no clear “direct” pathway, though the photon energy of this feature does agree well with an indirect pathway via the $1s3p$ state ($E_{3p} - 2\omega_L = 19.68$ eV). Past experiments have indicated that removing either of the two pathways will quench the interference [63], suggesting that this feature results from another process. In Figure 3-7(b), we remove the possibility of another “direct” pathway by removing all $1snp$ states with the exception of $1s3p$. We find that the strong oscillations remain, both above and below the ionization threshold, in spite of the absence of quantum path interference.

To explain this feature, we propose that the observed interference does not arise from quantum path interference, but instead results from optical interference. Rather than two quantum paths, the delay-dependent oscillations stem from the interference between two coherent optical fields which contain the same photon energy, but which arrive on the detector at two different times. In particular, the interference feature at 19.68 eV can be understood as the

interference between the attosecond pulse transmitted by the medium and the dipole emission of the dressed atom. For a sufficiently thin target, we have:

$$\tilde{\epsilon}_{out}(\omega) \approx \tilde{\epsilon}_{in}(\omega) \left(1 + i \frac{2\pi\omega}{c} \frac{\tilde{P}(\omega)}{\tilde{\epsilon}_{in}(\omega)} NL \right) \quad (3-1)$$

which yields an intensity spectrum of:

$$|\tilde{\epsilon}_{out}(\omega)|^2 \approx |\tilde{\epsilon}_{in}(\omega)|^2 \left[1 + \left| \frac{2\pi\omega}{c} \frac{\tilde{P}(\omega)}{\tilde{\epsilon}_{in}(\omega)} NL \right|^2 - \frac{4\pi\omega}{c} \Im \left[\frac{\tilde{P}(\omega)}{\tilde{\epsilon}_{in}(\omega)} \right] NL \right] \quad (3-2)$$

Here, the first term represents the spectrum of the attosecond pulse, the second term is the intensity spectrum of the polarization field, and the third term represents the interference between the two. In the figure below, we plot the polarization spectrum intensity (second term), which is found not to exhibit the sub-cycle oscillations, indicating that this feature arises from the interference term, which is directly proportional to the absorbance. Interestingly, the oscillations above 24 eV are also nearly absent, suggesting that the interference oscillations in the vicinity of the ionization threshold of helium may also not result from pathways involving the high-lying $1snp$ Rydberg states, though it is important to note that such intermediate resonances may enhance the optical interference process and that our calculations neglect the contributions of continuum states.

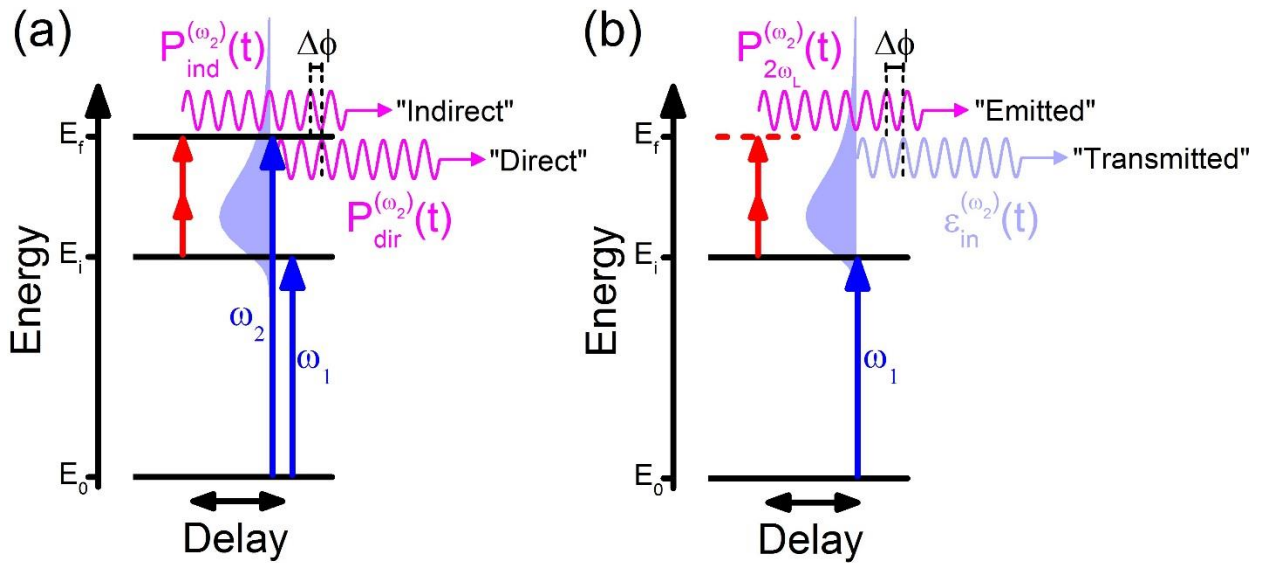


Figure 3-8 Comparison of “which-way” and optical interference models. (a) In the “which-way” interference, the final state can be excited both by the attosecond pulse alone (“direct”) and by the combined attosecond and NIR laser fields (“indirect”). Each of these excitation pathways induces a time-dependent dipole, $P_{dir}^{(\omega_2)}$ and $P_{ind}^{(\omega_2)}$ respectively, which both oscillate with the frequency $\omega_2 = E_f - E_0$. Depending on the delay, these two components may add up constructively or destructively, leading to a modulation of the measured signal. (b) In the optical interference, there is no state with energy E_f , and therefore the component of the attosecond spectrum (pale blue shaded) with frequency ω_2 does not induce dipole emission on its own. When the NIR laser is present, the state with energy E_i forms sidebands resulting in the emission with frequency ω_2 . This laser-induced dipole radiation (“emitted”) will interfere with the “transmitted” components of the attosecond spectrum with frequency ω_2 , leading to a delay-dependent modulation in the measured signal. Blue arrows indicate atomic transitions initiated by the attosecond pulse (with spectrum indicated by the pale blue shaded area), while red arrows indicate transitions resulting from the NIR pulse. Magenta sinusoidal arrows indicate the dipole emission with frequency ω_2 , while the pale blue sinusoidal arrow indicates the transmitted component of the attosecond spectrum.

The absorption of light is a fundamental process which can be used to initiate chemical reactions [64] or as a basis for lightwave electronics [65]. Here, we show that a moderately intense (10^{11} - 10^{13} W/cm²) laser field can control the absorption of light on the attosecond timescale. When overlapped in space and time with a few-cycle laser field, new features in the absorption spectrum of an isolated attosecond pulse appear, corresponding to two- and three-photon excitation to bound states which cannot be populated by the XUV pulse alone. These

absorption features can be “gated” on the half- and even quarter-cycle timescale by changing the delay between the two pulses, allowing for all-optical switching on the attosecond timescale.

3.2 Sub-cycle Electron Dynamics and Quantum Interferences of Attosecond Transient Absorption of Neon Atoms

In the previous session, we discussed the attosecond transient absorption experiment in helium atoms which is a relatively simple atom system with few interacting energy levels. For this reason, the experiments could be interpreted relatively easily, using a three-level atom [5, 66-68] or other model systems [35, 48] to explain most of the features of experiments. For ATA experiments in bound states of helium atoms, *ab initio* solutions of the time-dependent Schrödinger equation (TDSE) have also been obtained [48, 60, 62], which have helped to verify the existing theory and to illustrate several previously unexplained features. However, helium atoms have simple energy levels which are solvable with very high precision in principle and could be treated very well with single-active-electron (SAE) approximation. Therefore, our current theory needs to be further examined by ATA experiments with more complex atoms before we can apply it to molecules or condense matter.

In this session, we extended the attosecond transient absorption spectroscopy technique to a more complex atom system - neon atoms – in which ten electrons are involved in an atom, so the previous theory for ATA technique based on SAE approximation is highly challenged. Using neon as the target gas, we observed laser-induced AC Stark shifts and quantum interferences between different multi-photon excitation pathways, which is similar to those features observed in helium attosecond transient absorption spectrum. Theoretical calculations from TDSE with SAE approximation reproduced the experiments result quite well. In addition we confirmed by

both experiment and calculation that the quantum interference result from two distinct pathways of excitation to a final state.

Neon is a more complex noble gas with ground configuration $1s^2 2s^2 2p^6$, and higher energy levels with the excitation of one valence electron results configuration of $1s^2 2s^2 2p^5 nl$. Its energy levels of interest along with measured absorption cross section are shown in the figure below.

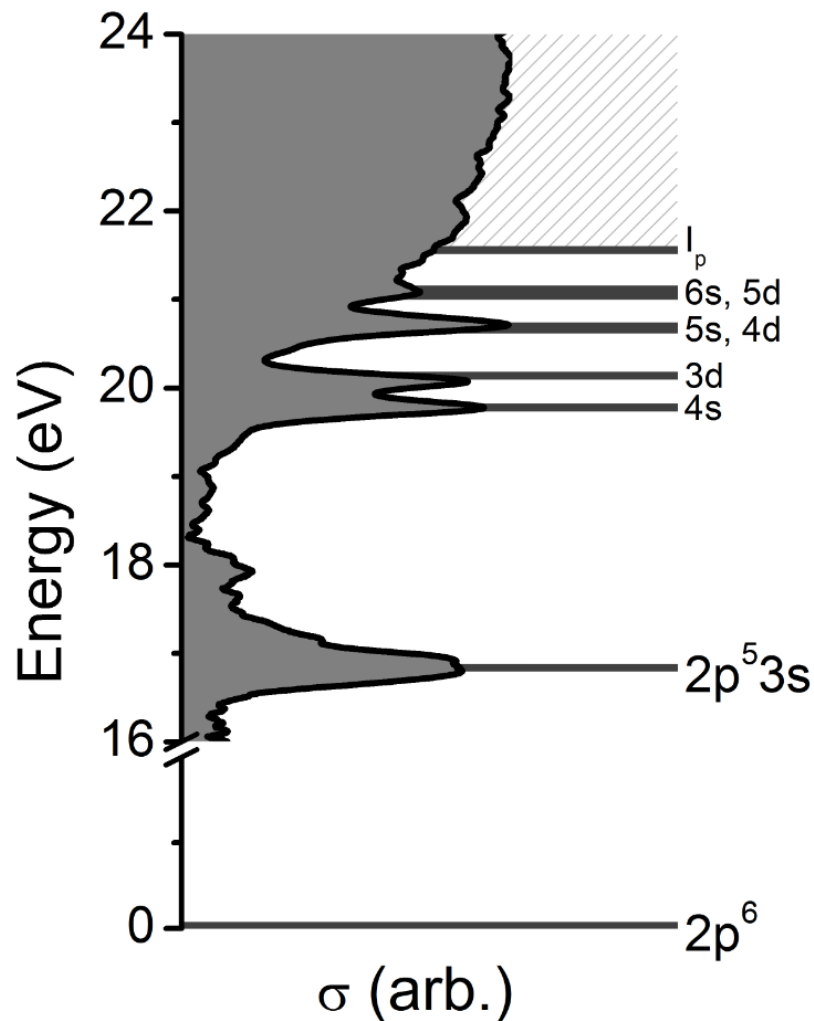


Figure 3-9 Measured absorption cross section of neon atoms (black curve with gray filled area) and atomic energy levels of interest. The electron configurations are marked for each identified. Adapted from [63]

According to dipole selection rules, single XUV photon absorption by neon atoms will cause a valence electron transit from ground $2p$ state to ns or nd bound states or to the continuum, which can be experimentally measured as absorption cross section, as indicated in the figure above. When a moderately intense NIR laser field is introduced, as is the case in ATA experiments, the corresponding energy level splitting and shifting can be directly observed through changes in the positions and shapes of the absorption features. Furthermore, time-dependent absorption measurements enable us to resolve in time domain the evolution of atom energy levels under perturbation of NIR laser field.

The experiment was performed on the attosecond transient absorption setup that was used for the helium experiment [48]. The target cell was filled with 40 torr of neon gas and $\sim 75\%$ of the spectrum above neon ionization threshold was absorbed. By changing an iris diameter, we could control the pulse energy of NIR laser pulses as well as the focal spot size. The delay between the two arms was controlled by a piezo-electric transducer (PZT). A CW green laser that copropagated in both arms was used to stabilize and control the delay between the two pulses [28]. The delay stability was locked to within 50 attosecond RMS for the entirety of the measurement, while the delay step size is 141 as. The carrier-envelope phase was not of significant importance in our experiments since the generated single attosecond pulses were synchronized to the dressing NIR pulses [1].

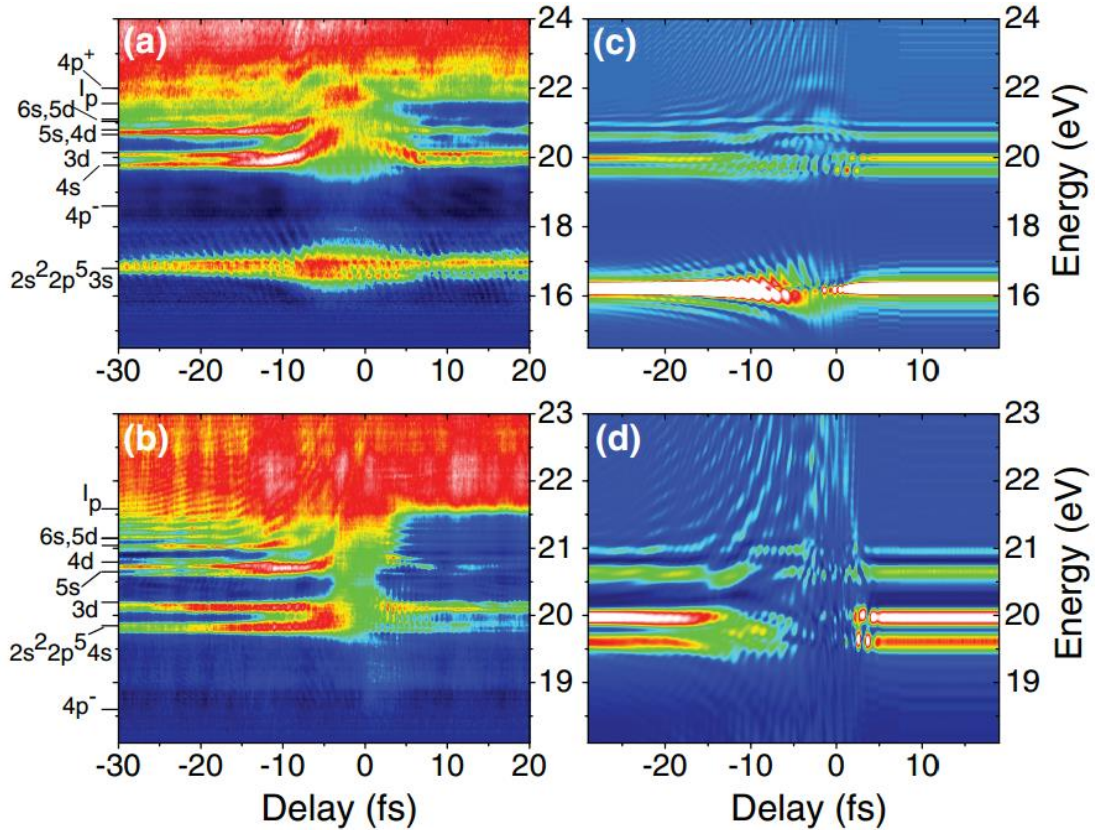


Figure 3-10 Measured delay-dependent absorbance spectra with a dressing laser intensity of (a) ~ 10 TW/cm² and (b) ~ 75 TW/cm² (b). Panels (c) and (d) show the calculated absorption cross sections for dressing laser pulses 4 fs in duration and with the same intensities as in panels (a) and (b). Adapted from [63]

The measured absorbance spectrum of neon atoms perturbed by 10 TW/cm² laser pulses as a function of time delay between pump and probe pulses is shown in the figure above. When the time delay is negative, where the attosecond pulses arrived at the absorption cell before the NIR pulses, we can see several absorption lines corresponding to electron transitions from ground state to certain excited states which are marked in the figure. The spectrum of the single attosecond pulses is broad, bound states and continuum absorption can be observed simultaneously. As NIR pulses are adjusted by the delay controlling PZT to be close to the single attosecond pulse, the energy levels exhibit some interesting features. First of all, the absorption cross section in the vicinity of $1s^22s^22p^53s$ state oscillates with half of the NIR cycle – 1.3 fs.

Secondly, half cycle oscillation in addition to strongly AC stark shift is observed for higher excited states near zero delay, as is also observed in helium atoms and explained by Chini et. al.[48]. Thirdly, light induced structure near 22 eV around zero delay was observed. At last, the ionization threshold do not show up until positive delay. This is likely because that the higher excited states of neon atoms can be easily ionized by one NIR photon absorption. To see this area more clearly, we increased the NIR laser intensity up to 75 TW/cm², with which one NIR photon ionization of highly excited states is much stronger. And the XUV spectrometer was optimized to concentrate on higher excited energy levels near ionization threshold. The delay dependent absorption spectrum are shown, in which tons of parabolic interference lines are observed above 21 eV in negative delay. This is previously interpreted as quantum interference as a result of direct-indirect transition in helium atoms [48].

The theoretical treatment is done with an effective method based on Floquet theory []. This part of work is collaborated with Dr. Xiaomin Tong. With this method, the IR-assisted photoabsorption cross sections can be calculated as:

$$\sigma(\omega_p) = \frac{4\pi\omega_p}{c} \text{Im} \int_0^\infty iC(t) e^{i(\omega_p + \epsilon_g)t - \eta t} dt \quad (3-3)$$

where, $C(t)$ is a generalized autocorrelation function defined as:

$$C(t) = \frac{1}{T} \int_0^T \langle \Psi(t=0, \tau) | \Psi(t, \tau) \rangle \quad (3-4)$$

The wave function $\Psi(t, \tau)$ is obtained from time-dependent Schrodinger equation in which the Hamiltonian takes the form of $H(t, \tau) = H_0 + V(t+\tau)$. τ is a time shift which

corresponds to an initial phase $\delta = \frac{2\pi\tau}{T}$. $\Psi(t, \tau)$ is obtained using the split-operator method

with the generalized pseudospectral grid in the energy representation for a given $H(t, \tau)$ with the initial wave function as $|\Psi(t=0, \tau)\rangle = d|\Psi_g\rangle$. The method is equivalent to the time-independent Floquet method but the details of the Floquet wave function are not explicitly required.

Our calculated photoabsorption cross section for neon atoms as a function of IAP-NIR delay are shown in Figure 3-10 (c) and (d), corresponding to NIR intensity of 10 TW/cm² and 75 TW/cm² respectively. All the predominant features reappear in our calculation. Note that the calculated energy levels of neon atoms are slightly off their actual position due to limited box area used in the calculation. However, the behaviors of each energy level are similar to what is observed in the experiment, such as the half cycle oscillation in 1s²2s²2p⁵3s state (16.8 eV).

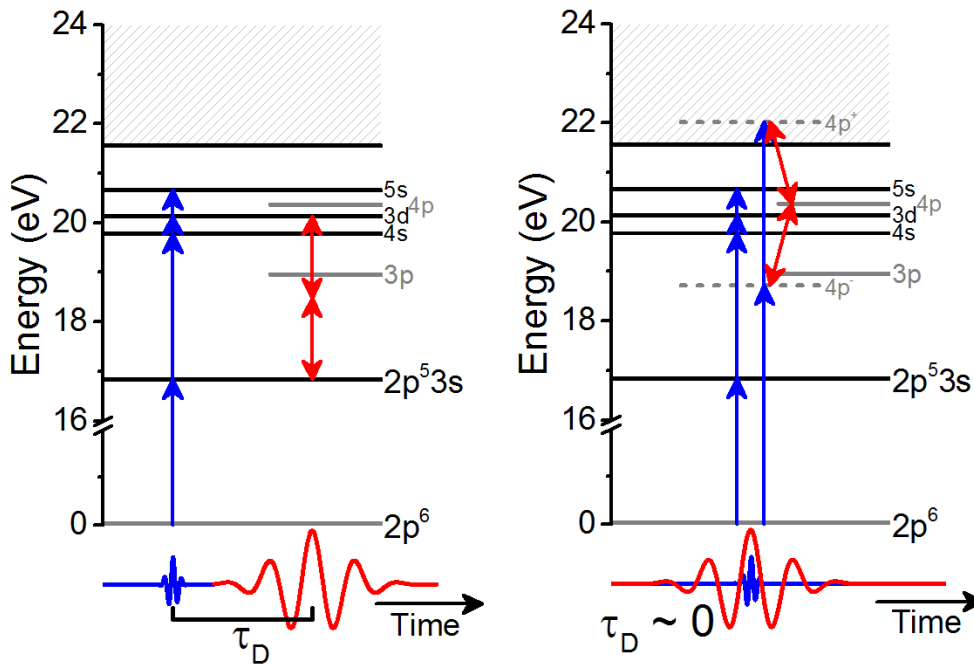


Figure 3-11 Diagram of direct and indirect pathways resulting in quantum interferences in the (a) 3s and (b) 4p⁺ absorption lines. Energy levels indicated by black lines are accessible by one XUV photon absorption, while gray levels are forbidden by selection rules. Dashed gray energy levels in (b) indicate Floquet-like sidebands of the 4p energy level. Adapted from [63]

There are two distinct pathways for electron to transit from ground state to 3s state. When IAPs arrived at the absorption cell, one XUV photon absorption resulted in excitation of several ns and nd states, one of which is 3s. This is termed as direct pathway. There are also some population in 3d states (20.1 eV) which is about two NIR photon energy higher than 3s state. A certain delay time τ_d later, came the NIR pulses, which caused the 3d state transit down to 3s state by emitting two NIR photons. This is the indirect pathway. These two pathways finally lead to an interference in the absorption cross section. The light induced structure in Figure 3-10 (a) and (b) near 22 eV is localized around zero delay, since a dark state 4p which cannot be populated directly by one XUV photon absorption is involved. This process is diagrammed in Figure 3-12(b). Under moderately intense laser field, 4p state have two Floquet sidebands located evenly with one NIR photon energy away from 4p. Therefore, except for the direct pathway by an XUV photon absorption to the $4p^+$ state (ionization), there exists another indirect pathway: an XUV photon absorption to $4p^-$ followed by two NIR photon absorption to the final $4p^+$ state.

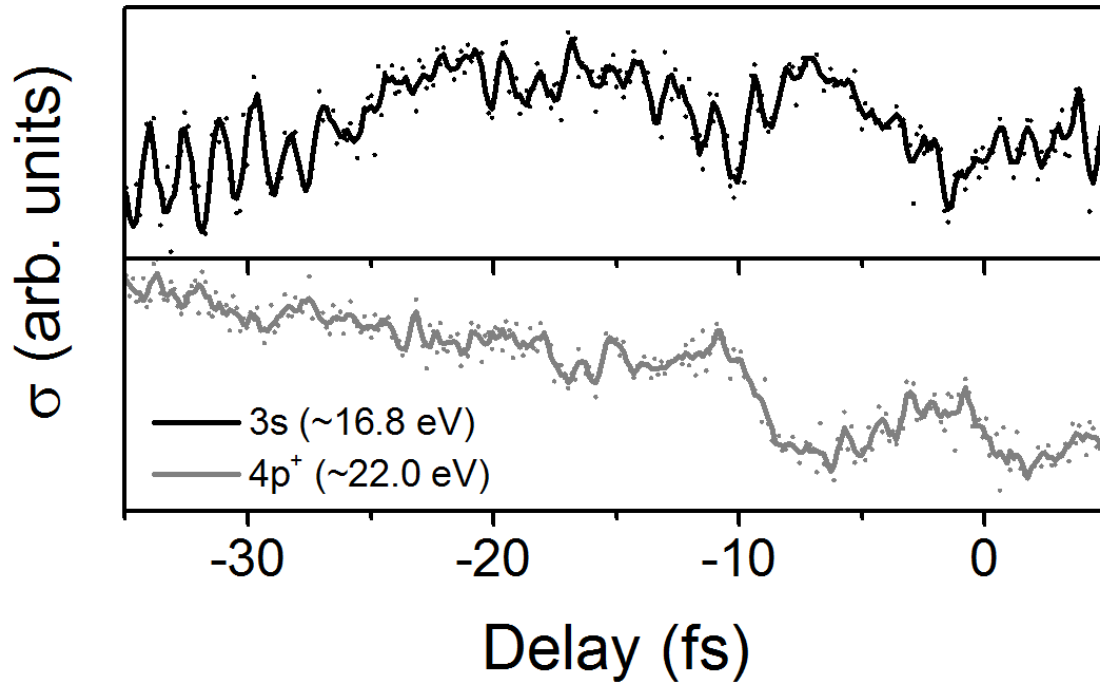


Figure 3-12 Measured absorption cross sections in the vicinity of the 3s (black) and 4p⁺ (gray) absorption lines. The dots indicate the experimentally obtained data points, whereas the solid lines are smoothed to show the major features. Whereas half-cycle (~1.3 fs) oscillations can be observed in the 3s absorption lines extending to large negative delays, oscillations in the 4p⁺ absorption can only be observed for delays between 0 and -7 fs. Adapted from [63]

This also leads to interference in absorption cross section which can be seen in Figure 3-12(c) (gray curve). Note that Floquet sidebands exist only if laser is present, so the light induced structure as well as the corresponding interference shows up only near zero delay.

Previously, the role that a certain state plays in ATA experiment can be identified by a test calculation which dynamically eliminates the state during the time propagation of the TDSE. Here, we adopted an experimental way to confirm the origin of the interference in the vicinity of 3s state by suppressing the indirect pathway. The aluminum filter used to filter out the IAPs was replaced with a 200 nm thick indium filter which allows transmission of XUV pulses within the

spectrum range from 11 eV to 17 eV. So only the direct pathway for the excitation of 3s state is feasible, while the indirect way was turned off due to lack of XUV photons to populate electrons to 3d state. Figure 3-13(a) shows the result ATA cross section, in which no quantum interferences are observed, and calculated cross section shown in Figure 3-13 (b) is in great agreement with the experiment result. This is a direct evidence from experiment that the observed quantum interference come from the coupling between higher excited states (3d) and 3s state by NIR laser. Instead, we can see a clearly symmetric energy splitting near the IAP-NIR overlap region. This is called Autler-Town splitting, which is caused by resonance coupling between 3s and 3d state. Although the population of 3d state initialized by indium filtered IAPs is zero, the transition from 3s to 3d by absorbing two NIR photons is still possible.

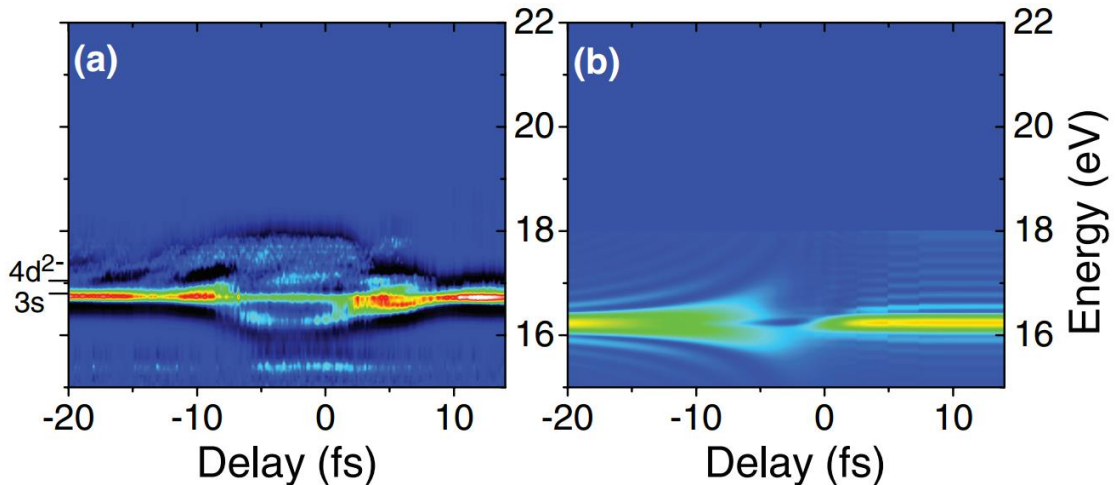


Figure 3-13 Measured (a) and calculated (b) delay-dependent absorbance spectrum with isolated attosecond pulses filtered by indium filter which allows transmission of XUV pulses within the spectrum range from 11 eV to 17 eV. Autler-Town splitting instead of quantum interference was observed. Adapted from [63]

In conclusion, we measured the transient absorption of an isolated attosecond pulse by laser-dressed bound states of neon atoms. Although lots of electrons are involved, the theory

treatment based on SAE approximation is still be able to reproduce the experimental result. The observed sub-cycle changes in the neon absorption spectrum result from both laser-induced AC Stark shifts and from quantum interferences between different multi-photon excitation pathways. Light induced structure was also observed and well predicted by our theory. Furthermore, we saw experimental evidence that the indirect pathway to 3s state via 3d state plays a role in the quantum interference in the vicinity of 3s state. The presented neon ATA experiment along with our theory pave the way to extend ATA technique to more complex system.

CHAPTER 4 - ATTOSECOND TIME-RESOLVED AUTOIONIZATION OF ARGON AND KRYPTON ATOMS

Note: Portions of this chapter were used or adapted with permission from the following:

(1) He Wang, Michael Chini, Shouyuan Chen, Chang-Hua Zhang, Feng He, Yan Cheng, Yi Wu, Uwe Thumm, and Zenghu Chang. Attosecond Time-Resolved Autoionization of Argon. *Phys. Rev. Lett.* 105, 143002 (2010)

(2) Michael Chini, Xiaowei Wang, Yan Cheng and Zenghu Chang. Resonance effects and quantum beats in attosecond transient absorption of helium. *Journal of Physics B: Atomic, Molecular and Optical Physics*, 47, 124009 (2014)

(3) Yan Cheng, Michael Chini, Xiao-Min Tong, Andrew Chew, Julius Biedermann, Yi Wu, Eric Cunningham, and Zenghu Chang. Quantum Beats in Attosecond Transient Absorption of Krypton Autoionizing States. *CLEO: 2015*, paper FTh3C.3

The recent advance in the attosecond pulse generation has made the observation of real time electron dynamics possible. Autoionization in argon and krypton atoms was studied experimentally by transient absorption spectroscopy with isolated attosecond pulses. The peak position, line shape and population of the resonant states were modified by intense near infrared (NIR) laser pulses as the delay between attosecond pulse and NIR laser was scanned.

4.1 Attosecond time resolved autoionization of argon

Fano resonances in the photoabsorption cross sections of atoms are the signature of the autoionization process, which is governed by electron-electron correlation [46]. In multi-electron systems, discrete states are embedded in the continuum state under independent particle picture.

Because of the configuration interaction, the discrete state is coupled with continuum state and the Fano peaks in the absorption spectrum are the result of interference between the direction ionization to the continuum state with the decay from the autoionizing states. Although the autoionizing states in strong laser field has been theoretically predicted thirty years ago [69], the synchrotron pulse duration is too long (100 fs to 100 ps) to probe Fano resonances exposed to an external strong field in the time domain since the autoionizing state of noble gases can be as short as few femtoseconds. Since the generation of the first isolated attosecond pulses in 2001 [70], it was theoretically proposed and experimentally demonstrated that time-resolved Fano profiles can be studied by attosecond streaking technique [71-74]. Here we report results of the transient absorption experiment on the autoionization process with isolated attosecond pulses in argon atoms.

The absorption cross-section of autoionization state is usually described by the Fano formula as:

$$\sigma(E) = \sigma_a \frac{(q + \varepsilon)^2}{1 + \varepsilon^2} + \sigma \quad (4-1)$$

where $\varepsilon = (E - E_r)/(\Gamma/2)$ is the reduced energy defined in terms of the resonance energy E_r and the natural width Γ of the resonance. The natural width Γ determined the decay rate of the resonance through autoionization, which is related with the life time τ of the autoionizing state by $\tau = \hbar/\Gamma$. The q parameter represents the ratio of transition amplitude from ground state to autoionizing state to the transition amplitude of excitation of continuum.

A diagram of the argon autoionizing states of interest is depicted in the figure below. The line width Γ of the $3s3p^64p$ state and $3s3p^65p$ state are 80 meV and 28 meV respectively, which

correspond to life time of 8.2 fs and 23.5 fs. They are orders of magnitude shorter than synchrotron pulses, therefore the real time control of autoionization state demands attosecond pulse as a trigger.

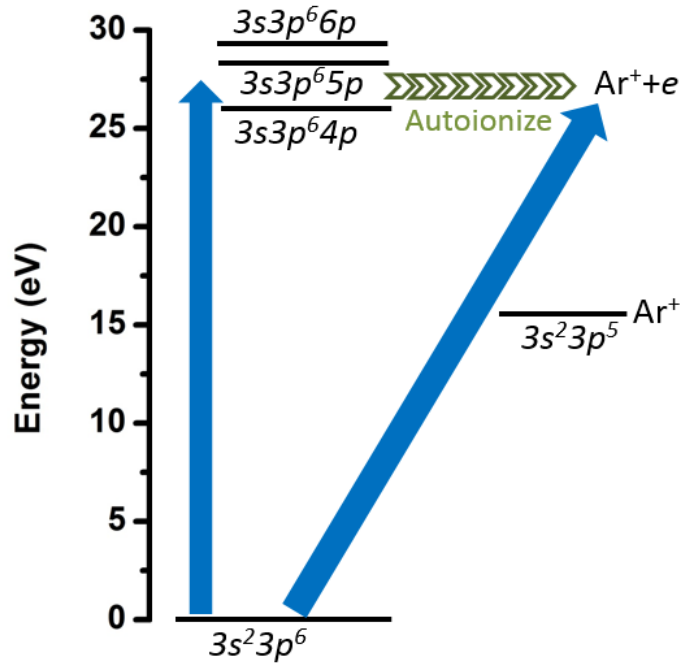


Figure 4-1 Energy diagram of the $3s3p^6np$ 1P autoionizing states in argon. The continuum spectrum of the attosecond pulse covers the 1P series of states. Adapted from [5].

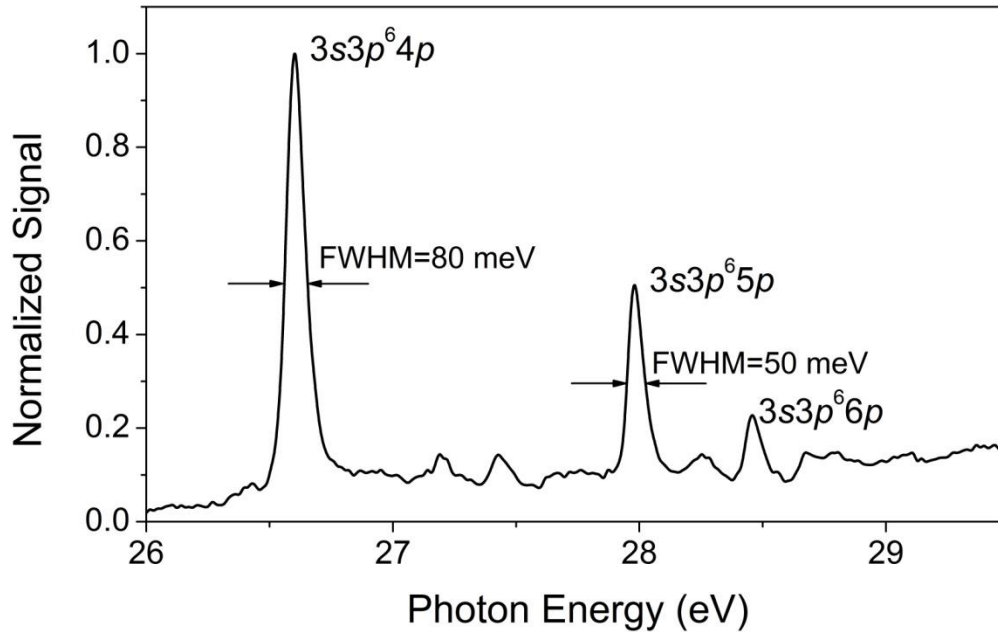


Figure 4-2 Transmitted XUV spectrum indicating argon $3s3p^6np$ 1P autoionizing states. The spectrometer resolution was 50 meV. Adapted from [5].

To control and measure the real time autoionization states of argon atoms, a pump-probe scheme with a Mach-Zehnder configuration was used in the experiment. 1 KHz, 2.5 mJ pulses from a carrier envelope phase (CEP) stabilized regenerative amplifier (Legend Due Core TM) was focused into a hollow core fiber with 400 μm inner diameter filled 1.5 atm of neon gas. After spectral broadening and the pulse compression by chirped mirrors, a 0.8 mJ, 8 fs NIR output pulse centered at 750 nm was split into two parts. Half of the beam generated the isolated attosecond pulse using the generalized double optical gating (GDOG) [27] from Ar, and the corresponding XUV supercontinuum spectrum covered the energy range between 20 eV and 40 eV. Measurements with an attosecond streak camera confirmed the pulse duration to be ~ 130 as. After filtered out by 300 nm Al foil the XUV beam was focused by a toroidal mirror to a second gas cell with a 1 mm inner diameter filled with 25 torr of Ar gas where the absorption occurs. The XUV spot size was estimated to be 30 μm and the Rayleigh range. Meanwhile, the other half of the NIR beam was recombined collinearly with the attosecond pulse at the second gas cell

by a hole-drilled mirror which reflected the NIR and allowed the XUV to pass, a lens with $f=400$ mm was used to focused the NIR, and it spatially and temporally overlaps with the XUV focal spot at the second cell. Delay between the NIR and XUV pulses was introduced by a piezo-electric transducer. A CW green laser was co-propagated in both arms of the interferometer to stabilize and control the delay between the NIR and XUV pulses with 22 as precision [28]. The transmitted XUV spectrum was refocused by a spherical mirror at 2 degree grazing incidence angle and dispersed by a transmission grating (2000 lines/mm). The MCP phosphor stack was used to capture the image XUV spectrum. The spectrometer resolution was measured to be 50 meV with the reference of $3s3p^65p$ state, which is smaller than the width of the $3s4p^64p$ resonance peak.

The figure below shows the experimental results. In the plot, negative delay corresponds to the situation where the XUV pulses arrive on the argon target before the NIR pulses. Three resonance peaks $3s3p^64p$, $3s3p^65p$, and $3s3p^66p$ can be identified. As the time delay approaches zero, the NIR pulse gradually shifts the positions of the first two resonance peaks to higher photon energy.

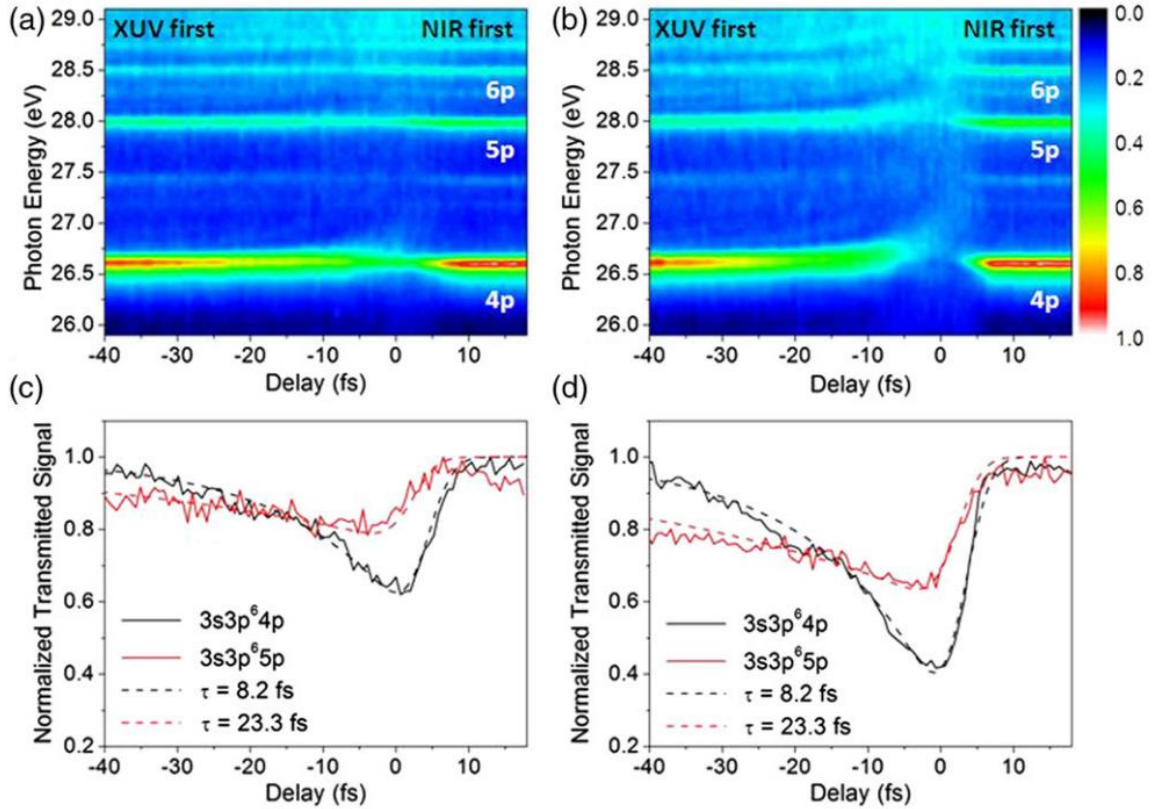


Figure 4-3 Transmitted attosecond XUV spectra of argon in a strong NIR laser field with a peak intensity of (a) 5×10^{11} W/cm² and (b) 10^{12} W/cm². Negative delays correspond to the attosecond pulse arriving on the target before the NIR laser pulse. The resonance peaks are shifted, broadened, and weakened when the two pulses overlap. (c), (d) Transmitted signal (solid) near the $3s3p^6 4p$ and $3s3p^6 5p$ states for 5×10^{11} W/cm² and 10^{12} W/cm², respectively, and calculated exponential decay convoluted with 4.5 fs Gaussian for best fit (dashed). Adapted from [5].

Figure 4-3 (c) plots the total count of the $3s3p^6 4p$ peak as function of delay. When the XUV and NIR are overlapped, the transmission corresponding to the autoionizing state is minimized, which can be considered as a new type of electromagnetic induced transparency that occurs on a femtosecond time scale. This phenomenon can be understood as multiphoton ionization of the resonance state ($3s3p^6 4p$ 26.61 eV), which has a binding energy of less than 3 eV, by the NIR laser pulse. The NIR intensity is estimated to be $\sim 10^{13}$ W/cm² at the second gas cell, which is more than sufficient for the depletion of the population of the excited state through

multiphoton ionization. At $\sim 10^{12}$ W/cm, we found the depletion of the resonance states to be weaker. When a portion of an excited state population is depleted, the contribution from the autoionization to the Fano interference is smaller, which leads to a weaker Fano peak.

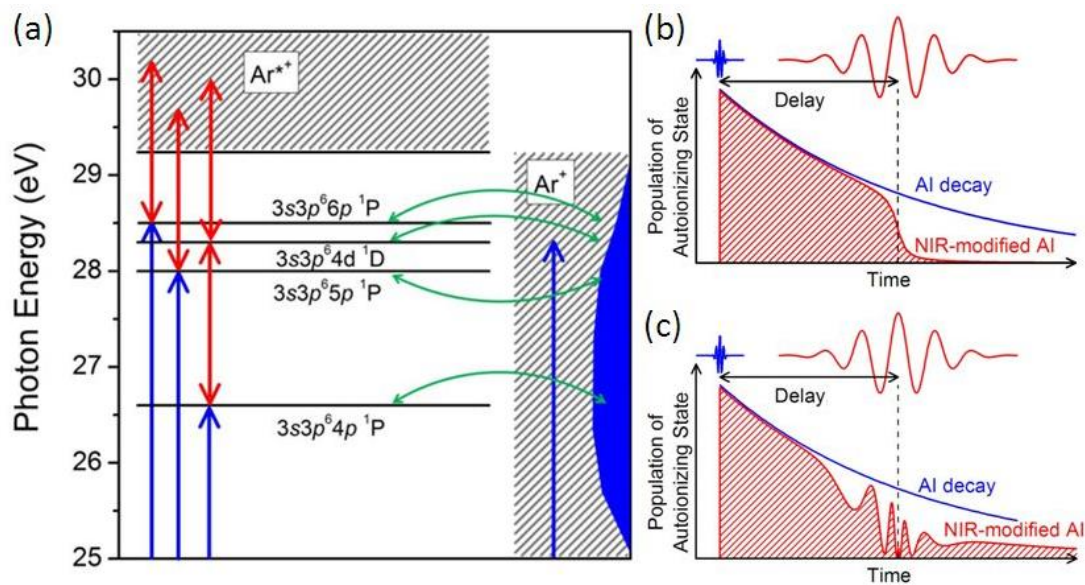


Figure 4-4 (a) Schematic representation of argon autoionizing states exposed to the strong NIR laser field. The blue arrows indicate the attosecond XUV excitation of the ground state to the $3s3p^6np\ ^1P$ states as well as to the $Ar^+ (3s^23p^5\epsilon l)$ continuum. The red arrows indicate the NIR laser coupling between the autoionizing states and the $Ar^{*+} (3s3p^6\epsilon l)$ continuum or to $3s3p^6nl$ autoionizing states. The configuration interaction (green arrows) couples all autoionizing states to the Ar^+ continuum. (b) Autoionization decay modified by NIR laser-induced coupling to the $Ar^{*+} (3s3p^6\epsilon l)$ continuum. Ionization by the NIR field truncates the autoionization decay, resulting in a shorter lifetime and a broader, shifted resonance peak. (c) Autoionization decay modified by NIR laser-induced coupling to $3s3p^6nl$ autoionizing states. Rabi oscillation between the two states results in AC Stark-like splitting. Adapted from [5].

We observed several new features in autoionization of argon with attosecond transient absorption spectroscopy that could not be measured with synchrotron radiation. The capability of synchronizing an intense 8 fs NIR pulse and a 130 as XUV pulse on an argon gas target allows us to control the autoionization process with a lifetime of less than 10 fs. It was found that the

NIR laser field causes changes to the resonance peak shape and a reduction in the transmission, and that these features depend strongly on the laser intensity. The shift and broadening of the Fano resonance peak in the laser field are discovered for the first time to the best of our knowledge.

In reality, the coupling can be complicated, as additional quasi-bound states ($3s3p^6nd$), which cannot be observed by the absorption of a single XUV photon, is in the same energy range as the $3s3p^6np$ 1P manifold of states. However, such states can be accessed by two photon (XUV+NIR) processes. In particular, the $3s3p^64d$ (28.3 eV) state lies 1.7 eV above the $3s3p^64p$ state we detect [75], which is approximately equal to the central photon energy of the NIR laser pulse. When the two states are strongly coupled together in resonance with the NIR photon, Rabi oscillations and autoionization can result in complicated Fano interference profiles, which includes the AC Stark shifting and splitting [69, 76]. This NIR-laser induced interference of two (or more) autoionizing states can dramatically change their uncoupled decay widths. This may explain the much stronger shift and splitting for the $3s3p^64p$ state as compared to the higher-lying states. Furthermore, as is shown in the trace of the shift, the strongly shifted $3s3p^64p$ resonance peak suddenly disappears once the energy approaches 27.7 eV. We tentatively attribute this to the fact that the continuum energy threshold, which will experience only the smaller non-resonant AC Stark shift, lies ~ 1.5 eV above the shifted peak of the $3s3p^64p$ state indicated near zero delay. The $3s3p^64p$ state can then be coupled to the continuum directly, speeding up the decay process and resulting in the observed asymmetry of the $3s3p^64p$ state with respect to zero delay.

Simulations of the argon attosecond transient absorption experiment are performed using the formalism in Ref.[69, 76]. In this simulation, we ignored the $3s3p^65p$ and $3s3p^66p$ states as

well as the $\text{Ar}^{*+} (3s3p^6\epsilon l)$ continuum state, but preserved the coupling to the $\text{Ar}^+ (3s^23p^5\epsilon l)$ continuum via configuration interaction. The simulated delay-dependent spectra are shown in the figure below for NIR laser intensities of 5×10^{11} and 1×10^{12} W/cm^2 , respectively. Features including the asymmetric splitting, broadening, and weakening of the Fano lineshape, are well reproduced.

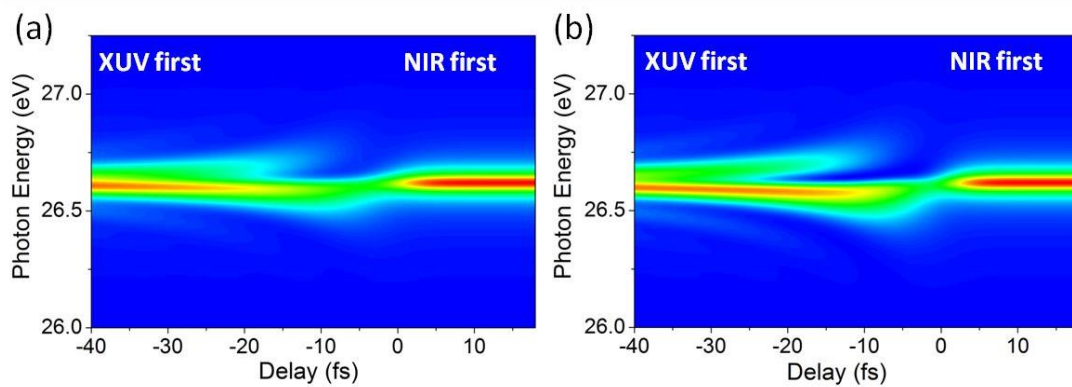


Figure 4-5 Simulated dipole radiation spectrum of laser-induced coupling of the $3s3p^64p$ and $3s3p^64d$ autoionizing states. The XUV laser had a pulse duration of 140 as and intensity of 10^{10} W/cm^2 . The NIR laser had a pulse duration of 8 fs and intensity of (a) 5×10^{11} W/cm^2 and (b) 10^{12} W/cm^2 . Adapted from [5].

Compared with the photoelectron measurement in the attosecond streaking experiments, transient photoabsorption measurements have higher data collection efficiency and better energy resolution. Attosecond transient absorption is a pure optical measurement, with a much simpler set-up than an attosecond streak camera. The measurement demonstrates full control of the autoionization process with attosecond precision.

4.2 Quantum Beats in Attosecond Transient Absorption of Krypton Autoionizing States

In previous photoelectron measurements [56], the quantum beats were attributed to electrons which were initially excited by the attosecond pulse to different $1snp$ states, and subsequently ionized by the dressing laser pulse to the same final state in the continuum. The quantum beats therefore arise from the field-free evolution of the excited state wavepacket in the time interval between the two pulses. In the case of attosecond transient absorption, however, the final state is typically a bound state, and so the conditions for observing the quantum beating are somewhat different. Rather than observing the quantum beats in the absorption spectrum above the ionization threshold, we expect that the wavepacket motion may be imprinted as a slow variation on the absorption in the vicinity of the excited state energy levels. Here, we propose a mechanism by which the quantum beating of the $1s4p$ and higher-lying states can be observed in the transient absorption in the vicinity of the $1s2p$ absorption line. Because the bandwidth of the dressing infrared laser is large, the $1s4p$ and higher-lying states can be coupled to the $1s2p$ state through the emission of two photons within the spectrum of state-of-the-art few-cycle Ti:Sapphire lasers. For example, population initially excited to the $1s5p$ and $1s6p$ states can be transferred to the $1s2p$ state via stimulated emission of two 876 and 829 nm photons, respectively. In Figure 4-6, we simulate the attosecond transient absorption of the $1s2p$ state coupled to the $1s5p$ and $1s6p$ states. For simplicity, only the $2p$, $3s$, $5p$, and $6p$ energy levels were included in the calculation. Figure 4-6 (a) shows the attosecond transient absorption spectrogram, which exhibits relatively slow oscillations with a superimposed half-cycle modulation. To guide the eye, we have also plotted a sinusoidal oscillation with a period equal to the quantum beat period of the $1s5p$ and $1s6p$ states, $T_{5p,6p} = 2\pi/|E_{6p} - E_{5p}| = 25.83$ fs, which

is in good agreement with the slow oscillations on the high-energy side of the 1s2p resonance. In Figure 4-6 (b) we have integrated the absorbance spectrum within a small energy window (21.25 to 21.28 eV) just above the 1s2p resonance, and find that the quantum beat results in a strong modulation of the absorption in the vicinity of the 1s2p energy level.

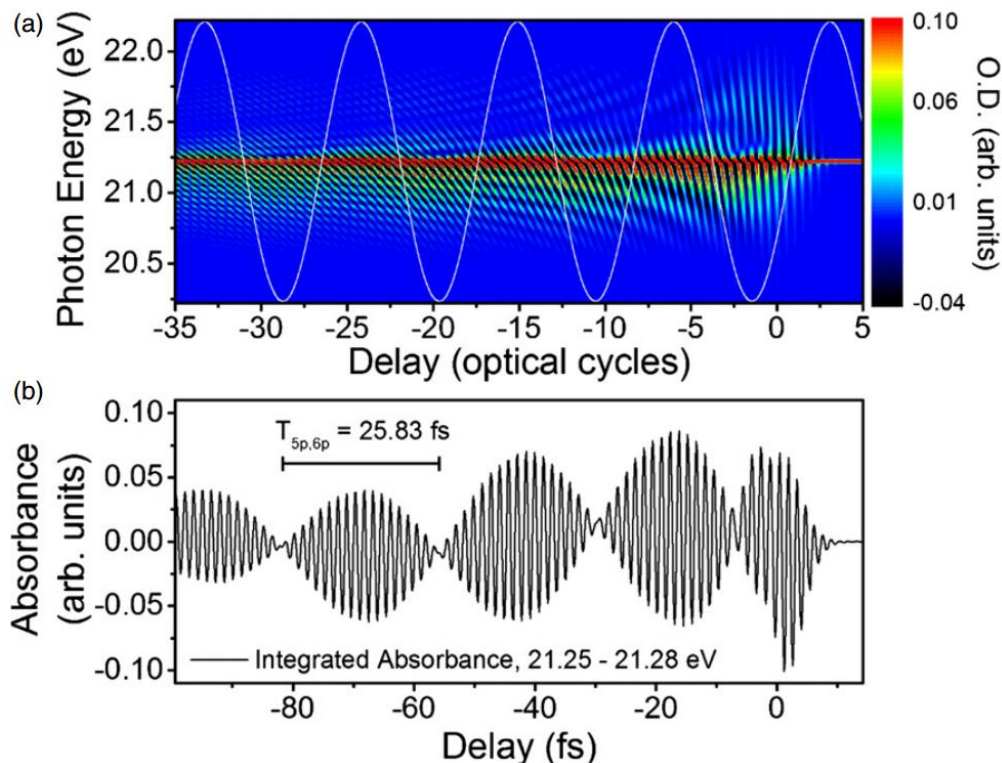


Figure 4-6 Quantum beats in the delay-dependent absorption near the 1s2p excited state with a reduced excited state basis set consisting of the 1s2p, 1s3s, 1s5p, and 1s6p states. Relatively slow oscillations are present on the high-energy side of the 1s2p absorption line in (a) with periodicity equal to that of the quantum beating of the 1s5p and 1s6p state (white curve). The integrated absorbance from 21.25 to 21.28 eV in (b) clearly shows the quantum beat effect with a periodicity of 25.83 fs. Adapted from [77].

Such slow oscillations are clearly present in previous transient absorption measurements, but unambiguous identification of the quantum beats will require measurements over a much larger range of negative delays. Because clear observation of the quantum beat requires sufficient

population to be transferred from the 1s5p and 1s6p states to the 1s2p state, in these calculations we have intentionally modified the attosecond pulse spectrum, so that the spectrum in the vicinity of the 1s5p and 1s6p states is ~10 times stronger than in the vicinity of the 1s2p state. Such modifications can be achieved experimentally by using suitable foil filters [63], as has previously been demonstrated in attosecond transient absorption, or by using multilayer XUV mirrors.

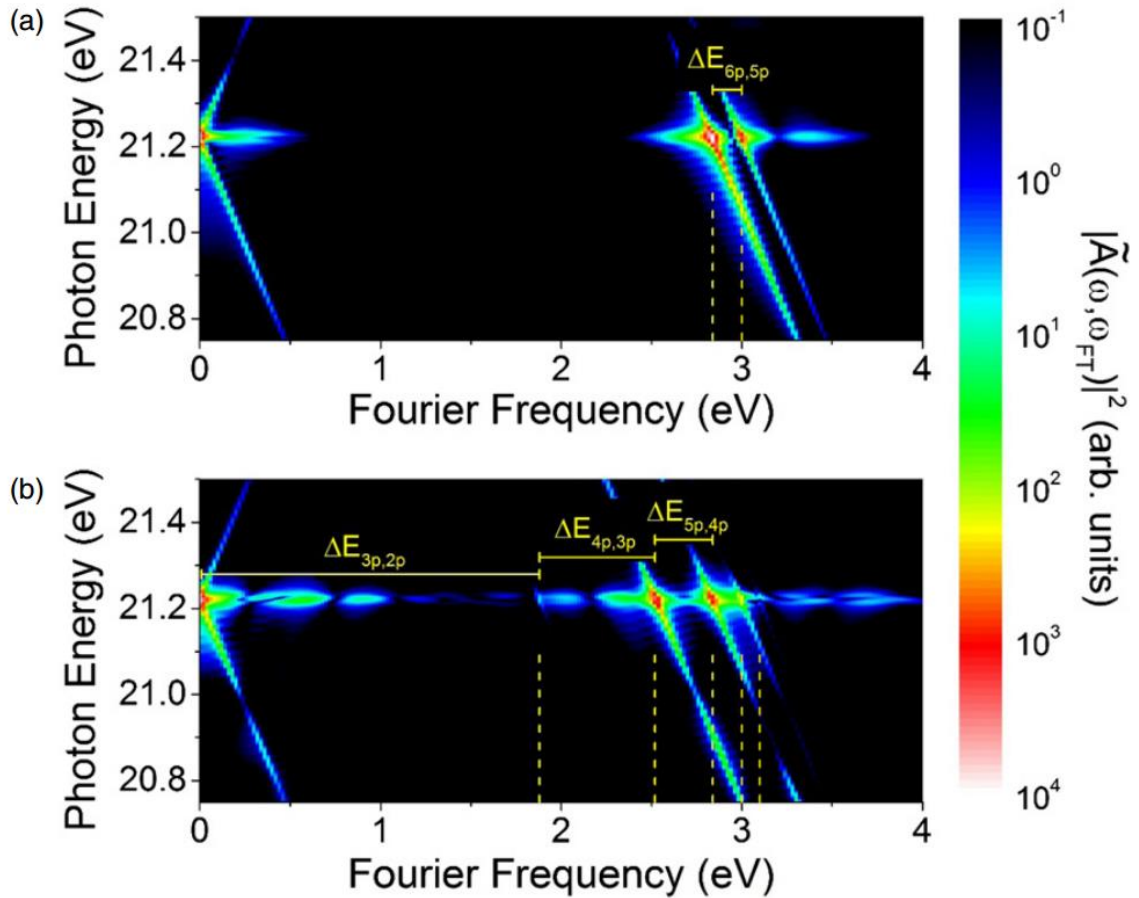


Figure 4-7 Fourier transform analysis of the quantum beats in the vicinity of the 1s2p excited state. (a) For the reduced basis set, the dominant quantum beat arises from the 1s5p and 1s6p states. (b) When the full 16-state basis set is used, additional beat frequencies corresponding to each of the 1snp energy level differences $\Delta E_{n'p,np} = E_{n'p} - E_{np}$ can be observed. Adapted from [77].

Quantum beats occurs when two quantum paths that leads to the same final states have a phase difference, and this phase difference gives rise to periodic beating structures. Recently we proposed that quantum beats can be observed in attosecond transient absorption experiments in the bound states. For example, in helium atoms, electrons in the $1s^2$ ground state can be excited to $1s2p$, $5p$, $6p$ states, in addition, $5p$ and $6p$ states can be coupled to the $1s2p$ state by emitting two NIR photons. We calculated the attosecond transient absorption spectrum in the $1s2p$ state, and found that the absorbance shows a slow variation structure, with a period of around 26 fs, which corresponds to the energy difference of the $1s5p$ and $1s6p$ states. In our experiment, quantum beats can be observed in a series of krypton autoionizing states. This is the krypton autoionizing states absorption cross section in the range from 14 to 14.7 eV, which is slightly higher than the ionization threshold, and this allows these autoionizing states be coupled to bound excited states by one or more photons.

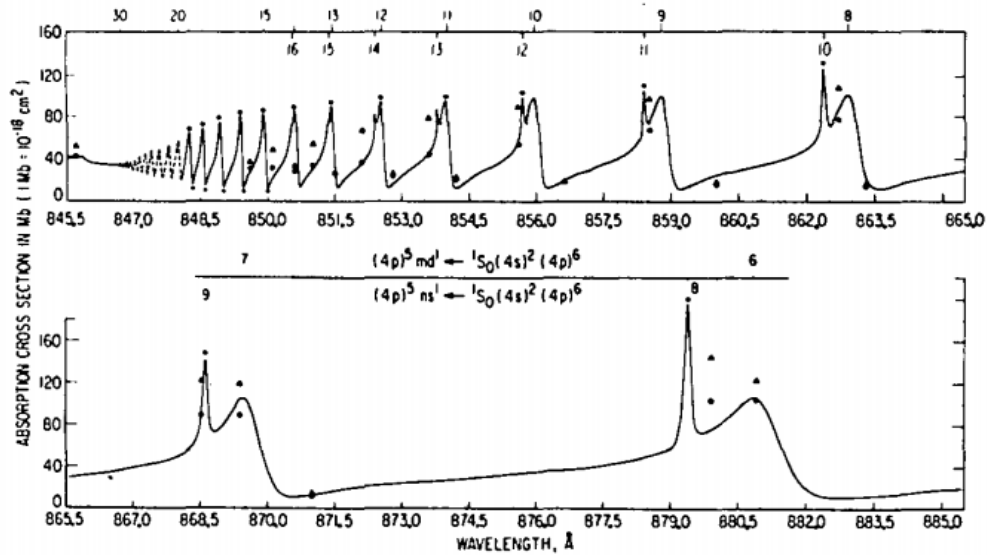


Figure 4-8 The atomic absorption cross section of krypton vs wavelength. Adapted from [78]

In the experiment, the output of a home-built femtosecond Ti:Sapphire laser was sent into a neon-filled hollow core fiber and a set of chirped mirrors. The pulse was split into a high-harmonic generation arm and a near infrared (NIR) arm by using a broadband beam splitter. In the high-harmonic generation arm, isolated attosecond pulses were generated using the double optical gating technique [27]. The vacuum ultraviolet (VUV) continuum was filtered using a 200 nm thick indium filter, and the spectra spans from below 12 eV to more than 17 eV.

In the attosecond transient absorption experiment, both the single attosecond pulse and the NIR laser pulse were focused into a 2 mm inner diameter krypton-filled gas cell, in which the absorption occurred. The time delay between the two pulses was varied by a piezoelectric transducer (PZT) stage. The transmitted VUV spectra was recorded as a function of the time delay in a VUV spectrometer composed of a flat-field grating and a MCP/phosphor detector.

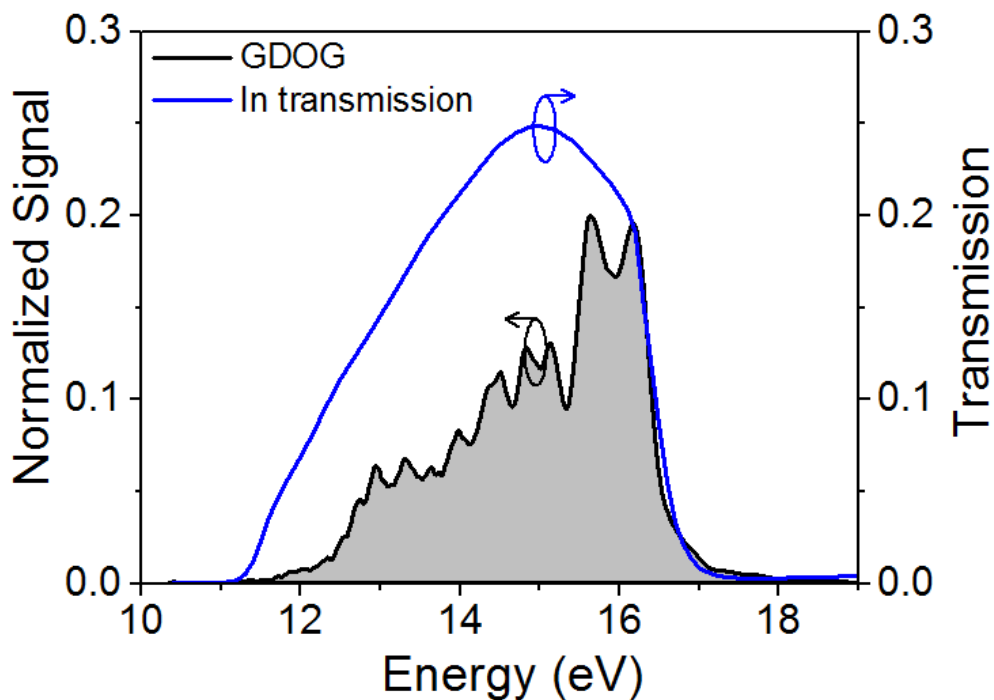


Figure 4-9 The attosecond pulse spectrum with a 200 nm thick indium filter.

The figure above shows the spectrum of the attosecond pulse generated using the generalized double optical gating technique, it covers from 11 eV to 18 eV, the blue curve is the transmission curve for a 200 nm thick indium foil filter. The krypton ionization energy is 14.0 eV, the XUV spectrum covers both excited bound states and the autoionizing states, and this is essential for this experiment in order to observe quantum beats in the autoionizing states.

The figure below shows the measured transmitted attosecond VUV spectra of krypton as a function of the time delay between the isolated attosecond pulse and a NIR pulse with a peak intensity of 5×10^{12} W/cm². Negative delay indicates that the isolated attosecond pulse arrives at the target before the NIR pulse. The attosecond pulse launches electronic wave packets composed of multiple bound excited states and spin-orbit coupling induced autoionization states of krypton atoms. Absorption lines corresponding to the $4s^2 4p^5 nd$ excited states change dramatically near zero time delay and in the negative delay region. In addition to the shifting and splitting of the energy levels in the negative delay region, quantum beats with a period of ~ 7 fs are observed in the $5d$ light-induced intermediate state [48].

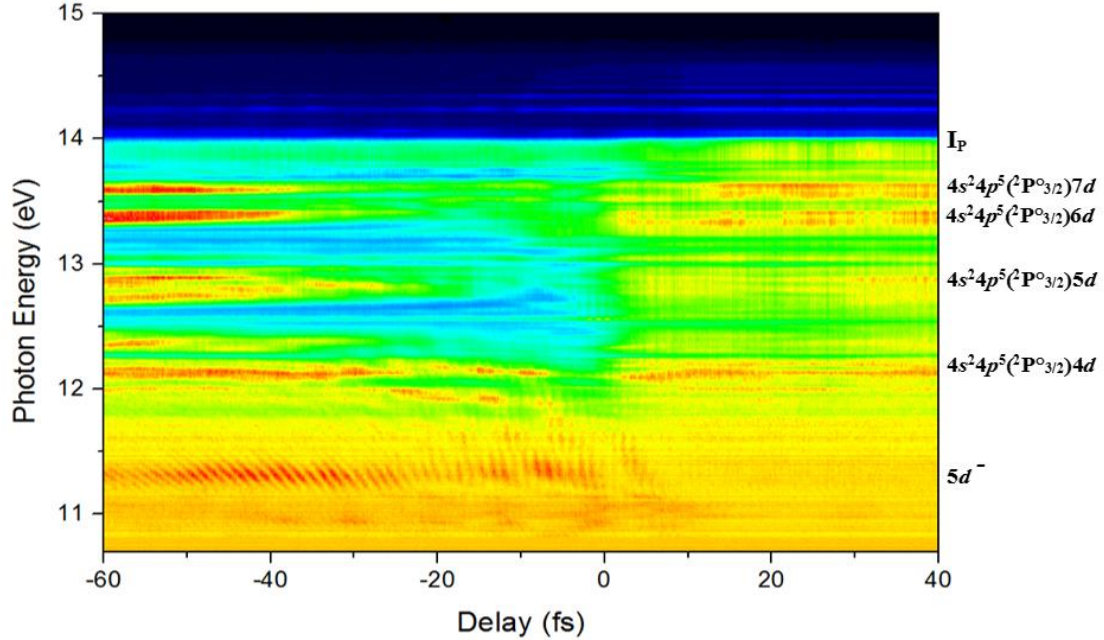


Figure 4-10 The measured transmitted attosecond VUV spectra of krypton as a function of the time delay between the isolated attosecond pulse and a NIR pulse with a peak intensity of $5 \times 10^{12} \text{ W/cm}^2$. Adapted from [79].

Here we replot this region in a different color scale so that we can see these features more clearly. This absorption lines correspond to 6d, 7d, 8d, and 9d autoionizing states. The oscillation period for these three states are 9.8 fs, 6.3 fs and 5.2 fs respectively. Furthermore, six autoionization lines are observed in the 14 – 15 eV region, as shown in the figure below. Recurrences are observed in the $4s^2 4p^5 (2P^o_{1/2}) 6d$, $4s^2 4p^5 (2P^o_{1/2}) 7d$, $4s^2 4p^5 (2P^o_{1/2}) 8d$ states with periods of 9.8 fs, 6.3 fs, 5.2 fs, respectively. Recurrences cannot be observed clearly in $4s^2 4p^5 (2P^o_{1/2}) 9d$, $4s^2 4p^5 (2P^o_{1/2}) 10d$, $4s^2 4p^5 (2P^o_{1/2}) 11d$ since the absorption features are not strong enough in the data. The quantum beats are attributed to electrons coupled by the dressing NIR laser pulse to the same final state after being initially excited by the attosecond pulse to different $4s^2 4p^5 (2P^o_{1/2}) nd$ autoionizing states. The beating itself arises from the field-free evolution of the wave packet in the time interval between the two pulses, with the wave packet motion imprinted as a slow variation in the absorption of the autoionizing states [5]. The relative phase among

these states can be retrieved from such measurement, thus allows the reconstruction of the valence state wave packet.

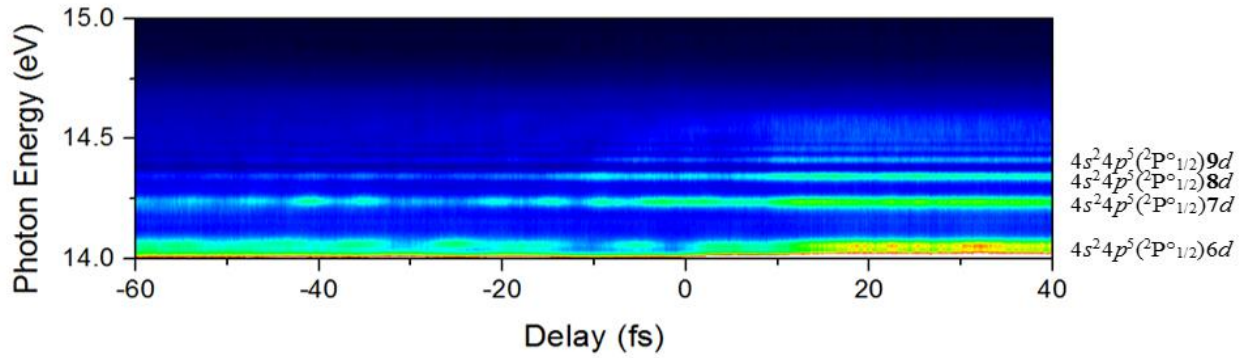


Figure 4-11 The measured transmitted attosecond VUV spectra of krypton as a function of the time delay between the isolated attosecond pulse and a NIR pulse in the energy range of 14 – 15 eV with a peak intensity of $5 \times 10^{12} \text{ W/cm}^2$. Adapted from [79].

This is the Fourier transform analysis of this region, this part clearly shows that these autoionizing states are coupled to bound excited states.

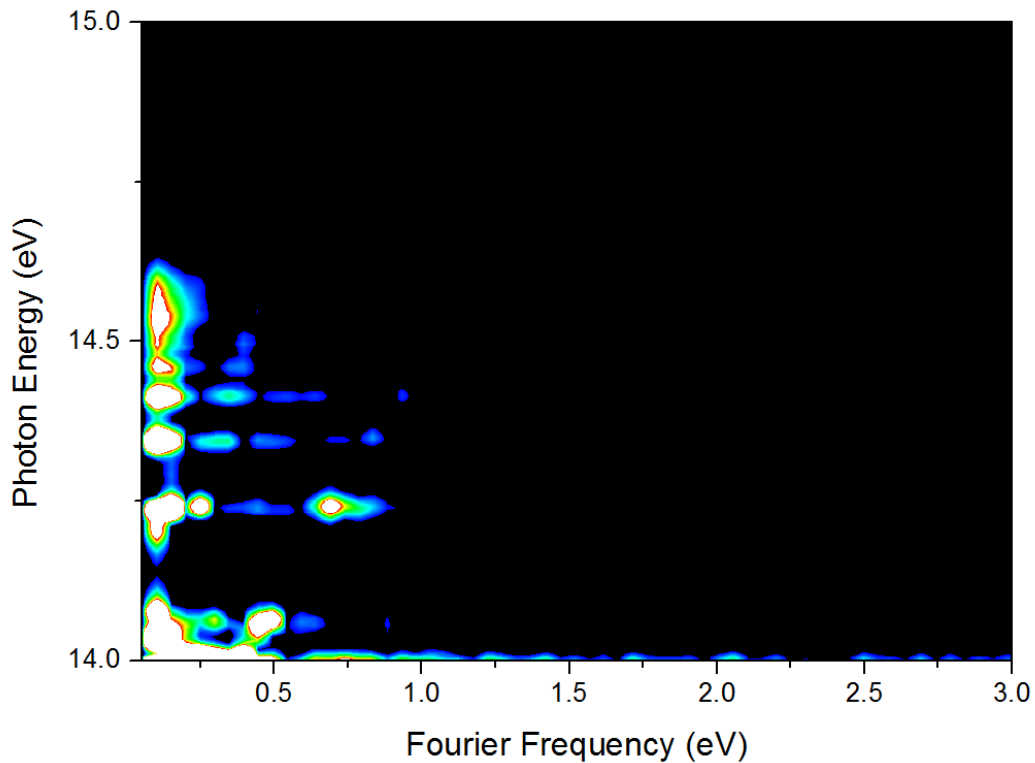


Figure 4-12 the Fourier transform analysis of the measured time dependent transmitted attosecond VUV spectra of krypton

So following this analysis, we proposed a simplified model calculation which includes the ground state, the 5p and 7d state and three autoionizing states. These four states can be coupled from the ground state by absorbing one xuv pulse, and these states can be coupled to the 5p state by one NIR photon. Because of these couplings, we expect to see quantum beating structures in these states.

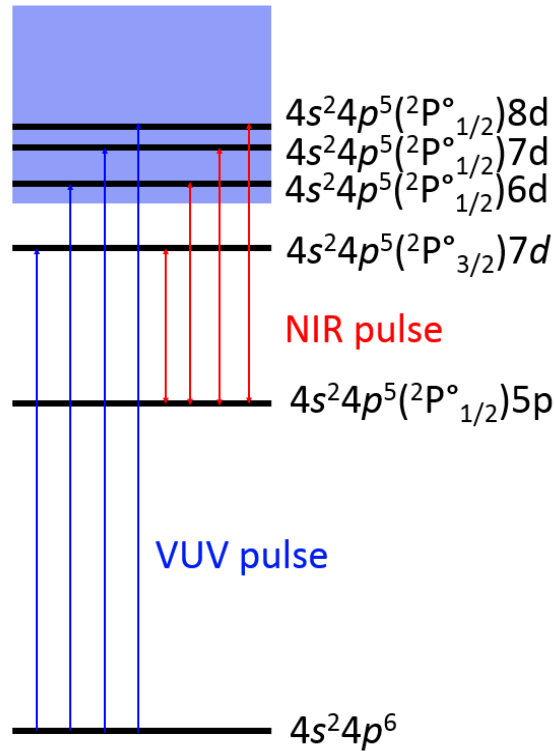


Figure 4-13 The simplified model calculation that includes the ground state, the 5p and 7d state and three autoionizing states.

And this is the calculation result, these autoionizing states shows clearly oscillation structures with periods of 10, 6, 5 fs, which is very close to the experimental results. In addition, these quantum beat measurements allows us to retrieve the quantum phase of these states thus allows the reconstruction of the valence electron wave packet, this part of work is still preliminary.

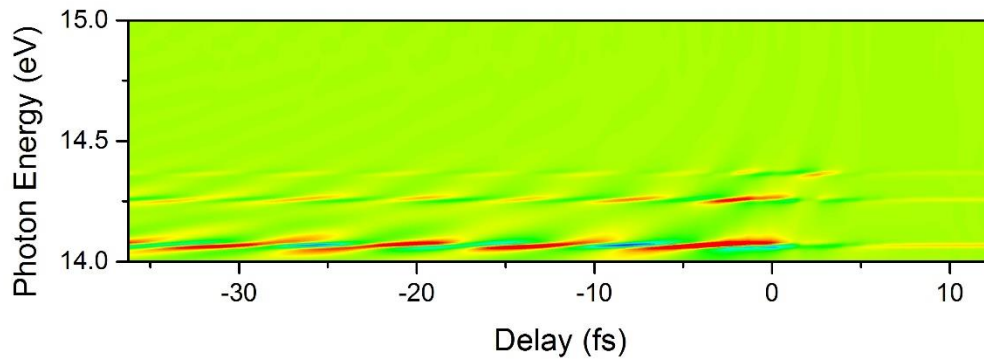


Figure 4-14 The calculated transmitted attosecond VUV spectra of krypton as a function of the time delay between the isolated attosecond pulse and a NIR pulse in the energy range of 14 – 15 eV

In conclusion, we measured the transient absorption of a single attosecond pulse in krypton bound states and autoionizing states by synchronizing a single attosecond pulse with a few-cycle NIR laser field. Other than the shifting and splitting of the bound state energy levels, quantum beats with periods of 9.8 fs, 6.3 fs and 5.2 fs are observed for the $4s^24p^5(^2P^{\circ}_{1/2})6d$, $4s^24p^5(^2P^{\circ}_{1/2})7d$, and $4s^24p^5(^2P^{\circ}_{1/2})8d$ autoionizing states respectively. Such measurement allows the reconstruction of the valence state wave packet.

CHAPTER 5 - COHERENT PHASE-MATCHED VUV GENERATION BY BELOW THRESHOLD HARMONIC GENERATION

Note: Portions of this chapter were used or adapted with permission from the following:

Michael Chini, Xiaowei Wang, Yan Cheng, He Wang, Yi Wu, Eric Cunningham, Peng-Cheng Li, John Heslar, Dmitry A. Telnov, Shih-I Chu & Zenghu Chang. Coherent phase-matched VUV generation by field-controlled bound states. *Nature Photonics* 8, 437–441 (2014)

Currently high order harmonics and attosecond pulses are usually generated with 10 Hz to 1 kHz repetition rate, high harmonics generated with megahertz repetition rates are very desirable for experiments such as coincidence measurements and photoemission spectroscopy. The generation of high-order harmonics [80] and attosecond pulses [81] at megahertz (MHz) repetition rates allows for the extension of frequency metrology techniques [82] to the vacuum ultraviolet (VUV) and soft x-ray spectral regions and to attosecond timescales. Ideally, such processes could be driven directly by plasmon field enhancement of laser pulses from a femtosecond oscillator [83, 84], but recently people found that the below-threshold harmonics generation is actually governed by incoherent atomic line emission [85] due to poor phase matching. Here, we demonstrate below-threshold harmonics generation in a new regime, in which the phase matching of short trajectory harmonics is enabled only near resonant structures of the atomic target. The generated coherent VUV line emission exhibits narrow spectral linewidths with low divergence and phase-matched growth with increasing target density, and requires intensities on the order of 10^{13} W/cm², which can be achieved through tight focusing of few-cycle femtosecond pulses with sub-microJoule energy.

5.1 Below Threshold Harmonic Generation

Recent work in high-order harmonics generation (HHG) at high repetition rates [80, 83] has focused on the so-called below-threshold harmonics, with photon energies below the target ionization potential. Such harmonics are critical to the extension of attosecond science to MHz repetition rates and to the development of HHG sources with high average power, since they can be generated with relatively low driving laser intensities ($\sim 10^{13}$ W/cm²). However, little is known about the mechanism behind the generation of below-threshold harmonics. Although non-perturbative below-threshold harmonics generation is incompatible with the semiclassical three-step model of HHG [8], recent experimental work [80, 86-88] indicates that below-threshold harmonics can arise from a recollision process, and theoretical models extending the three-step model to account for negative-energy electron recollisions have been proposed [88, 89].

Such semi-classical treatments of the HHG process minimize the effects of the target atom structure on the high-order harmonic spectrum. However, this approach which may not be valid for the generation of below-threshold harmonics, where resonance-enhancement of high-order harmonics has been observed for moderate driving laser intensities [90-92]. Here, we uncover a novel regime of below threshold harmonics generation accompanied with coherent VUV line emission. The line emission is generated from moderately intense few-cycle driving laser pulses, wherein the VUV generation is enhanced in the vicinity of dipole-allowed single-photon transitions. In contrast to the incoherent atomic line emission observed in HHG with high laser intensities [93] or with plasmonic enhancement [85], the narrow-linewidth VUV emission is spatially coherent and exhibits phase-matched growth. Our results, supported by numerical simulations under identical experimental conditions, suggest that the atomic resonances enhance not only the single-atom emission, but also the coherent build-up of fully phase-matched below-threshold harmonics.

In the experiment, below-threshold high-order harmonics were generated from argon gas in a loose focusing geometry, and the VUV spectrum was measured using a flat-field grating spectrometer [29]. The high harmonic generation was driven with few-cycle ($\tau = 5$ fs, $\lambda = 730$ nm) near infrared (NIR) laser pulses with moderate intensities ($\sim 10^{13} - 10^{14}$ W/cm²) sufficient to generate high-order harmonics, but not so high as to destroy the atomic resonances. In the language of strong-field laser physics, such intensities correspond to the border between the “multi-photon” and “tunneling” regimes of ionization [9, 94]. The use of few-cycle driving lasers relaxes the constraints on resonance-enhanced HHG in the traditional sense, and multiple resonances can be observed in the spectrally-resolved HHG signal.

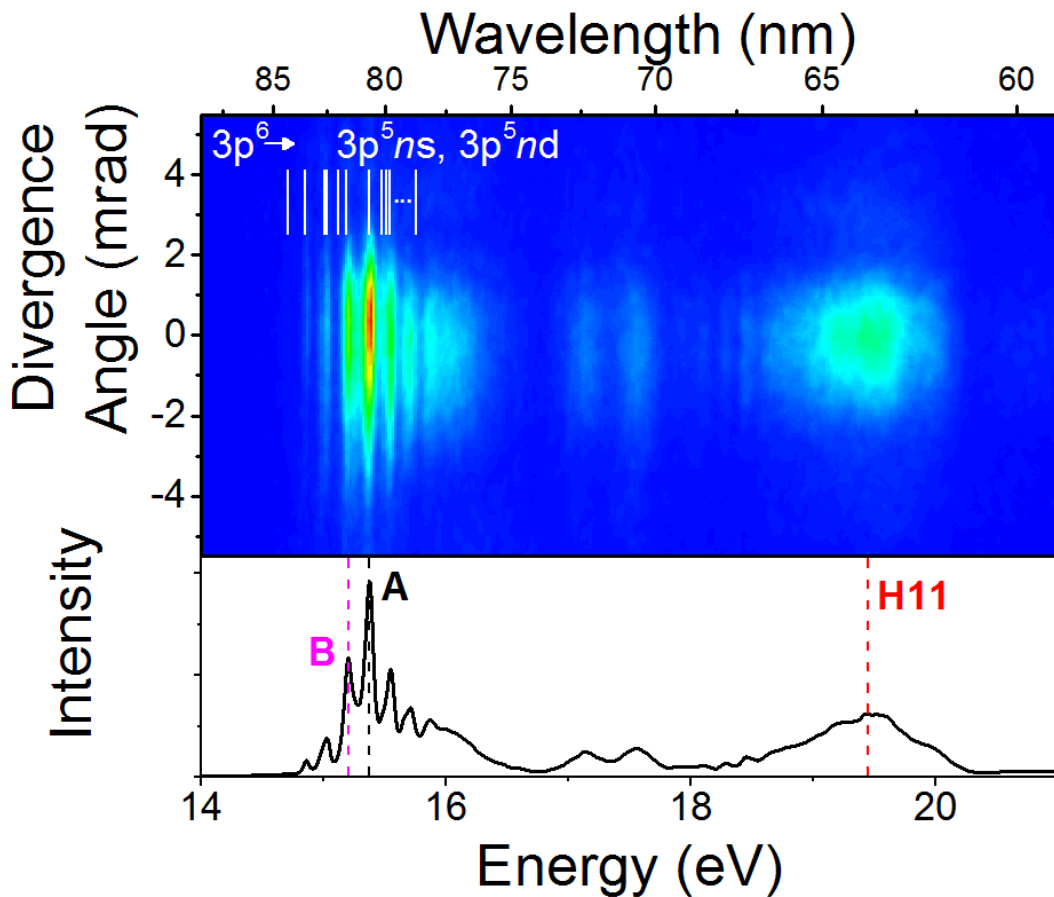


Figure 5-1 Measured harmonic spectrum with an intensity of $(3.3 \pm 0.3) \times 10^{13}$ W/cm² and a target pressure-length product of 10 torr-mm. The spectrum is characterized by coherent

line emissions (e.g.; RESs A and B) consistent with the labelled $3p^6 \rightarrow 3p^5ns$ and $3p^5nd$ resonances of argon (indicated by vertical white lines) in addition to the broadband high harmonics (e.g.; the 11th harmonic, H11). Adapted from [95].

The figure above shows the spectrally- and spatially-resolved HHG signal in the vicinity of the 9th and 11th harmonics with a driving laser intensity of $(3.3 \pm 0.3) \times 10^{13}$ W/cm² and a target pressure-length product of 10 torr-mm. Whereas the 11th harmonic is above the argon ionization threshold ($I_p = 15.76$ eV), the 9th harmonic spans photon energies both above- and below-threshold. Below-threshold, the 9th harmonic exhibits narrow-linewidth spectral enhancements in the vicinity of the atomic resonances. The figure below shows the evolution of these resonance-enhanced structures as a function of the driving laser intensity within three different regimes. At relatively low intensities ($\sim 1 - 3 \times 10^{13}$ W/cm²), the resonance-enhanced structures exhibit narrow linewidth and dominate the high harmonic spectrum. For intensities between $\sim 5 - 8 \times 10^{13}$ W/cm², The above-threshold harmonic emission becomes comparable to the resonance-enhanced structures, and the linewidths in general become shifted and broadened until no resonances can be observed at intensities higher than $\sim 10^{14}$ W/cm². The intermediate regime corresponds almost exactly with the crossover from the multi-photon to the tunneling ionization regime. Although the electronic states corresponding to the various resonance-enhanced structures could not be determined precisely, the mechanism of resonance enhancement is confirmed by below-threshold harmonics generation in neon and xenon gases, and by numerical solution of the time-dependent Schrodinger equation.

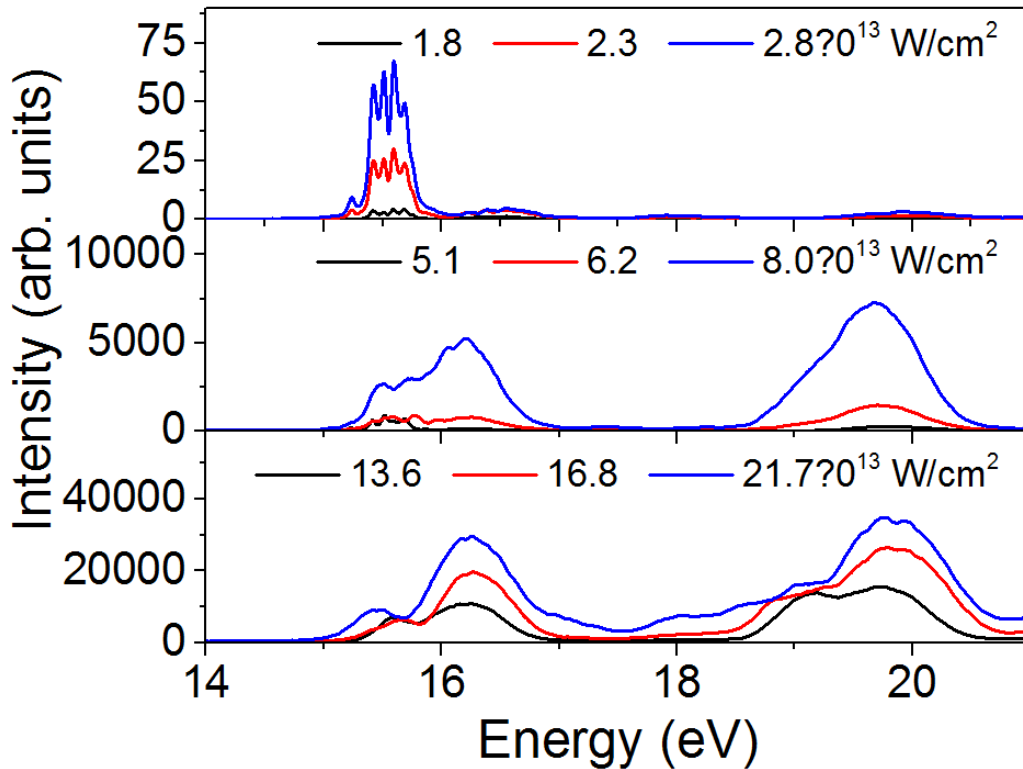


Figure 5-2 Evolution of the resonance-enhanced structures with driving laser intensity. At low intensities (top), the resonance-enhanced structures dominate the spectrum, whereas the harmonics dominate at higher intensities (bottom). Adapted from [95].

The figure below shows the below threshold harmonic generation for xenon, argon and neon gas. The ionization threshold for xenon, argon and neon is 12.12 eV, 15.76 eV and 21.56 eV respectively. We can see that the xenon spectrum consists of only relatively broad harmonic orders, whereas the argon and neon spectra exhibit coherent line emission in the vicinity of their respective bound excited states, up to the ionization thresholds. By comparing the harmonic spectra of argon with those from neon and xenon, we confirm that the coherent resonance-enhanced structures (RESs) coincide in photon energy with the atomic resonance manifolds of these gases.

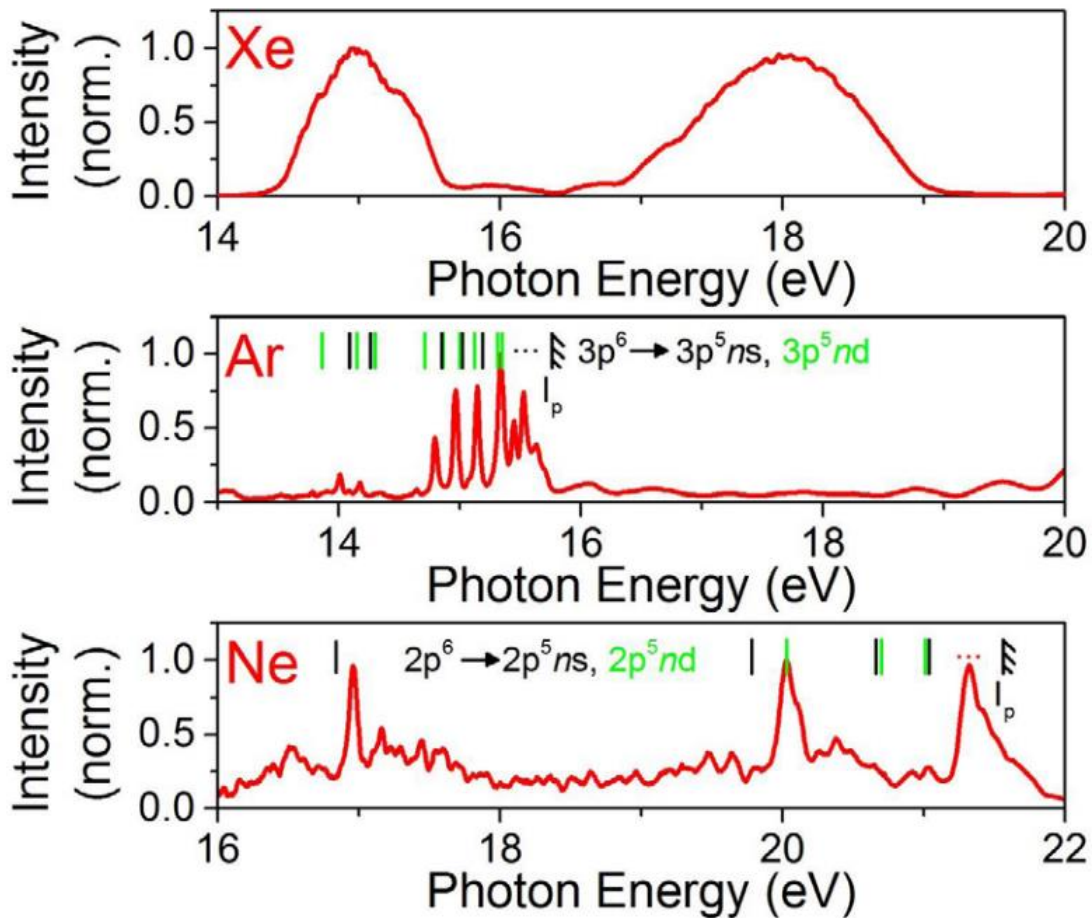


Figure 5-3 Argon and neon exhibit resonance-enhanced structures in the below-threshold harmonics generation, whereas the harmonics generated in xenon are structureless above the ionization threshold. Bound state resonances within the photon energy ranges of interest are indicated. Adapted from [95].

5.2 Coherent VUV Emission

Although spectrally similar to atomic line emission, the observed resonance-enhanced structures are emitted in a laser-like beam, with divergence angles similar to the above threshold harmonics as shown in the figure below. Such a small divergence angle is consistent with previous measurements of below-threshold harmonics in a tight focusing geometry [80, 87],

wherein multiple divergence angles were attributed to quantum trajectories with different intensity-dependent phases. Here, the phase matching conditions are chosen to favor the short trajectories with small intensity-dependent phase, and the more strongly divergent long trajectory contributions are not observed. Although previous studies have indicated that such short trajectory contributions cannot be initiated by tunnel ionization [89], we can confirm that the resonance-enhanced harmonics generation does result from a recollision-like process. In the figure below, the integrated yield of the resonance-enhanced structures between 15 and 15.8 eV is compared to that of the above-threshold 11th harmonic for an elliptically polarized driving laser pulse with the same intensity. The strong ellipticity dependence of both the resonance-enhanced structures and the above-threshold harmonics is indicative of a recollision-based generation process, wherein the ionized electron can be driven away from the parent ion by the elliptically polarized field and preventing recombination [31]. We find that the efficiency of both the resonance-enhanced structures and the above-threshold harmonic generation drop by one order of magnitude when the ellipticity is ~ 0.2 , in good agreement with previous measurements using more intense few-cycle laser pulses [96]. It is worth noting that, although the recollision-based three-step model is typically applied in the tunneling ionization regime, similar quantum trajectory analyses can be applied at lower laser intensities [80, 89].

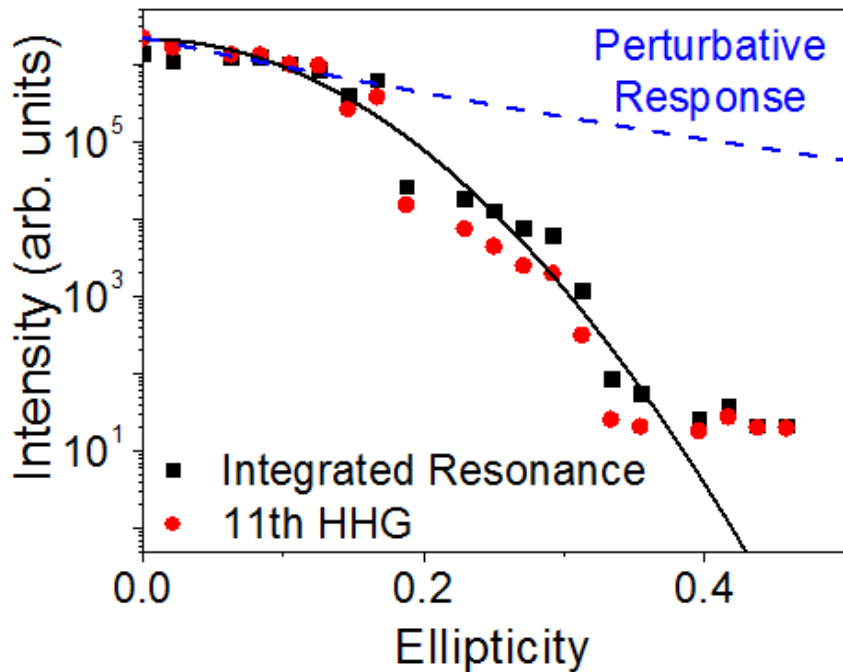
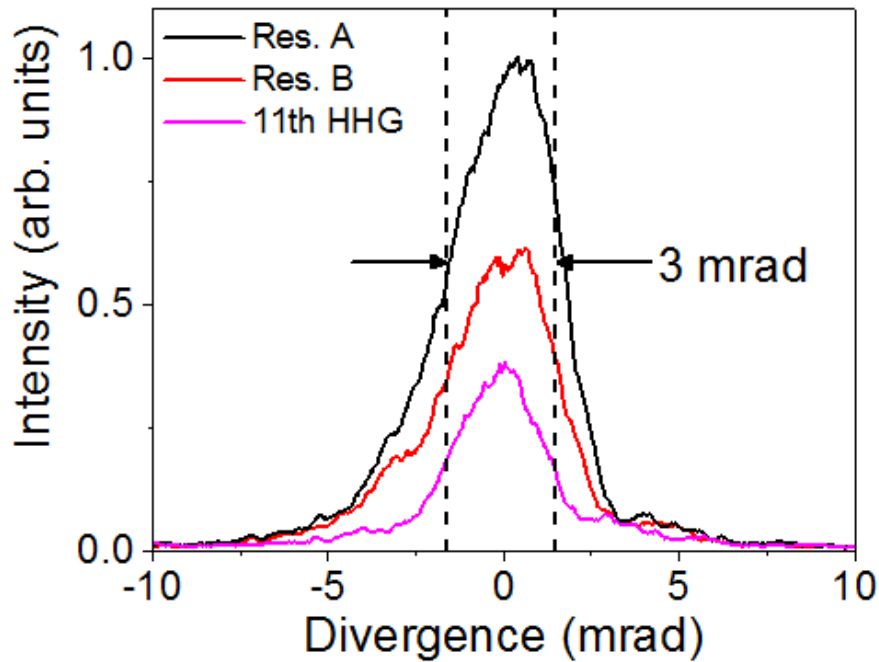


Figure 5-4 a, Both the RESs (here, A and B) and the above-threshold harmonics exhibit narrow divergence angles of ~ 3 mrad FWHM, indicating laser-like spatial coherence of the VUV line emission. b, The efficiency of the coherent line emission depends strongly on the ellipticity of the driving laser, and indicates a sub-cycle generation mechanism. The ellipticity dependence is much stronger than that expected from recollision (blue solid line), but is consistent with harmonic generation during tunneling. Adapted from [95].

Using the double optical gating technique, we measure the dependence of VUV generation as a function of the carrier envelope phase of the driving NIR laser pulses. The double optical gating technique creates a half laser cycle gate (~ 1.5 fs) with linear polarization. The intensity within the gate is $\sim 5 \times 10^{13}$ W/cm².

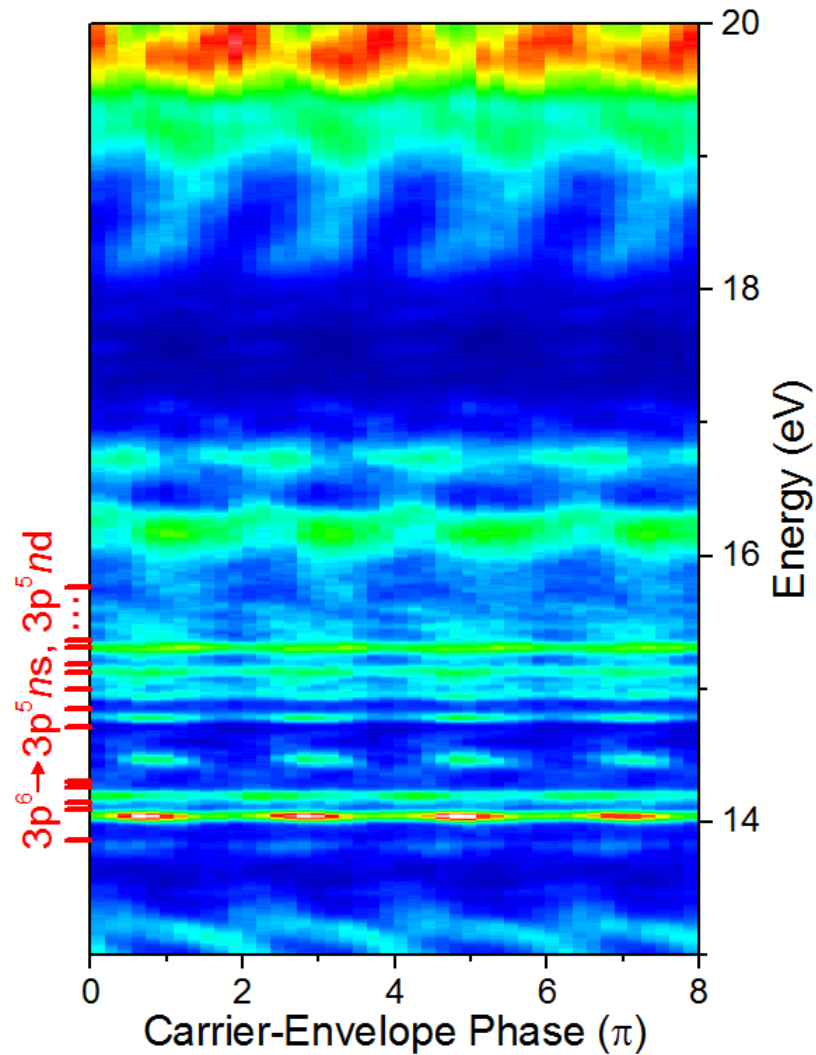


Figure 5-5 The RESs exhibit a strong dependence on the carrier-envelope phase when the VUV generation is confined to a single half-cycle of the driving laser. Adapted from [95].

When the driving laser pulse is ~ 5 fs with linear polarization, the carrier envelope phase dependence is much weaker, as shown in the figure below.

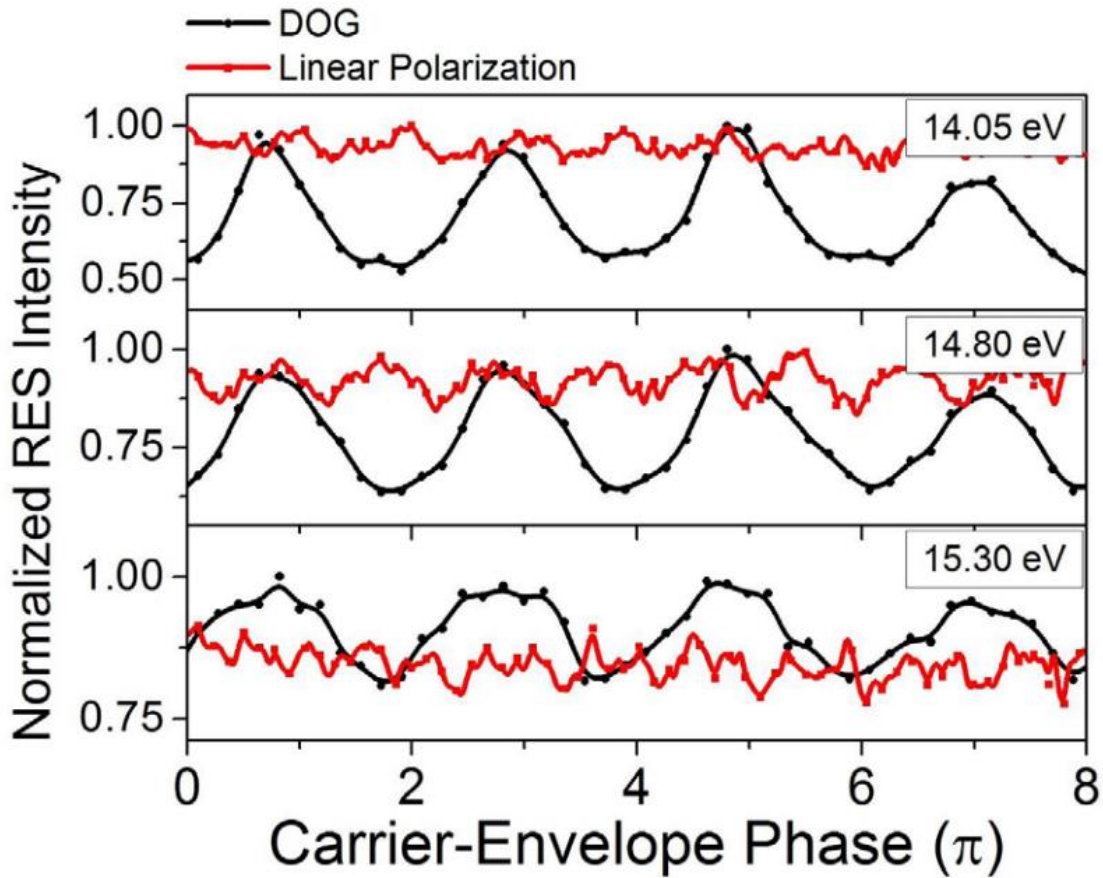


Figure 5-6 The intensity of the RESs located at 14.05 eV (top), 14.80 eV (middle) and 15.30 eV (bottom) exhibits a 2π periodicity under the DOG, whereas much smaller changes are observed with the CEP for linearly polarized 5 fs pulses. Adapted from [95].

5.3 Phase Matching Mechanisms

Generation of strong sources of high-order harmonics requires that extra attention is paid to the phase matching of the generation process [97, 98], allowing coherent build-up of the harmonic photons generated by different atoms in a macroscopic medium. However, near- and

below-threshold harmonics can typically not be well phase-matched. Above-threshold, this results from the strong absorption of the neutral gas, which limits the phase-matched build-up to relatively low pressures [99]. On the other hand, phase matching of the below-threshold harmonics, though not well understood, is typically thought to be limited to quantum trajectories with large intensity-dependent phase. In the figure below, the phase matching of the resonance-enhanced structures at between 15 and 15.8 eV is compared with that of the 11th harmonic. The quadratic growth of the high-order harmonic signal as a function of gas pressure characterizes perfect phase matching, and the harmonic yield is limited by absorption. We observe that, while the phase matching of the 11th harmonic is limited by re-absorption of the harmonic photons to pressure-length products of ~ 20 torr-mm, the resonance-enhanced structures below-threshold can be perfectly phase matched to much higher pressures – up to nearly 1000 torr-mm, allowing a relative enhancement of the resonance-enhanced structures over the above-threshold harmonics by approximately four orders of magnitude. The figure below compares harmonic spectra calculated from solution of the time-dependent Schrodinger equation for a single atom and for a macroscopic medium as used in the experiment. By comparing the two spectra, we can see that the below-threshold phase matching is indeed enhanced near the atomic resonance structures, while the off-resonance below-threshold harmonics are comparatively weaker after propagation through the macroscopic medium.

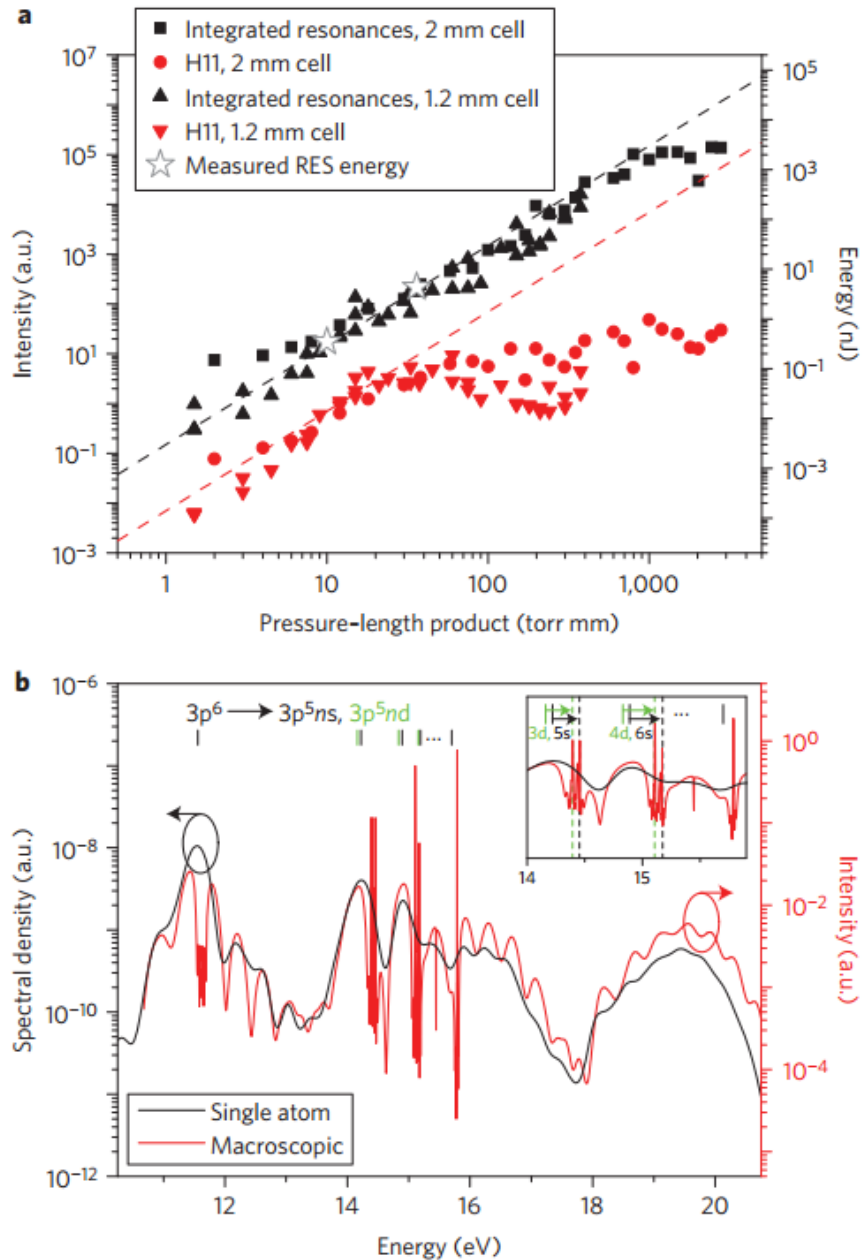


Figure 5-7 a, The coherent VUV emission in the vicinity of the RESs scales quadratically with the target gas pressure-length product, indicating perfect phase-matching. The 11th harmonic (H11) scales quadratically up to a pressure-length product of only ~20 torr-mm, due to the strong absorption cross-section of the neutral gas for photon energies just above the ionization threshold. Calibrated energy measurements of the RESs are indicated by open gray stars. **b**, Numerical simulation of the VUV emission in argon indicates that the phase-matching process results in spectrally narrow, energy-shifted RESs when compared with the single-atom emission. The shift of the phase-matched RESs relative to the bound state energies is indicated in the inset. Adapted from [95].

The on-axis phase matching of the resonance-enhanced structures can be understood by considering the propagation of both the NIR driving laser and the generated VUV light through the medium. Perfect phase matching requires that the phase accumulated in the wave propagation is the same for both the NIR and VUV. For a Gaussian beam, the phase mismatch of the q^{th} harmonic is given by:

$$\Delta\varphi = \frac{\alpha I_0}{1 + (z/z_R)^2} + q \arctan(z/z_R) + \Delta k_q z \quad (5-1)$$

where the three terms describe the intensity-dependent dipole phase, the Gouy phase, and the chromatic dispersion of the ionizing medium [10]. The proportional coefficient α is different for long and short quantum trajectories, and z_R is the Rayleigh length of the focused beam. Phase matching is optimal when $\Delta\varphi$ does not vary much with the propagation coordinate z . In the absence of strong ionization, Δk_q is often assumed to be approximately equal to zero for harmonics with photon energies above the ionization threshold, and short trajectory phase matching is achieved for a thin target located with the range of $0 \leq z \leq z_R$. However, for below-threshold harmonics from quantum trajectories initiated by multi-photon ionization, α is approximately zero [80, 89, 100], and the phase mismatch of the Gouy phase cannot be compensated by that of the dipole phase. On the other hand, the neutral atom phase mismatch becomes nonzero when the harmonic photon energy lies near an atomic resonance. For the below-threshold harmonics (again, in the absence of substantial ionization), the neutral atom

phase mismatch may dominate for certain photon energies, the neutral atomic medium phase mismatch can be written as:

$$\Delta k_{at}(\omega) \approx \frac{2\pi N\omega}{c} \sum_j \frac{f_j}{\omega_j^2 - \omega^2} \quad (5-2)$$

and the Gouy phase is:

$$\Delta k_G(z) \approx q \frac{1}{2\pi} \frac{d}{dz} \tan^{-1} \left(\frac{z}{z_R} \right) \quad (5-2)$$

where z is the on-axis target position relative to the focal point, z_R is the Rayleigh length, q is the harmonic order, N is the atomic density, and ω_j and f_j are the energy and oscillator strength of the j^{th} resonance.

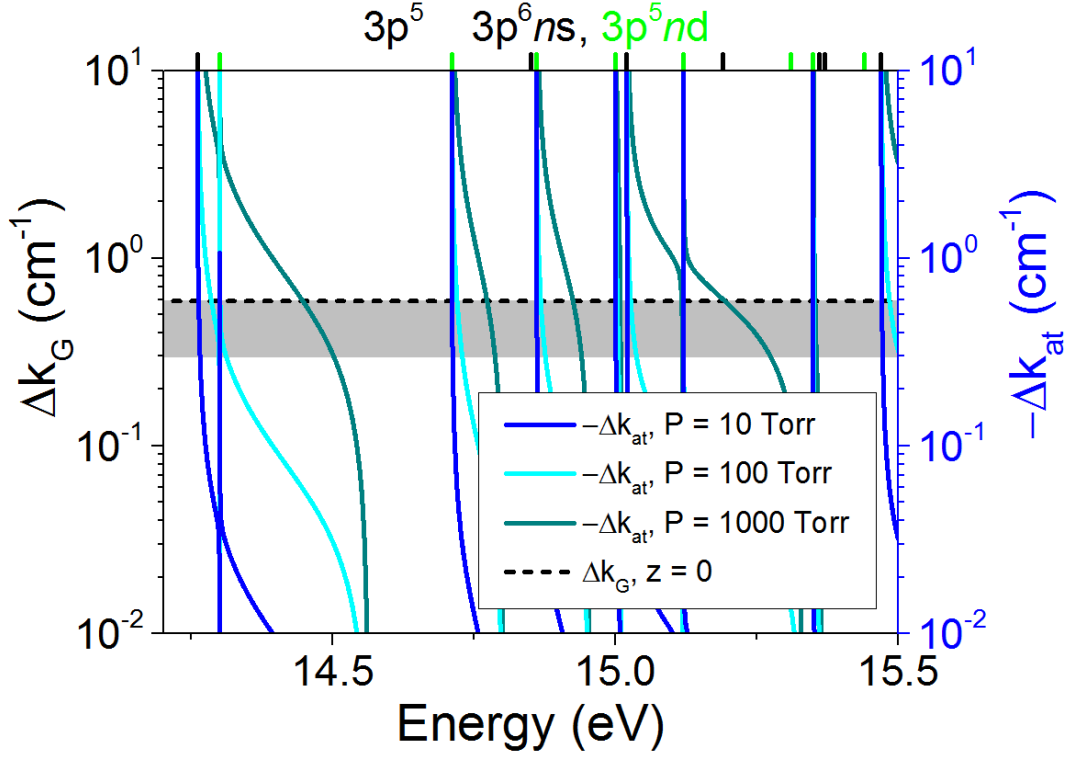


Figure 5-8 Argon exhibits regions of anomalous dispersion (gray shading) in the vicinity of the atomic resonances, just above the resonance energies. Adapted from [95].

In the figure above, we plot the contributions of the Gouy phase shift and the near-resonance neutral atom dispersion to the total phase mismatch for an isolated resonance in the vicinity of the 9th harmonic under similar conditions to the experiments. Clearly, phase matching can be achieved only within a narrow spectral range near resonance. From the total phase mismatch, we find that the resonance-enhanced phase matching condition can be met for $0 \leq z \leq z_R$. In addition, the phase matching conditions depend on the pressure (density) of the atomic gas and on how close the photon energy is to the resonance energy. For photon energies $\omega > \omega_j$, the resonance contribution to Δk_{at} is negative and can compensate the positive Gouy phase-mismatch, giving $\Delta k = \Delta k_{at} + \Delta k_G \approx 0$ under the experimental conditions.

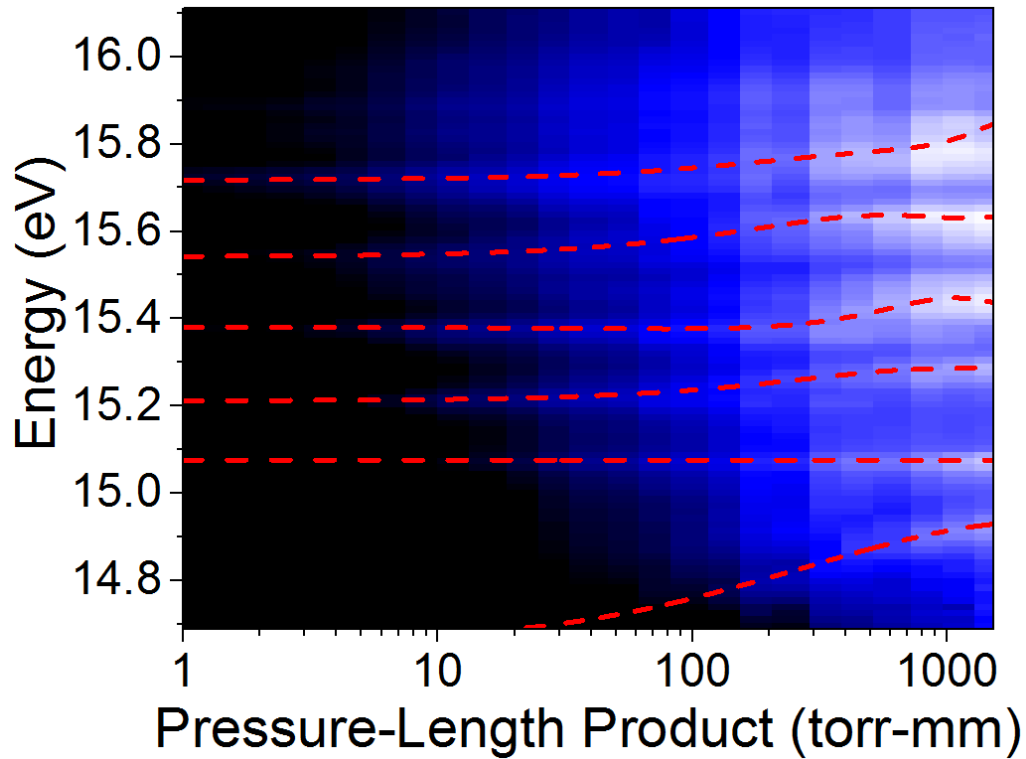


Figure 5-9 Since the amount of negative dispersion increases with the pressure, the phase-matched photon energy moves away from the resonance energy, and the RESs tend to shift to higher energy with increasing pressure. The dashed red lines represent a cubic spline fit of the most prominent RES peak energies. Adapted from [95].

As shown in the figure above, the resonance-enhanced structures are observed to shift in energy when the pressure is increased, indicating that the phase matching process can select the particular photon energy within the harmonic for perfect phase matching.

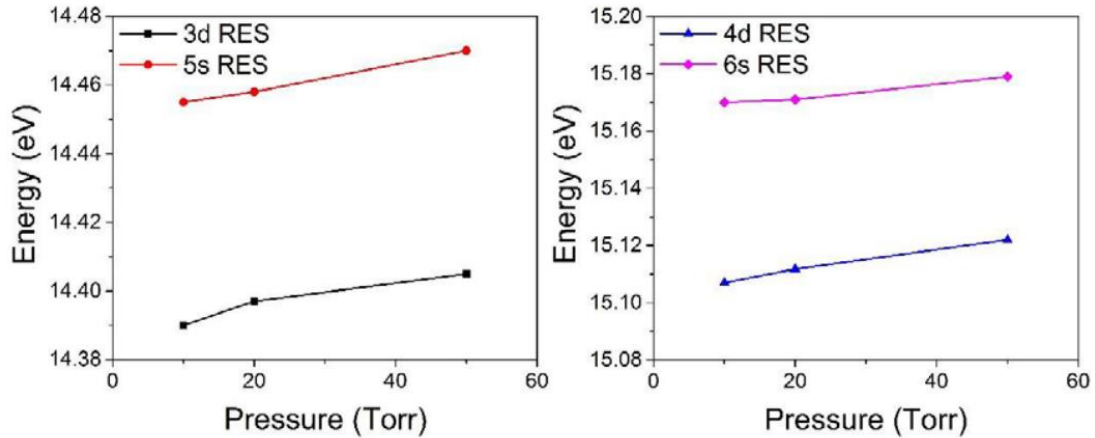


Figure 5-10 As the target pressure increases, the phase-matching occurs at higher energies and the RESs are observed to shift in energy. Adapted from [95].

High-order harmonics generated at high repetition rates have already been demonstrated as a novel source for direct frequency comb spectroscopy [101] and may soon replace 3rd generation synchrotron sources of high average power VUV light for lensless imaging [102], photoelectron spectroscopy [103, 104] and nanoscale lithography. Here, we demonstrate a novel regime of phase-matched below-threshold harmonics generation which is initiated by multi-photon ionization and requires driving laser intensities on the order of 10^{13} W/cm². Such intensities are already achievable from few-cycle laser oscillators at the nanoJoule level [105], which may enable phase-matched harmonic generation with MHz repetition rates without the need for cavity or nanoplasmonic enhancement.

CHAPTER 6 - ATTOSECOND TRANSIENT ABSORPTION SPECTROSCOPY IN HYDROGEN MOLECULES

Attosecond pulses promise to allow new forms of quantum control in which a broadband isolated attosecond pulse excites a molecular wavepacket consisting of a coherent superposition of multiple excited electronic states. This electronic excitation will trigger nuclear motion on the molecular manifold of potential energy surfaces and can result in permanent rearrangement of the constituent atoms. The ability to steer reaction outcomes by controlling the exciting light fields will enable attosecond control in photo-induced chemical processes [106, 107]. Here, we demonstrate attosecond transient absorption spectroscopy as a viable probe of the electronic and nuclear dynamics initiated in neutral hydrogen molecules by an isolated attosecond vacuum ultraviolet (VUV) pulse. The technique allows high-resolution and state-resolved measurements of molecular dynamics without the need for inducing subsequent ionization [108] or dissociation[109].

Purely electronic processes in atoms and small molecules typically proceed on attosecond to few-femtosecond timescales, as dictated by the energy level spacings between the ground and low excited states. In the absence of external degrees of freedom, electronic wavepackets excited by an isolated attosecond pulse[48, 56, 110] or by strong field ionization [34] exhibit a high degree of coherence, and can be probed via the photoelectron or transient absorption spectrum. On the other hand, electronic excitation in molecules leads to subsequent rearrangement – vibration, rotation, torsion – of the nuclei, on the timescale of femtoseconds to picoseconds, which can ultimately lead to the breaking of chemical bonds. Recent advances in the generation of attosecond light pulses [111] and time-resolved spectroscopic techniques have opened the

possibility of attosecond photochemistry [106, 107], wherein the initial electronic excitation can steer a chemical reaction along a particular trajectory.

Bound states are major actors in the quantum dynamics of systems with chemical and biological interest. Pioneering experiments have demonstrated attosecond control of ionization [108] and dissociation [109] of hydrogen molecules by detecting the charged reaction products. However, these techniques only provide indirect information on such dynamics as they require to pass through an ionization or dissociation step, and detection of only the final product of the interaction obscures the molecular dynamics. Furthermore, application of coincidence techniques to large systems, such as chromophores in proteins, will give electron spectra that are too complicated to be understood. On the other hand, attosecond transient absorption spectroscopy (ATAS), which is sensitive to the dynamics in individual bound states without the need for subsequent ionization or dissociation, does not require to disentangle the impossibly complicated path of strongly interacting electrons through bigger molecules. One can conceivably be able to monitor the recurrence of the vibronic wave packet created close to a localized chromophore, even in solution. So far, ATAS has been applied successfully to the study of wave packet motion [34, 48, 63, 110] and correlated electron dynamics [5, 112] in atoms and condensed matter [113] with unprecedented high energy resolution and time resolution. With recent developments in both experimental and theoretical approaches to ATAS, however, it is becoming apparent that the range of applicability of the technique is much larger than that.

6.1 Excited Vibrational States of Molecular Hydrogen

In this work, we make a major step forward and report for the first time the application of ATAS to H₂ molecules in the VUV energy range with sufficient energy resolution to monitor

several vibrational levels and to detect clear evidence of ultrafast recurrences associated with the vibronic wave packet in the system. The experiments are accompanied by state-of-the-art *ab initio* quantum calculations which fully account for both the electronic and nuclear motion in the presence of the two pulsed fields, and which guide the interpretation of the rich dynamics through the development of a few-level models which include the minimum number of electronic states in order to reproduce the most relevant features observed in the experimental and the fully *ab initio* results. These results paint a complete picture of the neutral hydrogen molecule in which attosecond electron excitation triggers nuclear motion evolving on the manifold of potential energy surfaces. The measurements further suggest ATAS as a viable technique for extending attosecond science to larger molecules, where coupled electronic and nuclear dynamics in the bound and quasi-bound state manifold underpin photochemical processes relevant to solar energy and photocatalysis.

The bound state manifold of molecular hydrogen is plotted in Figure 6-1 a. Absorption lines corresponding to the B $^1\Sigma_u^+ \leftarrow X^1\Sigma_g^+$, C $^1\Pi_u \leftarrow X$, and D $^1\Pi_u \leftarrow X$ bands of neutral hydrogen molecules are imprinted on the attosecond spectrum, as shown in Figure 6-1 b and c.

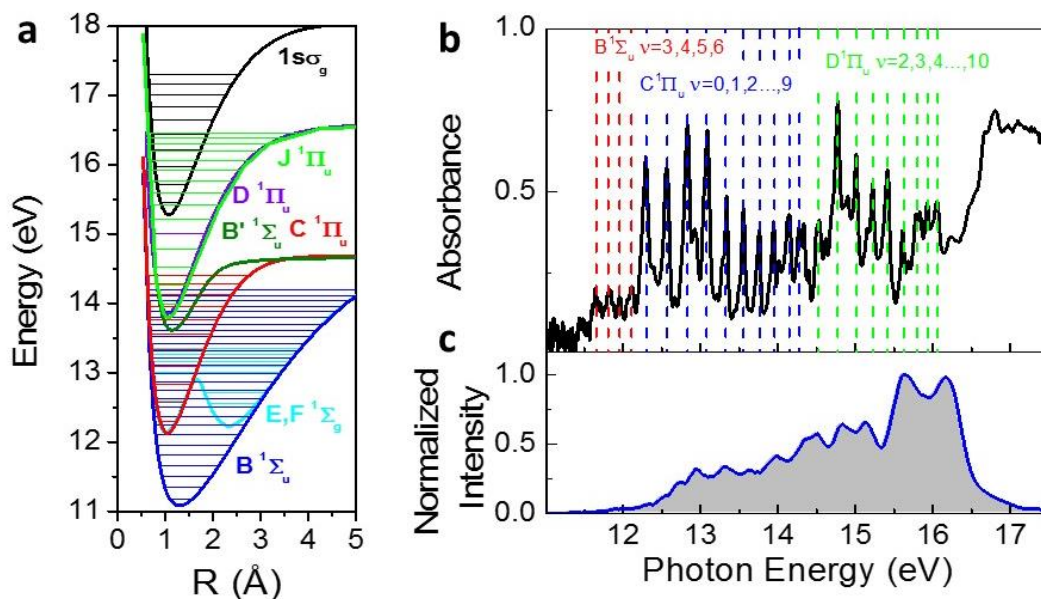


Figure 6-1 Attosecond absorption in neutral hydrogen molecules. a, the bound state manifold. The electronic and nuclear dynamics are encoded in the transient changes of the absorption lines with state selectivity. b, Absorption lines corresponding to the $B'^1\Sigma_u^+ \leftarrow X'^1\Sigma_g^+$, $C'^1\Pi_u \leftarrow X'$, and $D'^1\Pi_u \leftarrow X'$ bands of neutral hydrogen molecules can be observed in the attosecond spectrum. c, The spectral range of the attosecond VUV pulse was selected by using an indium foil filter .

6.2 Simultaneous Observation of Electron and Nuclear Dynamics in Hydrogen Molecules

In the experiments, few-cycle (~ 5 fs) pulses with a central wavelength of 730 nm from a Ti:Sapphire amplifier with a hollow-core fiber and chirped mirror pulse compressor were focused using a spherical mirror ($f = 500$ mm) into a quasi-static gas cell (inner diameter = 1.2 mm) with laser drilled holes placed ~ 5 mm after the laser focus. Isolated VUV pulses with spectrum supporting a transform-limited pulse duration of 750 as, which were generated using the generalized double optical gating technique²⁴ in low-pressure xenon gas (typically 1-5 mbar), and synchronized few-cycle NIR laser pulses with a variable time delay were combined with a hole-drilled mirror and focused together into a second quasi-static gas cell (inner diameter = 1.5

mm) filled with ~20 mbar of H₂ gas. The peak intensity of the NIR laser was $\sim 5 \times 10^{12}$ W/cm². The spectral range of the attosecond pulses was selected using an indium foil filter placed after the first gas cell with transmission extending from ~12-17 eV, which overlaps with the excited state manifold of neutral H₂. After passing through the gas cell, the VUV spectrum was dispersed using a flat-field grazing-incidence spectrometer [114] with a spectral resolution of ~40 meV at 15 eV. The delay was scanned using a mirror mounted on a piezoelectric stage and was actively stabilized to an error of ~25 attoseconds RMS [28] during the experiments. Details of the experimental setup can be found in previous publications [5, 48, 114].

The figure below depicts the measured delay-dependent absorbance of the H₂ target in the vicinity of the bound state manifold. Electronic and nuclear dynamics of the target are revealed through the dependence of the molecular absorption spectrum on the time delay between the isolated attosecond pulse and a few-cycle near infrared (NIR) pulse, where negative (positive) time delays indicate that the attosecond pulse arrives on the target before (after) the peak of the NIR laser envelope. The ATA spectrum is characterized by dense bands of absorption lines, corresponding primarily to the excitation of the B $^1\Sigma_u^+ \leftarrow X^1\Sigma_g^+$, C $^1\Pi_u \leftarrow X$, and D $^1\Pi_u \leftarrow X$ bands [115] which have large absorption cross section [116].

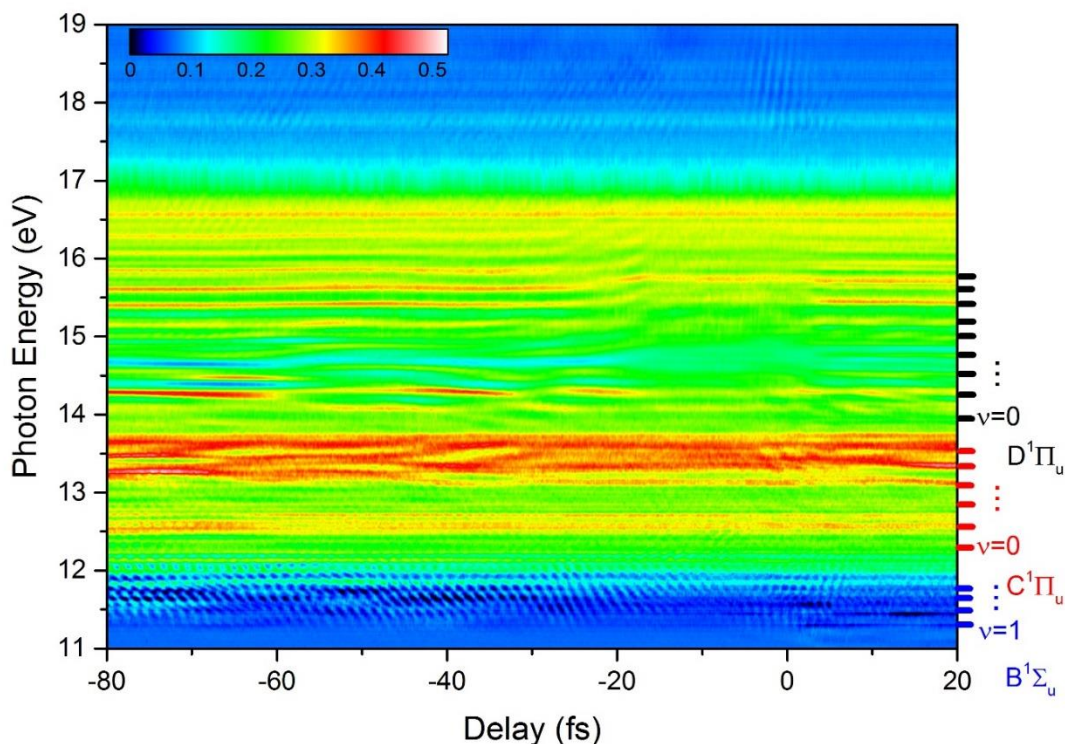


Figure 6-2 Experimentally measured time delay-dependent absorbance spectrum of hydrogen molecules. In the $B^1\Sigma_u$ state, absorption lines show fast oscillations with half the laser cycle period, while absorption line splitting and shifting are observed in $C^1\Pi_u$ and $D^1\Pi_u$ states, such features are attributed to electronic dynamics. These features revive as slow variations on the time scale of nuclear vibration. By performing the attosecond transient absorption experiment in hydrogen molecules, both the electronic and nuclear dynamics can be observed simultaneously.

When the attosecond pulse arrives on the target first, the ATA spectrum reveals delay-dependent changes in the absorption line energies, shapes, and strengths. In general, these dynamics can be attributed to a process wherein the attosecond pulse induces a time-dependent dipole response in the molecular target, which is interrupted by the NIR field [117]. The mechanism of the laser perturbation can be further classified by scrutinizing the absorption dynamics within a particular excited state absorption line: resonant processes involving coupling

of neighboring states through the absorption or emission of one NIR photon typically result in relatively slowly varying spectral features such as absorption line splitting (analogous to Autler-Townes splitting [118]) and the formation of light-induced structures [110], whereas nonresonant couplings involving two or more NIR photons result in fast oscillations with periodicity shorter than the dressing laser optical cycle [48]. These features reveal information about the field-free evolution of the *electron* wavepacket in the interval between the two pulses [56, 77], and are also ubiquitous features in both the experimental and calculated H₂ ATA spectra. On the other hand, the molecular dipole can also be perturbed by the *nuclear* dynamics. Under the adiabatic approximation, the electronic response to the nuclear motion is instantaneous, such that the time-dependent dipole is further modulated on the timescale of the nuclear vibrations. This modulation can be observed in ATAS as relatively slow oscillations on the timescale of the nuclear vibration, which are the focus of the current study. For the data in the figure above, we identify four distinct regions in which the nuclear motion within a particular electronic state can be discerned from the experiment, corresponding approximately to the B←X (11.0-12.5 eV), C←X (13.0-14.0 eV), and D←X (14.0-15.0 eV) transitions of neutral H₂, as well as to transitions in the vicinity of the ²Σ_g⁺ 1sσ_g and 2pσ_u states of H₂⁺ (17.5-19.0 eV). In each of these regions, periodic recurrences of the absorption line dynamics (splitting, shifting, and modulation) are observed to revive periodically, with periodicity approximately equal to the full vibrational period of the associated state. These structures correspond to vibrational revivals in the wavepacket motion, and indicate the state-resolved observation of wavepacket dynamics evolving on multiple distinct potential energy surfaces. The ability to differentiate these signatures of the electronic and nuclear dynamics in individual excited states suggests the power of ATAS to resolve multi-scale dynamics in more complex systems.

6.3 Theoretical Simulation of Attosecond Transient Absorption Spectroscopy of Molecular Hydrogen

The theory part of this work is in collaboration with Dr. Alberto González-Castrillo, Dr. Alicia Palacios, Dr. Luca Argenti and Dr. Fernando Martín.

The quantum calculations can be used to provide valuable insight into the ATAS measurements by identifying the primary coupling pathways for each electronic state. This allows for the development of model systems including only a few molecular states, for which the transient absorption spectrum can be calculated for arbitrarily long delays while fully accounting for the nuclear motion. Two such model calculations, in which the basis has been restricted to the ground $X \ ^1\Sigma_g^+$ state and either (i) the excited $B \ ^1\Sigma_u^+$ and $E, F \ ^1\Sigma_g^+$ bound states or (ii) the excited $C \ ^1\Pi_u$ and $J \ ^1\Delta_g$ bound states, are shown in Figure 6-3 f and d, respectively. In both cases, only bound vibrational states were included, so that the calculation could be extended to very long times. The first model is appropriate for molecules parallel to the polarization direction and can be compared to the transient absorption in the vicinity of the $B \leftarrow X$ transition, while the second model is appropriate for molecules perpendicular to the polarization direction and can be compared to the transient absorption in the vicinity of the $C \leftarrow X$ transition. The observed absorption line dynamics follow the vibrational periods of the coupled excited states.

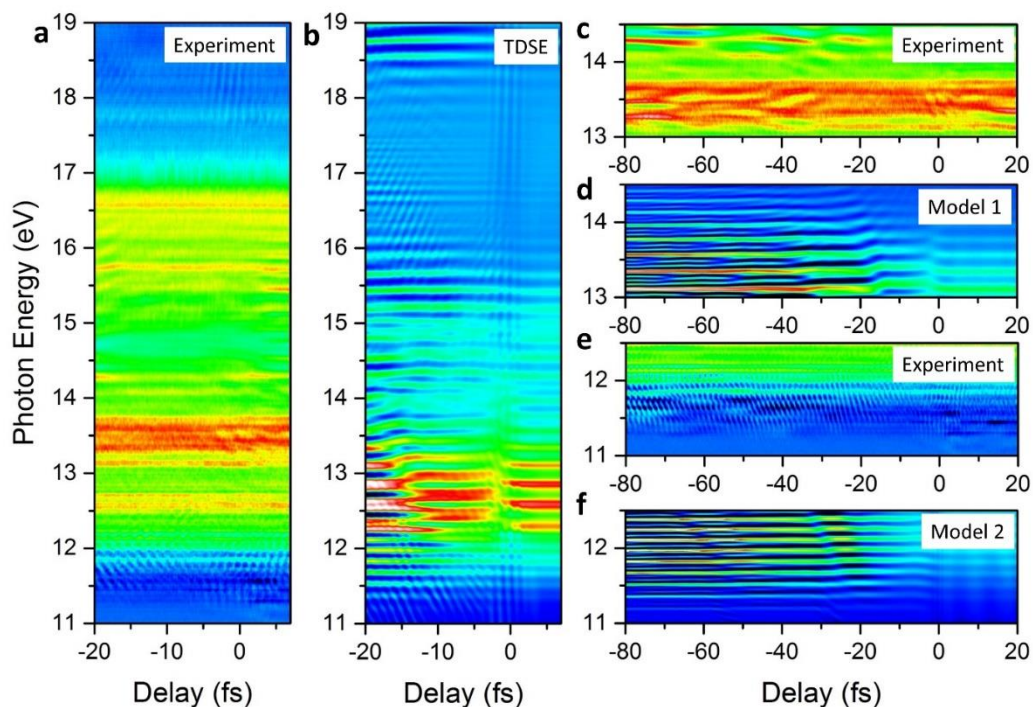


Figure 6-3 ATAS reveals state-resolved electronic and nuclear dynamics. a, the measured delay dependent absorption spectrum of hydrogen molecules near delay zero. b, the ab initio quantum simulations. c and d are the measured and simulated delay dependent absorption spectrum in the vicinity of C $^1\Pi_u$ states, e and f are the measured and simulated delay dependent absorption spectrum near B $^1\Sigma_u^+$ states. Model calculations including only the X $^1\Sigma_g^+$ ground state and d, the C $^1\Pi_u$ and J $^1\Delta_g$ and f, B $^1\Sigma_u^+$ and GK $^1\Sigma_u^+$ excited states, reveal the mechanism behind the state-resolved absorption features.

The time-dependent Schrödinger equation (TDSE) was solved by expanding the time-dependent wave function in a large basis of Born-Oppenheimer (BO) molecular states, which were obtained by diagonalization of the electronic and nuclear Hamiltonians of H_2 in a box of 60 a.u. and 12 a.u., respectively (see Refs. [119, 120]). The method includes all electronic and vibrational (dissociative) degrees of freedom and, therefore, accounts for electron correlation and the nuclear motion. The BO basis includes the six lowest bound states and a set of discretized continuum states for each of the following symmetries: $^1\Sigma_g^+$, $^1\Sigma_u^+$, $^1\Pi_g$, $^1\Pi_u$, and $^1\Delta_g$. All bound-bound and bound-continuum dipole couplings have been included. In the simulation we have

used a VUV pulse of central frequency 15 eV, duration at half maximum 400 as, and intensity 10^{10} W/cm², and an IR pulse of, respectively, 1.7 eV, 4 fs, and 2×10^{12} W/cm². Both pulses have a sine-squared envelope and carrier-envelope phase of 0° . Due to the finite size of the boxes used in the evaluation of the wave function, time integration could only be performed up to 22 fs, which limits our calculations to time delays from -20 to +20 fs. From the calculated time-dependent wave function, the expectation value of the canonical momentum has been obtained as a function of time. It has then been extrapolated analytically to arbitrarily large times beyond the end of the pulses and its Fourier transform numerically evaluated. The ATAS results from the imaginary part of the ratio between the momentum and vector potential Fourier transforms³⁰.

To further study the recurrence effect of the absorption line dynamics, we developed a simple model in which the time dependent wave function resulting from irradiating the molecule with the XUV and IR pulses at time delay τ is defined $\psi(t) = c_g(t)\psi_g(r, R)\chi_{v_g}(R) + \psi_\Pi(r, R)\sum_v c_{v,\tau}(t)\chi_v(R)$ and the coupling between the Π_u and Δ_g states due to the IR pulse is entirely neglected. Using this model, we found that the recurrence effect originates from quantum beats between laser-perturbed vibrational states. This is confirmed by a two-dimensional (2D) spectral analysis of both the experimental and model data in the vicinity of the C←X transition. Laser quenching of the population of a given excited state results the formation of spectral sidebands which depend on both energy and delay. The signature of this perturbed free decay can be observed in the 2D spectra as lines with unity slope, intercepting the spectral axis at the energy of the unperturbed bound state. We find that the quantum beats observed in the delay-dependent spectrum appear at the intersection of Fourier lines associated with neighboring vibrational states, and that these intersections approximately map the periods of the vibrational

states in the Π_u electronic state. Consecutive vibrational levels ($\Delta j = \pm 1$) cross when the Fourier frequency is equal to half of their energy differences), resulting in the prominent beats observed in the experiments, and higher-order beats can be observed at larger Fourier frequencies where laser-perturbed vibrational levels differing by $\Delta j = \pm 2$ intersect.

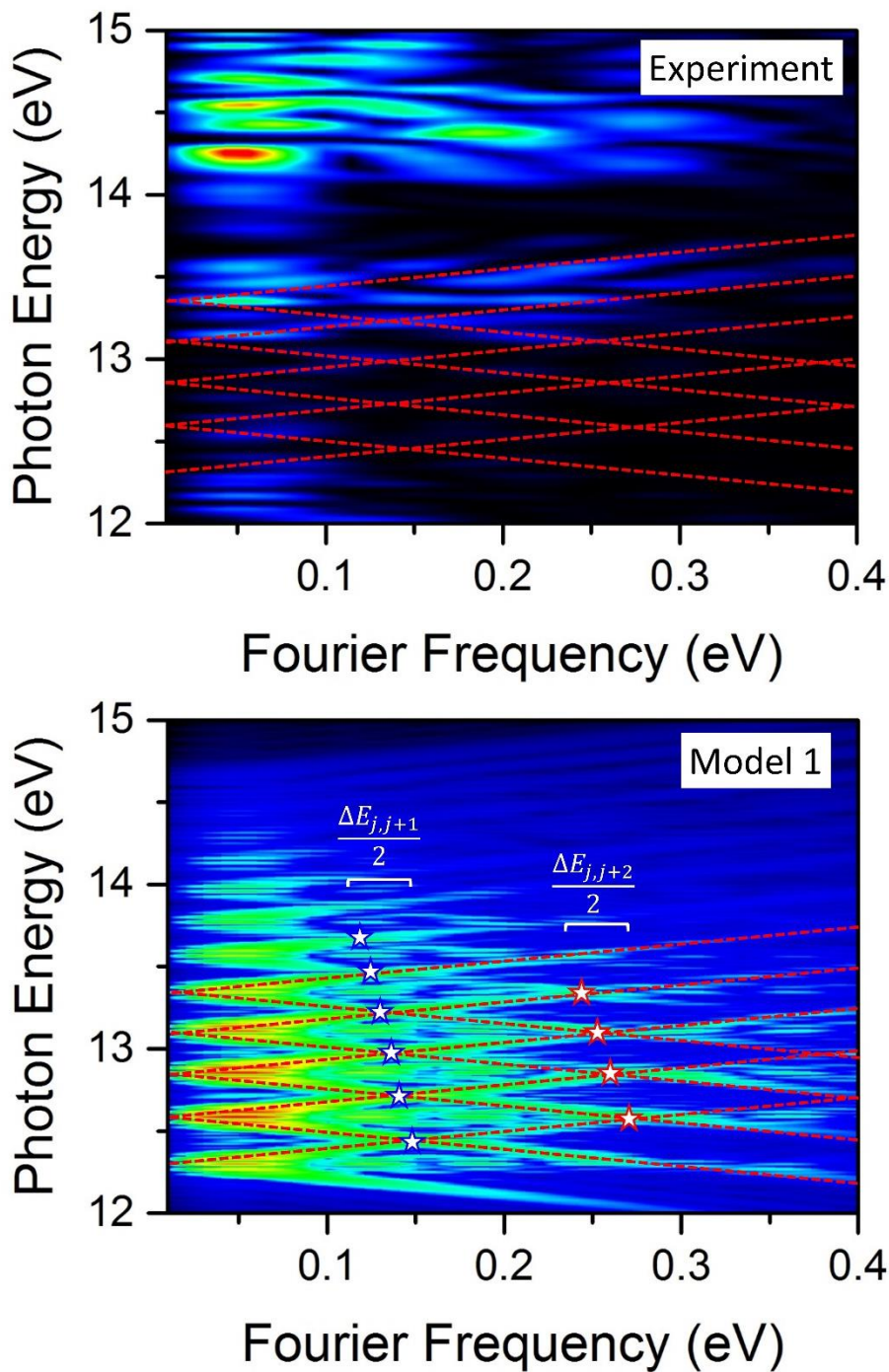


Figure 6-4 Fourier transform analysis of measured (a) and simulated (b) delay dependent absorption spectrum. Quantum beats in the delay dependent absorption spectrum can be observed as crossings of Fourier lines associated with different laser-perturbed vibrational states. Consecutive vibrational levels cross when the Fourier frequency is equal to half of their energy differences (blue stars), while intersections at larger Fourier frequencies indicate higher-order crossings (red stars).

To study the recurrence effect of the absorption line dynamics, we developed a simple model in which the time dependent wave function resulting from irradiating the molecule with the XUV and IR pulses at time delay τ is defined $\psi(t) = c_g(t)\psi_g(r, R)\chi_{v_g}(R) + \psi_{\Pi}(r, R)\sum_v c_{v,\tau}(t)\chi_v(R)$, where the expansion coefficients are given by the analytical formula $c_{v,\tau}(t) = F(\omega_v) \text{erf}\left[\frac{t}{\sigma_{XUV}}\right] \left(1 - \text{erf}\left[\frac{\tau-t}{\sigma_{IR}}\right]\right) \langle \chi_v | \chi_{v_g} \rangle \exp(-i\omega_{vg}t)$ in which $F(\omega_v)$ is a normalization factor that accounts for the XUV pulse spectrum and the dipole-transition matrix element between the ground and the Π_u state so that $|c_g|^2 + \sum_v |c_{v,\tau}|^2 = 1$ at all times.

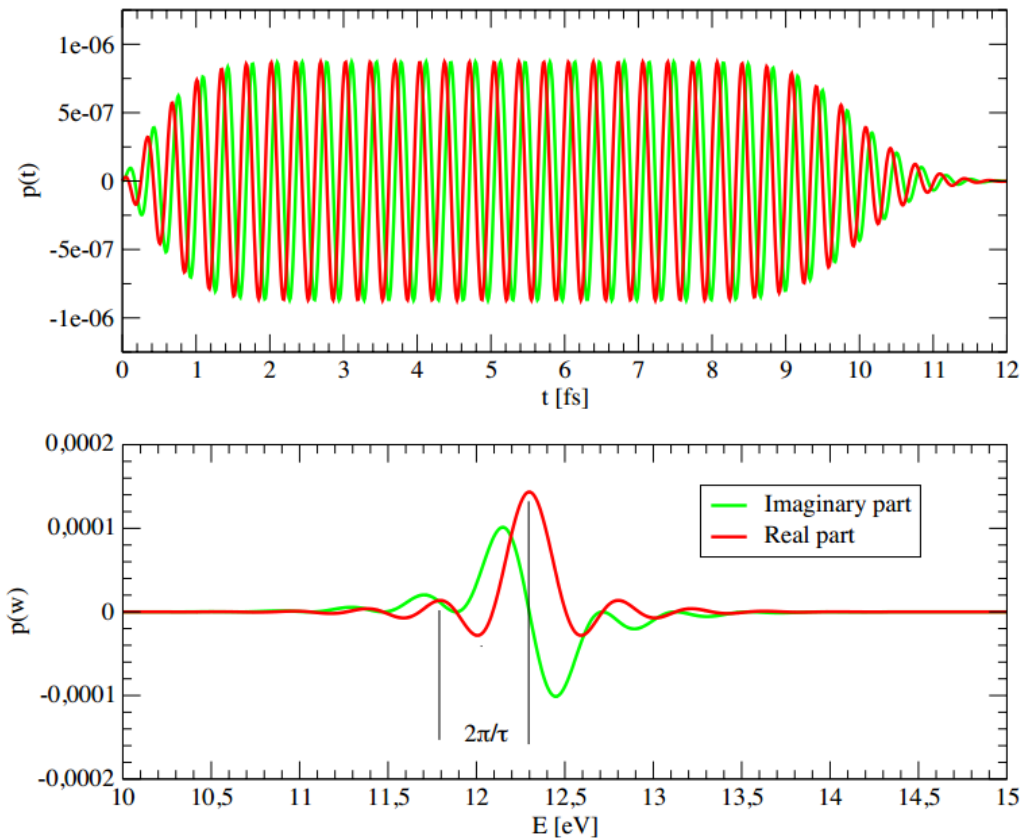


Figure 6-5 Plot of the polarization in the time and energy domain for a single vibrational state.

In this formula, which is only valid when the XUV and IR pulses do not overlap, we are assuming that the modulus of the c_ν amplitudes increase during a time interval σ_{XUV} , then remains constant during approximately a time interval τ , and then go to zero again during a time interval σ_{IR} . So the coupling between the Π_u and Δ_g states due to the IR pulse is entirely neglected. Under these assumptions, the time dependent dipole is given by $P_\tau(t) = \langle \psi(t) | \mu | \psi(t) \rangle$, and the ATAS spectrum is simply proportional to the Fourier transform of $P_\tau(t)$. The results obtained with this simple analytic treatment are shown in Figure 6-6 for the cases of a single $\nu = 0$ vibrational level, the two vibrational levels $\nu = 0$ and $\nu = 1$, and all vibrational levels in the Π_u state. The corresponding results obtained from the reduced TDSE calculations in which only the Σ_g , Π_u and Δ_g electronic states were included are shown in Figure 6-7. As can be seen, except the region of time delays where the XUV and IR pulse overlap, the agreement between both sets of calculations is very good.

The Fourier transform of the c_ν amplitude leads to a prominent peak at $\omega = \omega_{0,\nu}$, where $\omega_{0,\nu}$ is the frequency of the vibrational motion in the ν vibrational state, and satellite peaks, symmetric with respect to the central frequency $\omega_{0,\nu}$, whose intensity rapidly decreases as one moves apart from $\omega_{0,\nu}$. The position of all maxima are approximately given by the expression $\omega_{n,\nu} = \omega_{0,\nu} + n \frac{2\pi}{\tau} = \frac{2\pi}{T_\nu} + n \frac{2\pi}{\tau}$, where n is an integer number associated with the order of the peak and T_ν is the vibrational period in the ν vibrational state. As time delay increases, the satellite peaks approach the central peak. One has a similar expression for every ν , so it is possible that, for two different vibrational states ν and ν' and peak orders n and m , respectively, one has $\omega_{n,\nu} = \omega_{m,\nu'}$. This situation arises quite often when τ is continuously varied, leading to crossings in the Fourier lines associated to different vibrational states. The time delays at which these crossings can occur are given by $\tau = mT_{\nu'} - nT_\nu$. The smallest values of τ at which the

crossings can be visible correspond to orders of $m = n \pm 1$. For consecutive vibrational levels, $T_{v'} = T_v$, so that $\tau = T_v$. Therefore, the intersections of the Fourier lines approximately map the periods of the vibrational states in the Π_u electronic state. This is the reason why in the ab initio ATAS spectra, as well as in its reduced TDSE version, one can see the signatures of the Π_u potential energy curve of H_2 as a function of τ . The mapping is periodically reproduced at longer time delays when the Fourier orders differ by more than 1.

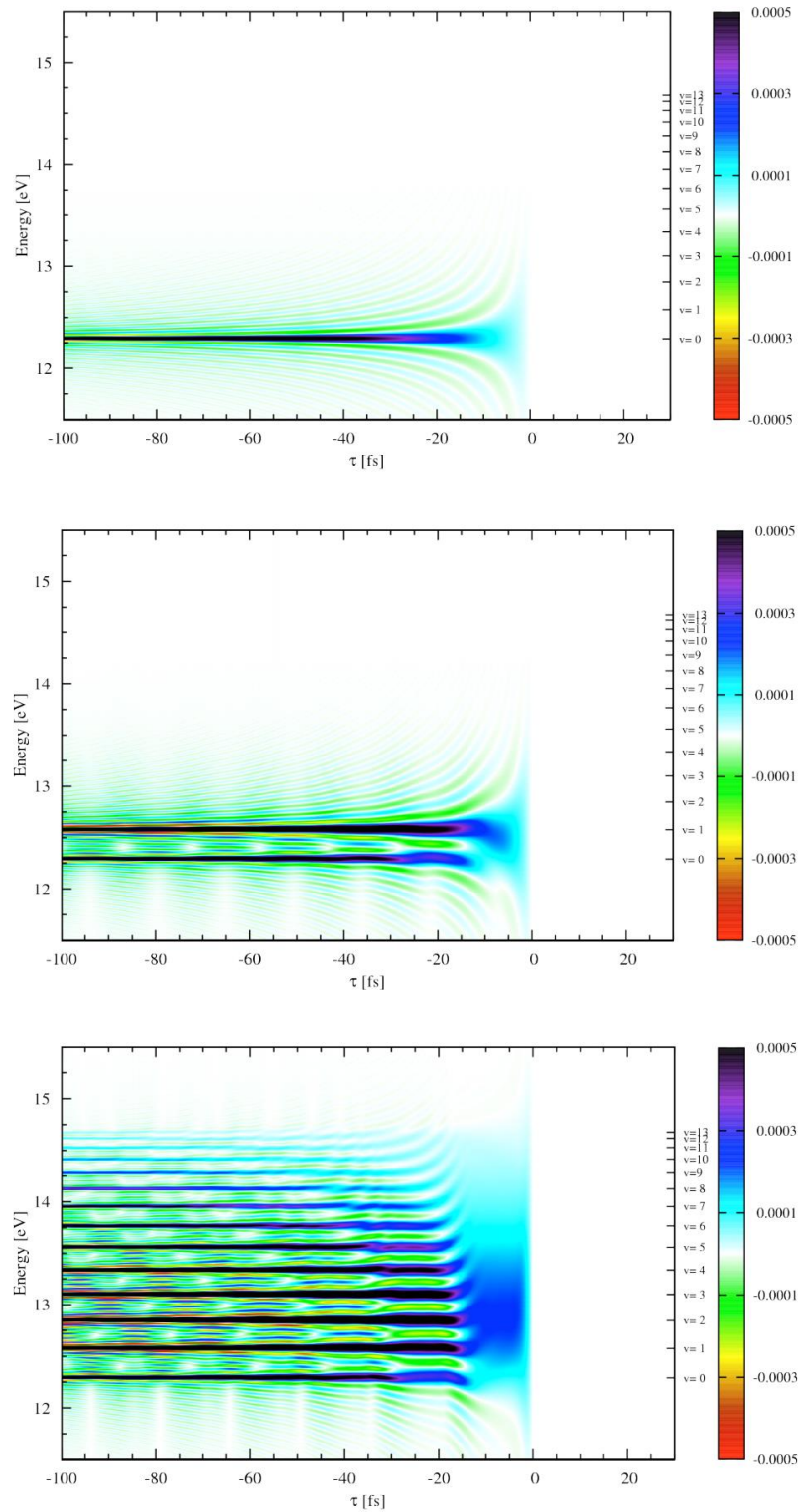


Figure 6-6 ATAS spectrum obtained from the analytical model. Upper panel: only the $v=0$ state is included. Central panel: only $v=0$ and $v=1$ states are included. Bottom panel: all v 's are included. Adapted from [121]

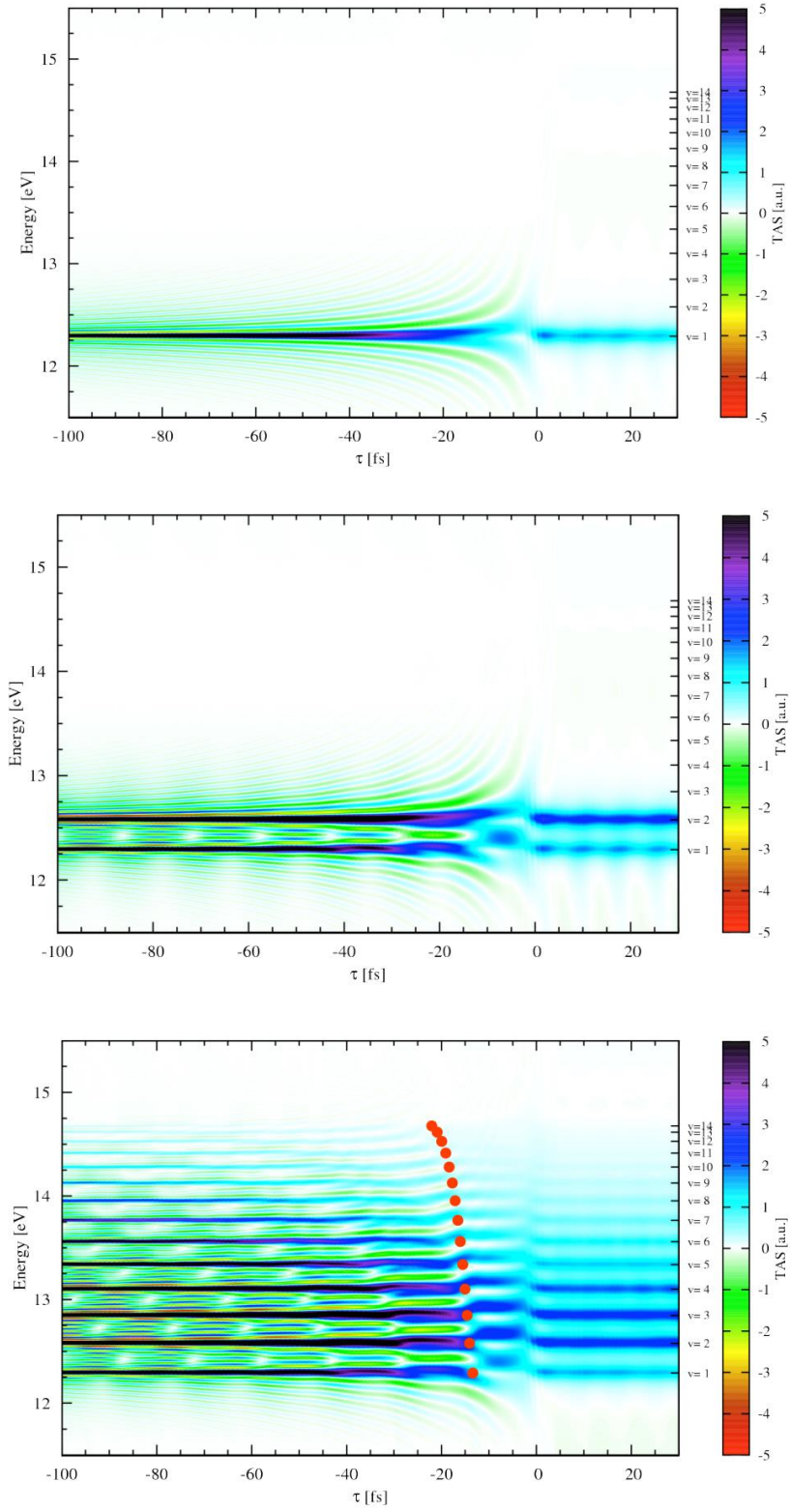


Figure 6-7 ATAS spectrum obtained from the reduced TDSE calculations. Upper panel: only the $v=0$ state is included. Central panel: only $v=0$ and $v=1$ states are included. Bottom panel: all v 's are included. Adapted from [121]

In the region where the XUV and IR pulses overlap, one should see the lines associated with dressed vibronic states. Indeed, the IR field couples the Π_u and Δ_g states, and due to its relatively large intensity, should have a non-negligible effect on the position of the corresponding vibrational states. To prove it, we have diagonalized the Floquet matrix and plotted the values of the eigenvalues as a function of the IR intensity. Since not all Π_u vibronic states are equally populated by the XUV pulse, the intensity of the line associated to a given eigenvalue has been multiplied by the square of the dipole transition amplitude connecting the initial vibronic state with the Π_u vibronic state and the square of the corresponding Floquet coefficient. One can see the familiar Autler-Townes splitting, which become more and more pronounced as the intensity of the IR field increases. One can also see a lot of avoided crossings, which are due to the proximity of the unperturbed vibronic energies. In order to compare the results of this figure with those shown in the previous ones, one should take into account that, in the Floquet picture, the amplitude (i.e., the intensity) of the IR pulse remains constant at all times and forever, which that of the actual pulse is only different from zero in a finite time interval and has a \sin^2 envelope. So, for a meaningful comparison, one should rather use the average value of the latter intensity, which is roughly four times smaller than the peak intensity.

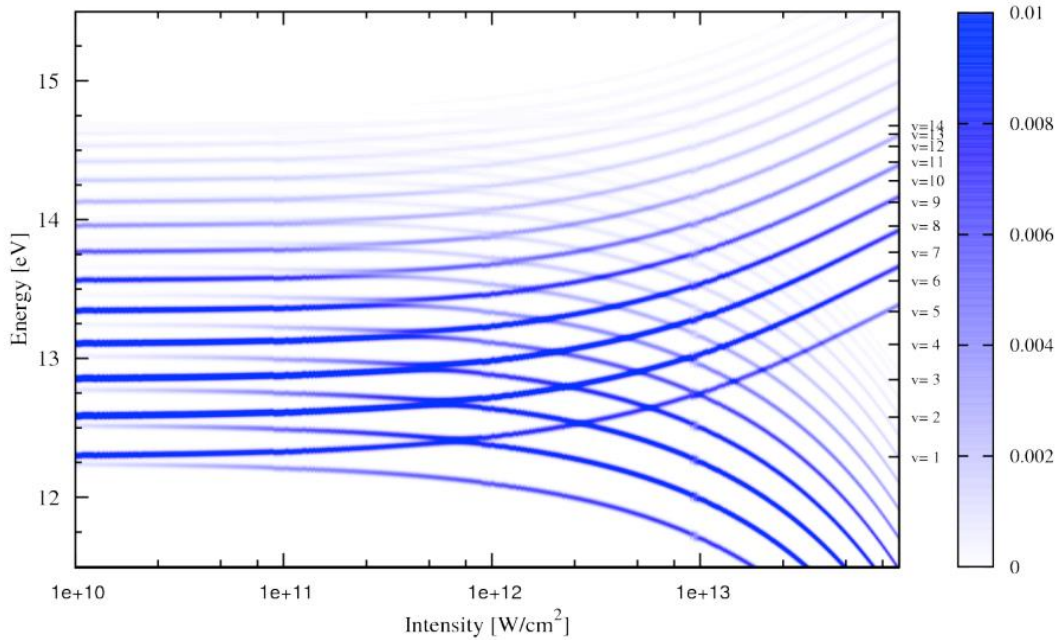


Figure 6-8 Eigenvalues of the Floquet matrix as a function of IR intensity. Adapted from [121]

For the peak intensity used in our TDSE calculations, $2 \times 10^{12} W/cm^2$, which corresponds to an average intensity of $5 \times 10^{11} W/cm^2$, we are in the vicinity of a series of avoided crossings. These crossings appear at energies roughly in between two consecutive vibrational states. As a result, one can expect to observe lines lying in between the energies of the unperturbed vibrational states. This is precisely what is observed in the region of the ATAS spectrum where the XUV and IR pulses overlap. At higher or lower intensities, the pattern should be different.

When longer and more intense pulses are used, one can see the the following figure that the interval of time delays in which the coupling between the Π_u and Δ_g states shows up is also longer. In this region, the ATAS spectrum becomes much more complicated than for shorter and less intense pulses, since pure Fourier transform effects are superimposed to the Autler-Townes multiple splittings due to the IR-induced coupling between the Π_u and Δ_g states. In the region

where the two pulses do not overlap any more, the ATAS spectrum reflects the same Fourier transform effects as discussed before.

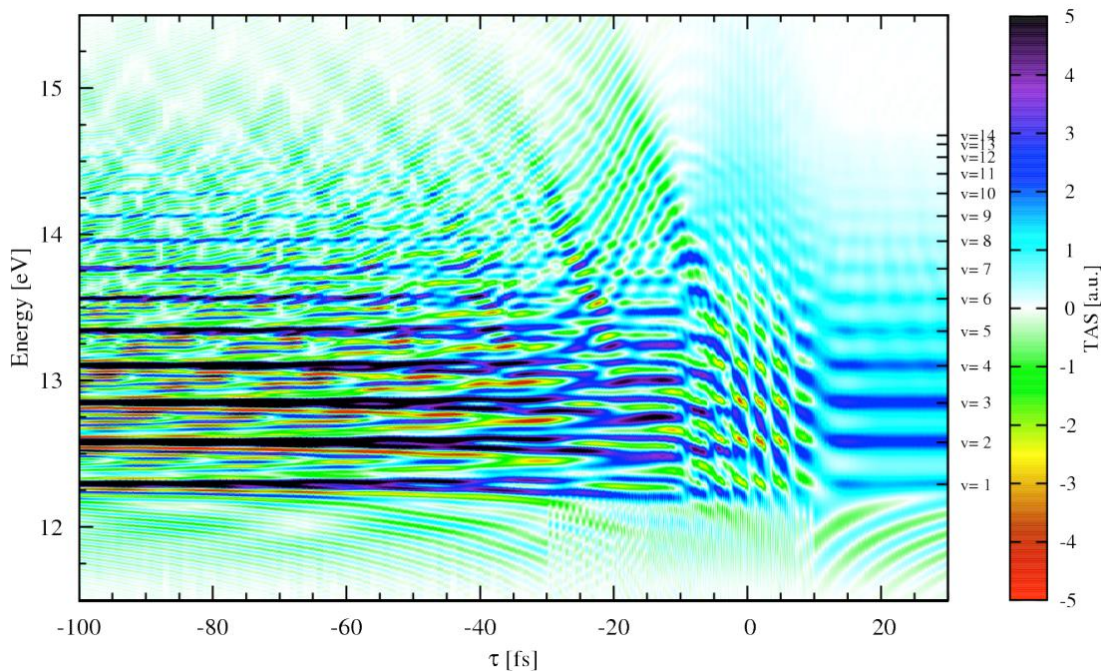


Figure 6-9 ATAS spectrum obtained from the reduced TDSE calculations. The intensity of the IR pulse is 10 times larger than that of Figure 6-7. Adapted from [121]

We have repeated the calculations by using the chirped pulse shown in the figure below. We have chosen a large chirp to check if this has any noticeable influence on the results. Notice, however, that the spectrum of the chirped pulse is nearly identical to the unchirped one, so that we ensure that the same states are populated with both kinds of pulses.

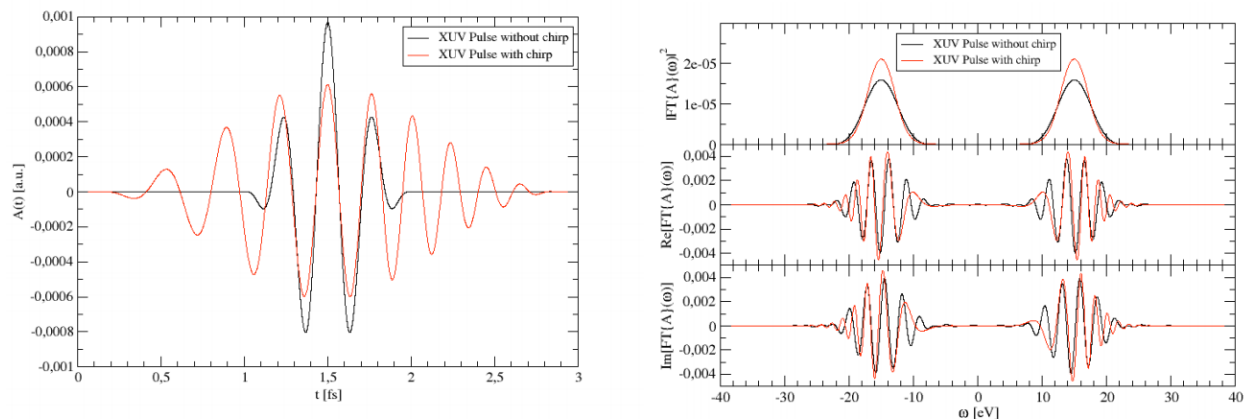


Figure 6-10 Left panel: Chirped and unchirped pulses used in the calculations. Right panel: Fourier transform of the two pulses. Adapted from [121]

As can be seen, the two absorption spectra are very similar, the effects expected from the chirp are somewhat hidden in the forest of lines discussed in the previous sections.

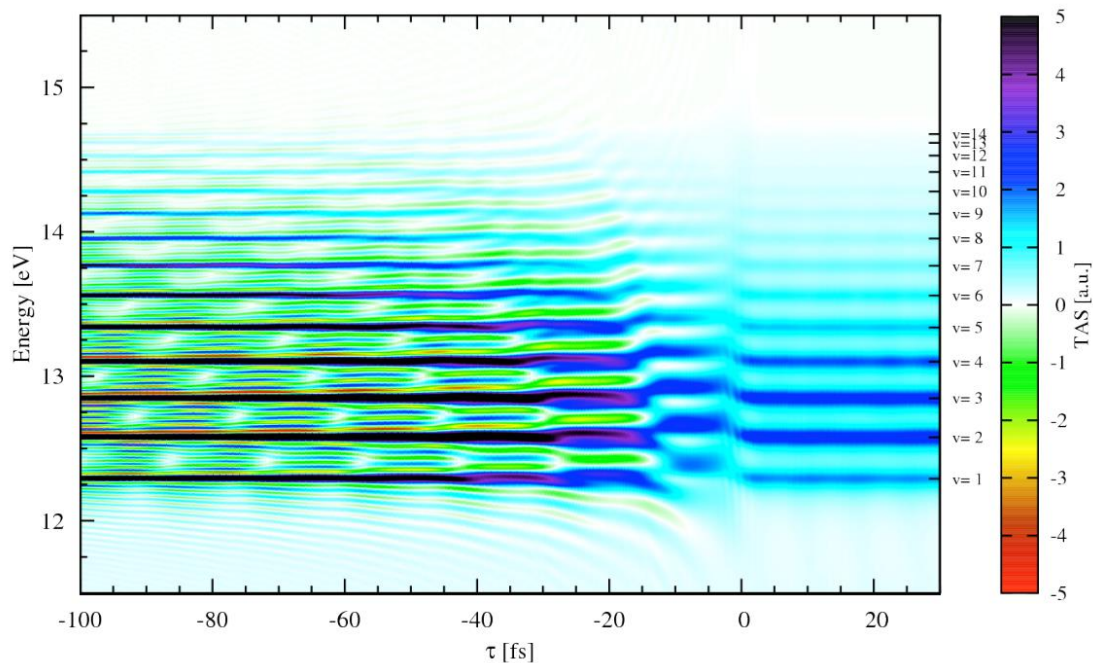


Figure 6-11 ATAS spectrum obtained from the reduced TDSE calculations using the chirped pulses. Adapted from [121]

6.4 Quantum Control in Attosecond Spectroscopy

The ATAS of H₂ presents an attractive scheme for attosecond quantum control in larger molecules evolving on multidimensional potential surfaces. Since the initial attosecond excitation determines the evolution of both the electronic and nuclear dynamics, it should be possible to shape the initial electronic wavepacket in such a way as to optimize the efficiency of pre-selected dissociation pathways and reaction products [122]. This can be done either by shaping the spectral amplitude and phase of the attosecond pulse [123] or by altering the wavepacket amplitude and phase with the addition of an overlapping control pulse [124]. Here, we demonstrate a rudimentary form of control by adding a weak, few-cycle NIR control pulse with intensity of $\sim 1 \times 10^{11}$ W/cm² which overlaps in time with the VUV attosecond pulse. In the presence of the NIR laser, the dipole selection rules for the VUV pulse are modified and the attosecond excitation results in a different initial wavepacket. We then probe the ensuing wavepacket dynamics by repeating the ATAS experiment, with two NIR laser pulses: the weak control pulse, which is locked in phase to the VUV attosecond pulse, and the strong perturbing pulse, which arrives at a variable time delay. While this may result in optical interference between the two NIR fields near zero delay, the wavepacket dynamics can be probed for delays of -20 fs and longer where the two NIR fields no longer overlap. Compared to the case of excitation by the VUV pulse alone, the transient absorption spectrum is more strongly modulated and exhibits oscillations with both half- and full-cycle periodicity. These changes indicate a substantial modification of the excited wavepacket, and are easily observed in spite of the low intensity of the control pulse. In the future, such a scheme could be implemented with a tunable control field or pulse shaping device to exert control in attosecond photochemistry.

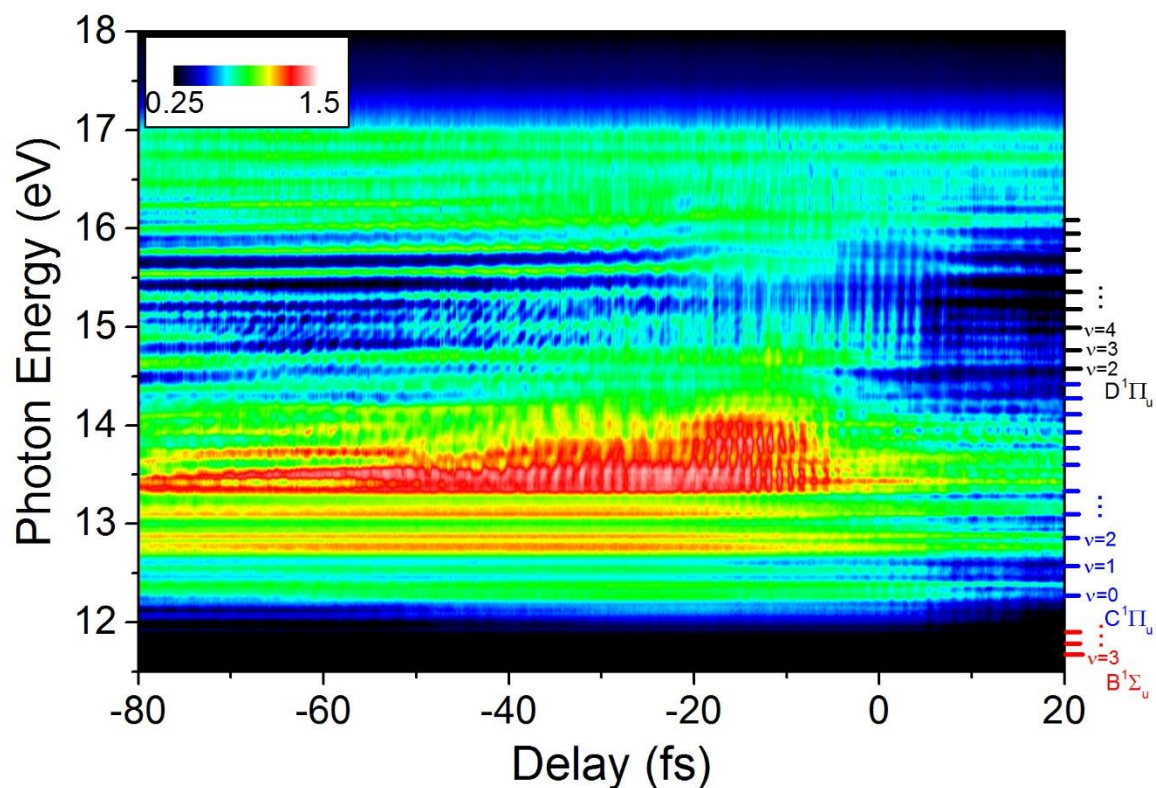


Figure 6-12 | Quantum control in attosecond photochemistry. A weak, few-cycle NIR “control” pulse, which overlaps in time with the VUV attosecond pulse, modifies the attosecond excitation dynamics. The strong modulation of the ATAS indicates the modification of the initial wavepacket, suggesting a mechanism for attosecond quantum control.

ATAS has proven valuable to the study of wavepacket dynamics and electron correlation in excited states of atoms and condensed matter. Here, we demonstrate its applicability to probing the electronic and nuclear dynamics simultaneously with high temporal and spectra resolution in hydrogen molecules. Unlike attosecond photoelectron and photoion spectroscopies, the ATAS measurements are capable of resolving dynamics on multiple potential energy surfaces with attosecond time resolution and state selectivity, without requiring a subsequent ionization step. The measurements suggest ATAS as a suitable platform for attosecond measurement in the first steps of a photochemical reaction.

CHAPTER 7 - FINAL REMARKS

In this thesis, I have discussed the probing and controlling of atomic and molecular dynamics by using the attosecond transient absorption spectroscopy technique. In chapter two, I presented the fundamental knowledge of how to generate single isolated attosecond pulses, which is used as the probe in the attosecond transient absorption spectroscopy experiments. In chapter three, four and six, I reported our progress on utilizing single isolated attosecond pulses on probing electron dynamics in helium/neon/argon/krypton atoms and probing molecular dynamics in hydrogen molecules. The target atom/molecule is first pumped into excited states and then probed by a subsequent attosecond XUV pulse or by an NIR laser pulse. By measuring the absorbed attosecond XUV pulse spectrum, the ultrafast electron correlation dynamics can be studied in real time. The quantum processes that can be studied using the attosecond transient absorption spectroscopy include the AC Stark shift, multi-photon absorption, intermediate states of atoms, autoionizing states, and transitions of vibrational states in molecules. In all experiments, the absorption changes as a function of the time delay between the attosecond XUV probe pulse and the dressing NIR laser pulse, on a time scale of sub cycle laser period, which reveals attosecond electron dynamics.

This is the beginning of studying and controlling electron and nuclear dynamics in atoms and molecules with attosecond transient absorption spectroscopy. With the development of the next generation of attosecond sources with micro-Joule pulse energy, attosecond-pump-attosecond-probe transient absorption experiments will be possible, this will allow us to study the excitation and control of electron dynamics on the few-attosecond time scale. In addition, the first application of attosecond transient absorption spectroscopy to the study of laser induced dynamics in atoms and simple molecules opens the door to the study of complex optical

phenomena in large molecules and solid materials, with the ultimate goal of “filming” chemical reactions and electron transportation.

APPENDIX A: LIST OF PUBLICATIONS

Peer-Reviewed Journal Publications

1. Y. Cheng, M. Chini, X. Wang, A. González-Castrillo, A. Palacios, L. Argenti, F. Martín, and Z. Chang, "Probing Electronic and Nuclear Dynamics in Molecules with Attosecond Transient Absorption," (under submission).
2. M. Chini, X. W. Wang, Y. Cheng, and Z. H. Chang, "Resonance effects and quantum beats in attosecond transient absorption of helium," *J Phys B-at Mol Opt* **47** (2014).
3. Q. Zhang, K. Zhao, J. Li, M. Chini, Y. Cheng, Y. Wu, E. Cunningham, and Z. H. Chang, "Suppression of driving laser in high harmonic generation with a microchannel plate," *Opt Lett* **39**, 3670-3673 (2014).
4. M. Chini, X. W. Wang, Y. Cheng, H. Wang, Y. Wu, E. Cunningham, P. C. Li, J. Heslar, D. A. Telnov, S. I. Chu, and Z. H. Chang, "Coherent phase-matched VUV generation by field-controlled bound states," *Nat Photonics* **8**, 437-441 (2014).
5. X. W. Wang, M. Chini, Y. Cheng, Y. Wu, X. M. Tong, and Z. H. Chang, "Subcycle laser control and quantum interferences in attosecond photoabsorption of neon," *Phys Rev A* **87** (2013).
6. M. Chini, X. W. Wang, Y. Cheng, Y. Wu, D. Zhao, D. A. Telnov, S. I. Chu, and Z. H. Chang, "Sub-cycle Oscillations in Virtual States Brought to Light," *Sci Rep-Uk* **3** (2013).
7. X. Wang, M. Chini, Y. Cheng, Y. Wu, and Z. Chang, "In situ calibration of an extreme ultraviolet spectrometer for attosecond transient absorption experiments," *Appl Optics* **52**, 323-329 (2013).
8. M. Chini, B. Zhao, H. Wang, Y. Cheng, S. Hu, and Z. Chang, "Subcycle ac stark shift of helium excited states probed with isolated attosecond pulses," *Phys Rev Lett* **109**, 073601 (2012).

9. M. Möller, Y. Cheng, S. D. Khan, B. Zhao, K. Zhao, M. Chini, G. G. Paulus, and Z. Chang, "Dependence of high-order-harmonic-generation yield on driving-laser ellipticity," *Phys Rev A* **86**, 011401 (2012).
10. S. D. Khan, Y. Cheng, M. Möller, K. Zhao, B. Zhao, M. Chini, G. G. Paulus, and Z. Chang, "Ellipticity dependence of 400 nm-driven high harmonic generation," *Appl Phys Lett* **99**, 161106 (2011).
11. H. Wang, M. Chini, S. Y. Chen, C. H. Zhang, F. He, Y. Cheng, Y. Wu, U. Thumm, and Z. H. Chang, "Attosecond Time-Resolved Autoionization of Argon," *Phys Rev Lett* **105** (2010).

Invited Book Chapters

1. M. Chini, H. Wang, B. Zhao, Y. Cheng, S. Chen, Y. Wu, and Z. Chang, "Attosecond Absorption Spectroscopy," in Progress in Ultrafast Intense Laser Science(Springer Berlin Heidelberg, 2013), pp. 135-150.

Invited talks

1. Yan Cheng, "Attosecond transient absorption experiments in atoms and molecules ",
OSA Graduate Research Symposium, CREOL, University of Central Florida, 2014,
Orlando, USA

Selected Conference Presentations

1. Y. Cheng, M. Chini, X.-M. Tong, A. Chew, J. Biedermann, Y. Wu, E. Cunningham, and Z. Chang, "Quantum beats in attosecond time-resolved autoionization of krypton," *Bulletin of the American Physical Society* **60** (2015).
2. Y. Cheng, M. Chini, X.-M. Tong, A. Chew, J. Biedermann, Y. Wu, E. Cunningham, and Z. Chang, "Quantum Beats in Attosecond Transient Absorption of Krypton Autoionizing States," in *CLEO: QELS_Fundamental Science*(Optical Society of America, 2015), p. FTh3C. 3.
3. Y. Cheng, M. Chini, X. Wang, Y. Wu, and Z. Chang, "Attosecond Transient Absorption in Molecular Hydrogen," in *CLEO: QELS_Fundamental Science*(Optical Society of America, 2014), p. FM2B. 3.
4. Y. Cheng, M. Chini, X. Wang, Y. Wang, Y. Wu, and Z. Chang, "Probing molecular dynamics using attosecond transient absorption," *Bulletin of the American Physical Society* **58** (2013).
5. Y. Cheng, M. Chini, X. Wang, Y. Wu, and Z. Chang, "Probing Hydrogen and Deuterium Molecular Dynamics Using Attosecond Transient Absorption," in *Laser Science*(Optical Society of America, 2013), p. LW2H. 2.
6. Y. Cheng, S. D. Khan, B. Zhao, K. Zhao, M. Chini, and Z. Chang, "Broadband high harmonic generation from 400 nm sub-10 fs driving pulses," in *Quantum Electronics and Laser Science Conference*(Optical Society of America, 2012), p. JW4A. 23.
7. Y. Cheng, S. Khan, K. Zhao, B. Zhao, M. Chini, and Z. Chang, "Ellipticity dependence of high harmonics generated using 400 nm driving lasers," in *APS Division of Atomic, Molecular and Optical Physics Meeting Abstracts*(2011), p. 5004.

APPENDIX B: COPYRIGHT PERMISSIONS

**American Physical Society
License Details**

Sep 23, 2015

This is an Agreement between Yan Cheng ("You") and American Physical Society ("Publisher"). It consists of your order details, the terms and conditions provided by American Physical Society, and the payment instructions.

| | |
|---|--|
| License Number | 3714840335865 |
| License date | Sep 23, 2015 |
| Licensed content publisher | American Physical Society |
| Licensed content publication | Physical Review A |
| Licensed content title | Subcycle laser control and quantum interferences in attosecond photoabsorption of neon |
| Licensed copyright line | ©2013 American Physical Society |
| Licensed content author | Xiaowei Wang et al. |
| Licensed content date | Jun 17, 2013 |
| Volume number | 87 |
| Type of Use | Thesis/Dissertation |
| Requestor type | Student |
| Format | Electronic |
| Portion | chapter/article |
| Rights for | Main product |
| Duration of use | Life of current edition |
| Creation of copies for the disabled | no |
| With minor editing privileges | no |
| For distribution to | Worldwide |
| In the following language(s) | Original language plus all translations |
| Specific languages | English |
| With incidental promotional use | no |
| The lifetime unit quantity of new product | 0 to 499 |
| The requesting person/organization is: | Yan Cheng, University of Central Florida |
| Order reference number | None |
| Title of your thesis / dissertation | ATTOSECOND TRANSIENT ABSORPTION SPECTROSCOPY OF ATOMS AND MOLECULES |
| Expected completion date | Dec 2015 |
| Expected size (number of pages) | 150 |
| Total | 0.00 USD |

**American Physical Society
License Details**

Sep 23, 2015

This is an Agreement between Yan Cheng ("You") and American Physical Society ("Publisher"). It consists of your order details, the terms and conditions provided by American Physical Society, and the payment instructions.

| | |
|---|---|
| License Number | 3714840475628 |
| License date | Sep 23, 2015 |
| Licensed content publisher | American Physical Society |
| Licensed content publication | Physical Review Letters |
| Licensed content title | Subcycle ac Stark Shift of Helium Excited States Probed with Isolated Attosecond Pulses |
| Licensed copyright line | © 2012 American Physical Society |
| Licensed content author | Michael Chini et al. |
| Licensed content date | Aug 16, 2012 |
| Volume number | 109 |
| Type of Use | Thesis/Dissertation |
| Requestor type | Student |
| Format | Electronic |
| Portion | chapter/article |
| Rights for | Main product |
| Duration of use | Life of current edition |
| Creation of copies for the disabled | no |
| With minor editing privileges | no |
| For distribution to | Worldwide |
| In the following language(s) | Original language plus all translations |
| Specific languages | English |
| With incidental promotional use | no |
| The lifetime unit quantity of new product | 0 to 499 |
| The requesting person/organization is: | Yan Cheng, University of Central Florida |
| Order reference number | None |
| Title of your thesis / dissertation | ATTOSECOND TRANSIENT ABSORPTION SPECTROSCOPY OF ATOMS AND MOLECULES |
| Expected completion date | Dec 2015 |
| Expected size (number of pages) | 150 |
| Total | 0.00 USD |

**American Physical Society
License Details**

Sep 23, 2015

This is an Agreement between Yan Cheng ("You") and American Physical Society ("Publisher"). It consists of your order details, the terms and conditions provided by American Physical Society, and the payment instructions.

| | |
|---|---|
| License Number | 3714840557217 |
| License date | Sep 23, 2015 |
| Licensed content publisher | American Physical Society |
| Licensed content publication | Physical Review Letters |
| Licensed content title | Attosecond Time-Resolved Autoionization of Argon |
| Licensed copyright line | © 2010 The American Physical Society |
| Licensed content author | He Wang et al. |
| Licensed content date | Oct 1, 2010 |
| Volume number | 105 |
| Type of Use | Thesis/Dissertation |
| Requestor type | Student |
| Format | Electronic |
| Portion | chapter/article |
| Rights for | Main product |
| Duration of use | Life of current edition |
| Creation of copies for the disabled | no |
| With minor editing privileges | no |
| For distribution to | Worldwide |
| In the following language(s) | Original language plus all translations |
| Specific languages | English |
| With incidental promotional use | no |
| The lifetime unit quantity of new product | 0 to 499 |
| The requesting person/organization is: | Yan Cheng |
| Order reference number | None |
| Title of your thesis / dissertation | ATTOSECOND TRANSIENT ABSORPTION SPECTROSCOPY OF ATOMS AND MOLECULES |
| Expected completion date | Dec 2015 |
| Expected size (number of pages) | 150 |
| Total | 0.00 USD |

**American Physical Society
License Details**

Sep 23, 2015

This is an Agreement between Yan Cheng ("You") and American Physical Society ("Publisher"). It consists of your order details, the terms and conditions provided by American Physical Society, and the payment instructions.

| | |
|---|---|
| License Number | 3714840158258 |
| License date | Sep 23, 2015 |
| Licensed content publisher | American Physical Society |
| Licensed content publication | Physical Review A |
| Licensed content title | Dependence of high-order-harmonic-generation yield on driving-laser ellipticity |
| Licensed copyright line | ©2012 American Physical Society |
| Licensed content author | Max Möller et al. |
| Licensed content date | Jul 26, 2012 |
| Volume number | 86 |
| Type of Use | Thesis/Dissertation |
| Requestor type | Student |
| Format | Electronic |
| Portion | chapter/article |
| Rights for | Main product |
| Duration of use | Life of current edition |
| Creation of copies for the disabled | no |
| With minor editing privileges | no |
| For distribution to | Worldwide |
| In the following language(s) | Original language plus all translations |
| Specific languages | English |
| With incidental promotional use | no |
| The lifetime unit quantity of new product | 0 to 499 |
| The requesting person/organization is: | Yan Cheng, University of Central Florida |
| Order reference number | None |
| Title of your thesis / dissertation | ATTOSECOND TRANSIENT ABSORPTION SPECTROSCOPY OF ATOMS AND MOLECULES |
| Expected completion date | Dec 2015 |
| Expected size (number of pages) | 150 |
| Total | 0.00 USD |

Terms and Conditions

The American Physical Society (APS) is pleased to grant the Requestor of this license a non-exclusive, non-transferable permission, limited to [**print** and/or **electronic** format, depending on what they chose], provided all criteria outlined below are followed.

1. For electronic format permissions, Requestor agrees to provide a hyperlink from the reprinted APS material using the source material's DOI on the web page where the work appears. The hyperlink should use the standard DOI resolution URL, <http://dx.doi.org/{DOI}>. The hyperlink may be embedded in the copyright credit line.
2. For print format permissions, Requestor agrees to print the required copyright credit line on the first page where the material appears: "Reprinted (abstract/excerpt/figure) with permission from [FULL REFERENCE CITATION] as follows: Author's Names, APS Journal Title, Volume Number, Page Number and Year of Publication.] Copyright (YEAR) by the American Physical Society."
3. Permission granted in this license is for a one-time use and does not include permission for any future editions, updates, databases, formats or other matters. Permission must be sought for any additional use.
4. Use of the material does not and must not imply any endorsement by APS.
5. Under no circumstance does APS purport or intend to grant permission to reuse materials to which it does not hold copyright. It is the requestors sole responsibility to ensure the licensed material is original to APS and does not contain the copyright of another entity, and that the copyright notice of the figure, photograph, cover or table does not indicate that it was reprinted by APS, with permission from another source.
6. The permission granted herein is personal to the Requestor for the use specified and is not transferable or assignable without express written permission of APS. This license may not be amended except in writing by APS.
7. You may not alter, edit or modify the material in any manner.
8. You may translate the materials only when translation rights have been granted.
9. You may not use the material for promotional, sales, advertising or marketing purposes.
10. The foregoing license shall not take effect unless and until APS or its agent, Copyright Clearance Center (CCC), receives payment in full in accordance with CCC Billing and Payment Terms and Conditions, which are incorporated herein by reference.
11. Should the terms of this license be violated at any time, APS or CCC may revoke the license with no refund to you and seek relief to the fullest extent of the laws of the USA. Official written notice will be made using the contact information provided with the permission request. Failure to receive such notice will not nullify revocation of the permission.
12. APS reserves all rights not specifically granted herein.
13. This document, including the CCC Billing and Payment Terms and Conditions, shall be the entire agreement between the parties relating to the subject matter hereof.

Other Terms and Conditions

Questions? customercare@copyright.com or +1-855-239-3415 (toll free in the US) or +1-978-646-2777.

**AIP PUBLISHING LLC LICENSE
TERMS AND CONDITIONS**

Sep 23, 2015

All payments must be made in full to CCC. For payment instructions, please see information listed at the bottom of this form.

| | |
|-------------------------------------|---|
| License Number | 3714841123268 |
| Order Date | Sep 23, 2015 |
| Publisher | AIP Publishing LLC |
| Publication | Applied Physics Letters |
| Article Title | Ellipticity dependence of 400 nm-driven high harmonic generation |
| Author | Sabih D. Khan, Yan Cheng, Max Möller, et al. |
| Online Publication Date | Oct 18, 2011 |
| Volume number | 99 |
| Issue number | 16 |
| Type of Use | Thesis/Dissertation |
| Requestor type | Author (original article) |
| Format | Electronic |
| Portion | Excerpt (> 800 words) |
| Will you be translating? | No |
| Title of your thesis / dissertation | ATTOSECOND TRANSIENT ABSORPTION SPECTROSCOPY OF ATOMS AND MOLECULES |
| Expected completion date | Dec 2015 |
| Estimated size (number of pages) | 150 |
| Total | 0.00 USD |

Terms and Conditions

AIP Publishing LLC -- Terms and Conditions: Permissions Uses

AIP Publishing LLC ("AIPP") hereby grants to you the non-exclusive right and license to use and/or distribute the Material according to the use specified in your order, on a one-time basis, for the specified term, with a maximum distribution equal to the number that you have ordered. Any links or other content accompanying the Material are not the subject of this license.

1. You agree to include the following copyright and permission notice with the reproduction of the Material: "Reprinted with permission from [FULL CITATION]. Copyright [PUBLICATION YEAR], AIP Publishing LLC." For an article, the copyright and permission notice must be printed on the first page of the article or book chapter. For photographs, covers, or tables, the copyright and permission notice may appear with the Material, in a footnote, or in the reference list.
2. If you have licensed reuse of a figure, photograph, cover, or table, it is your responsibility to ensure that the material is original to AIPP and does not contain the copyright of another entity, and that the copyright notice of the figure, photograph, cover, or table does not indicate that it was reprinted by AIPP, with permission, from another source. Under no circumstances does AIPP, purport or intend to grant permission to reuse material to which it does not hold copyright.
3. You may not alter or modify the Material in any manner. You may translate the Material into another language only if you have licensed translation rights. You may not use the Material for promotional purposes. AIPP reserves all rights not specifically granted herein.

4. The foregoing license shall not take effect unless and until AIPP or its agent, Copyright Clearance Center, receives the Payment in accordance with Copyright Clearance Center Billing and Payment Terms and Conditions, which are incorporated herein by reference.
5. AIPP or the Copyright Clearance Center may, within two business days of granting this license, revoke the license for any reason whatsoever, with a full refund payable to you. Should you violate the terms of this license at any time, AIPP, AIP Publishing LLC, or Copyright Clearance Center may revoke the license with no refund to you. Notice of such revocation will be made using the contact information provided by you. Failure to receive such notice will not nullify the revocation.
6. AIPP makes no representations or warranties with respect to the Material. You agree to indemnify and hold harmless AIPP, AIP Publishing LLC, and their officers, directors, employees or agents from and against any and all claims arising out of your use of the Material other than as specifically authorized herein.
7. The permission granted herein is personal to you and is not transferable or assignable without the prior written permission of AIPP. This license may not be amended except in a writing signed by the party to be charged.
8. If purchase orders, acknowledgments or check endorsements are issued on any forms containing terms and conditions which are inconsistent with these provisions, such inconsistent terms and conditions shall be of no force and effect. This document, including the CCC Billing and Payment Terms and Conditions, shall be the entire agreement between the parties relating to the subject matter hereof.

This Agreement shall be governed by and construed in accordance with the laws of the State of New York. Both parties hereby submit to the jurisdiction of the courts of New York County for purposes of resolving any disputes that may arise hereunder.

Questions? customercare@copyright.com or +1-855-239-3415 (toll free in the US) or +1-978-646-2777.



Title: Coherent phase-matched VUV generation by field-controlled bound states

Author: Michael Chini, Xiaowei Wang, Yan Cheng, He Wang, Yi Wu, Eric Cunningham

Logged in as:
Yan Cheng

[LOGOUT](#)

Publication: Nature Photonics

Publisher: Nature Publishing Group

Date: May 11, 2014

Copyright © 2014, Rights Managed by Nature Publishing Group

Author Request

If you are the author of this content (or his/her designated agent) please read the following. If you are not the author of this content, please click the Back button and select an alternative [Requestor Type](#) to obtain a quick price or to place an order.

Ownership of copyright in the article remains with the Authors, and provided that, when reproducing the Contribution or extracts from it, the Authors acknowledge first and reference publication in the Journal, the Authors retain the following non-exclusive rights:

- a) To reproduce the Contribution in whole or in part in any printed volume (book or thesis) of which they are the author(s).
- b) They and any academic institution where they work at the time may reproduce the Contribution for the purpose of course teaching.
- c) To reuse figures or tables created by them and contained in the Contribution in other works created by them.
- d) To post a copy of the Contribution as accepted for publication after peer review (in Word or Text format) on the Author's own web site, or the Author's institutional repository, or the Author's funding body's archive, six months after publication of the printed or online edition of the Journal, provided that they also link to the Journal article on NPG's web site (eg through the DOI).

NPG encourages the self-archiving of the accepted version of your manuscript in your funding agency's or institution's repository, six months after publication. This policy complements the recently announced policies of the US National Institutes of Health, Wellcome Trust and other research funding bodies around the world. NPG recognises the efforts of funding bodies to increase access to the research they fund, and we strongly encourage authors to participate in such efforts.

Authors wishing to use the published version of their article for promotional use or on a web site must request in the normal way.

If you require further assistance please read NPG's online [author reuse guidelines](#).

For full paper portion: Authors of original research papers published by NPG are encouraged to submit the author's version of the accepted, peer-reviewed manuscript to their relevant funding body's archive, for release six months after publication. In addition, authors are encouraged to archive their version of the manuscript in their institution's repositories (as well as their personal Web sites), also six months after original publication.

v2.0



Title: Sub-cycle Oscillations in Virtual States Brought to Light
Author: Michael Chini, Xiaowei Wang, Yan Cheng, Yi Wu, Di Zhao et al.
Publication: Scientific Reports
Publisher: Nature Publishing Group
Date: Jan 22, 2013

Logged in as:
Yan Cheng

[LOGOUT](#)

Copyright © 2013, Rights Managed by Nature Publishing Group

Creative Commons

The request you have made is considered to be non-commercial/educational. As the article you have requested has been distributed under a Creative Commons license (Attribution-Noncommercial), you may reuse this material for non-commercial/educational purposes without obtaining additional permission from Nature Publishing Group, providing that the author and the original source of publication are fully acknowledged (please see the article itself for the license version number). You may reuse this material without obtaining permission from Nature Publishing Group, providing that the author and the original source of publication are fully acknowledged, as per the terms of the license. For license terms, please see <http://creativecommons.org/>

[BACK](#)

[CLOSE WINDOW](#)

LIST OF REFERENCES

1. P. B. Corkum, and Z. Chang, "The Attosecond Revolution," *Opt. Photon. News* **19**, 24-29 (2008).
2. P. B. Corkum, and F. Krausz, "Attosecond science," *Nat Phys* **3**, 381-387 (2007).
3. M. Dantus, M. J. Rosker, and A. H. Zewail, "Real-Time Femtosecond Probing of Transition-States in Chemical-Reactions," *J Chem Phys* **87**, 2395-2397 (1987).
4. F. Krausz, and M. Ivanov, "Attosecond physics," *Rev Mod Phys* **81**, 163-234 (2009).
5. H. Wang, M. Chini, S. Y. Chen, C. H. Zhang, F. He, Y. Cheng, Y. Wu, U. Thumm, and Z. H. Chang, "Attosecond Time-Resolved Autoionization of Argon," *Phys Rev Lett* **105** (2010).
6. M. Ferray, A. Lhuillier, X. F. Li, L. A. Lompre, G. Mainfray, and C. Manus, "Multiple-Harmonic Conversion of 1064-Nm Radiation in Rare-Gases," *Journal of Physics B-Atomic Molecular and Optical Physics* **21**, L31-L35 (1988).
7. C. Lynga, M. B. Gaarde, C. Delfin, M. Bellini, T. W. Hansch, A. L'Huillier, and C. G. Wahlstrom, "Temporal coherence of high-order harmonics," *Phys Rev A* **60**, 4823-4830 (1999).
8. P. B. Corkum, "Plasma Perspective on Strong-Field Multiphoton Ionization," *Physical Review Letters* **71**, 1994-1997 (1993).
9. L. V. Keldysh, "Ionization in the Field of a Strong Electromagnetic Wave," *Soviet Physics JETP* **20**, 1307 (1965).
10. Z. Chang, *Fundamentals of Attosecond Optics* (2011 by CRC Press).
11. N. Milosevic, A. Scrinzi, and T. Brabec, "Numerical characterization of high harmonic attosecond pulses," *Phys Rev Lett* **88** (2002).

12. J. Itatani, J. Levesque, D. Zeidler, H. Niikura, H. Pepin, J. C. Kieffer, P. B. Corkum, and D. M. Villeneuve, "Tomographic imaging of molecular orbitals," *Nature* **432**, 867-871 (2004).
13. D. Shafir, Y. Mairesse, D. M. Villeneuve, P. B. Corkum, and N. Dudovich, "Atomic wavefunctions probed through strong-field light-matter interaction," *Nat Phys* **5**, 412-416 (2009).
14. O. Smirnova, Y. Mairesse, S. Patchkovskii, N. Dudovich, D. Villeneuve, P. Corkum, and M. Y. Ivanov, "High harmonic interferometry of multi-electron dynamics in molecules," *Nature* **460**, 972-977 (2009).
15. D. Strickland, and G. Mourou, "Compression of Amplified Chirped Optical Pulses," *Opt Commun* **56**, 219-221 (1985).
16. J. Feng, J. Nasiatka, M. Hertlein, B. Rude, and H. Padmore, "Compact cryogenically cooled Ti:Sapphire dual multi-kilohertz amplifiers for synchrotron radiation ultra-fast x-ray applications," *Review of Scientific Instruments* **84** (2013).
17. M. Nisoli, S. DeSilvestri, O. Svelto, R. Szipöcs, K. Ferencz, C. Spielmann, S. Sartania, and F. Krausz, "Compression of high-energy laser pulses below 5 fs," *Opt Lett* **22**, 522-524 (1997).
18. R. Szipöcs, K. Ferencz, C. Spielmann, and F. Krausz, "Chirped multilayer coatings for broadband dispersion control in femtosecond lasers," *Opt. Lett.* **19**, 201-203 (1994).
19. R. W. Boyd, *Nonlinear Optics, Third Edition* (Academic Press, 2008).
20. S. D. Khan, Y. Cheng, M. Moller, K. Zhao, B. Z. Zhao, M. Chini, G. G. Paulus, and Z. H. Chang, "Ellipticity dependence of 400 nm-driven high harmonic generation," *Appl Phys Lett* **99** (2011).

21. M. Moller, Y. Cheng, S. D. Khan, B. Z. Zhao, K. Zhao, M. Chini, G. G. Paulus, and Z. H. Chang, "Dependence of high-order-harmonic-generation yield on driving-laser ellipticity," *Phys Rev A* **86** (2012).
22. B. Shan, S. Ghimire, and Z. Chang, "Generation of the attosecond extreme ultraviolet supercontinuum by a polarization," *J Mod Optic* **52**, 277-283 (2005).
23. G. Sansone, E. Benedetti, F. Calegari, C. Vozzi, L. Avaldi, R. Flammini, L. Poletto, P. Villoresi, C. Altucci, R. Velotta, S. Stagira, S. De Silvestri, and M. Nisoli, "Isolated single-cycle attosecond pulses," *Science* **314**, 443-446 (2006).
24. H. Mashiko, S. Gilbertson, C. Q. Li, S. D. Khan, M. M. Shakya, E. Moon, and Z. H. Chang, "Double optical gating of high-order harmonic generation with carrier-envelope phase stabilized lasers," *Physical Review Letters* **100** (2008).
25. O. S. Yu, M. Kaku, A. Suda, F. Kannari, and K. Midorikawa, "Generation of extreme ultraviolet continuum radiation driven by a sub-10-fs two-color field," *Opt Express* **14**, 7230-7237 (2006).
26. S. Gibertson, "Double Optical Gating," PhD Dissertation (2010).
27. X. M. Feng, S. Gilbertson, H. Mashiko, H. Wang, S. D. Khan, M. Chini, Y. Wu, K. Zhao, and Z. H. Chang, "Generation of Isolated Attosecond Pulses with 20 to 28 Femtosecond Lasers," *Phys Rev Lett* **103** (2009).
28. M. Chini, H. Mashiko, H. Wang, S. Y. Chen, C. X. Yun, S. Scott, S. Gilbertson, and Z. H. Chang, "Delay control in attosecond pump-probe experiments," *Optics Express* **17**, 21459-21464 (2009).

29. X. W. Wang, M. Chini, Y. Cheng, Y. Wu, and Z. H. Chang, "In situ calibration of an extreme ultraviolet spectrometer for attosecond transient absorption experiments," *Applied Optics* **52**, 323-329 (2013).
30. J. L. Krause, K. J. Schafer, and K. C. Kulander, "High-Order Harmonic-Generation from Atoms and Ions in the High-Intensity Regime," *Phys Rev Lett* **68**, 3535-3538 (1992).
31. P. B. Corkum, N. H. Burnett, and M. Y. Ivanov, "Subfemtosecond Pulses," *Opt Lett* **19**, 1870-1872 (1994).
32. J. Mauritsson, P. Johnsson, E. Gustafsson, A. L'Huillier, K. J. Schafer, and M. B. Gaarde, "Attosecond pulse trains generated using two color laser fields," *Phys Rev Lett* **97** (2006).
33. R. E. F. Silva, P. Riviere, and F. Martin, "Autoionizing decay of H-2 doubly excited states by using xuv-pump-infrared-probe schemes with trains of attosecond pulses," *Phys Rev A* **85** (2012).
34. E. Goulielmakis, Z. H. Loh, A. Wirth, R. Santra, N. Rohringer, V. S. Yakovlev, S. Zherebtsov, T. Pfeifer, A. M. Azzeer, M. F. Kling, S. R. Leone, and F. Krausz, "Real-time observation of valence electron motion," *Nature* **466**, 739-U737 (2010).
35. M. Chini, B. Z. Zhao, H. Wang, Y. Cheng, S. X. Hu, and Z. H. Chang, "Subcycle ac Stark Shift of Helium Excited States Probed with Isolated Attosecond Pulses," *Phys Rev Lett* **109** (2012).
36. M. Holler, F. Schapper, L. Gallmann, and U. Keller, "Attosecond Electron Wave-Packet Interference Observed by Transient Absorption," *Phys Rev Lett* **106** (2011).

37. Z. H. Loh, M. Khalil, R. E. Correa, and S. R. Leone, "A tabletop femtosecond time-resolved soft x-ray transient absorption spectrometer," *Review of Scientific Instruments* **79** (2008).
38. M. Fiess, M. Schultze, E. Goulielmakis, B. Dennhardt, J. Gagnon, M. Hofstetter, R. Kienberger, and F. Krausz, "Versatile apparatus for attosecond metrology and spectroscopy," *Review of Scientific Instruments* **81** (2010).
39. W. Schwanda, K. Eidmann, and M. C. Richardson, "Characterization of a Flat-Field Grazing-Incidence XUV Spectrometer," *Journal of X-ray science and technology* **4**, 8-17 (1993).
40. N. Nakano, H. Kuroda, T. Kita, and T. Harada, "Development of a Flat-Field Grazing-Incidence Xuv Spectrometer and Its Application in Picosecond Xuv Spectroscopy," *Appl Optics* **23**, 2386-2392 (1984).
41. B. Blagojevic, E. O. Le Bigot, K. Fahy, A. Aguilar, K. Makonyi, E. Takacs, J. N. Tan, J. M. Pomeroy, J. H. Burnett, J. D. Gillaspay, and J. R. Roberts, "A high efficiency ultrahigh vacuum compatible flat field spectrometer for extreme ultraviolet wavelengths," *Review of Scientific Instruments* **76** (2005).
42. J. Park, G. V. Brown, M. B. Schneider, H. A. Baldis, P. Beiersdorfer, K. V. Cone, R. L. Kelley, C. A. Kilbourne, E. W. Magee, M. J. May, and F. S. Porter, "Calibration of a flat field soft x-ray grating spectrometer for laser produced plasmas," *Review of Scientific Instruments* **81** (2010).
43. "www.zemax.com."
44. "www.cxro.lbl.gov."

45. R. P. Madden, D. L. Ederer, and K. Codling, "Resonances in the Photo-ionization Continuum of Ar i (20-150 eV)," *Physical Review* **177**, 136-151 (1969).
46. U. Fano, "Effects of Configuration Interaction on Intensities and Phase Shifts," *Physical Review* **124**, 1866-1878 (1961).
47. M. Žitnik, A. Stanič, K. Bučar, J. G. Lambourne, F. Penent, R. I. Hall, and P. Lablanquie, "Lifetimes of n 1 P states in helium," *Journal of Physics B: Atomic, Molecular and Optical Physics* **36**, 4175 (2003).
48. M. Chini, X. W. Wang, Y. Cheng, Y. Wu, D. Zhao, D. A. Telnov, S. I. Chu, and Z. H. Chang, "Sub-cycle Oscillations in Virtual States Brought to Light," *Sci Rep-Uk* **3** (2013).
49. "<https://en.wikipedia.org/wiki/Absorbance>."
50. D. R. Smith, J. B. Pendry, and M. C. K. Wiltshire, "Metamaterials and negative refractive index," *Science* **305**, 788-792 (2004).
51. M. Fleischhauer, A. Imamoglu, and J. P. Marangos, "Electromagnetically induced transparency: Optics in coherent media," *Rev Mod Phys* **77**, 633-673 (2005).
52. F. Hao, Y. Sonnefraud, P. Van Dorpe, S. A. Maier, N. J. Halas, and P. Nordlander, "Symmetry Breaking in Plasmonic Nanocavities: Subradiant LSPR Sensing and a Tunable Fano Resonance," *Nano Lett* **8**, 3983-3988 (2008).
53. U. Fano, and J. W. Cooper, "Spectral Distribution of Atomic Oscillator Strengths," *Rev Mod Phys* **40**, 441-+ (1968).
54. Z. H. Loh, C. H. Greene, and S. R. Leone, "Femtosecond induced transparency and absorption in the extreme ultraviolet by coherent coupling of the He 2s2p (P-1(o)) and 2p(2) (S-1(e)) double excitation states with 800 nm light," *Chem Phys* **350**, 7-13 (2008).

55. T. E. Glover, M. P. Hertlein, S. H. Southworth, T. K. Allison, J. van Tilborg, E. P. Kanter, B. Krassig, H. R. Varma, B. Rude, R. Santra, A. Belkacem, and L. Young, "Controlling X-rays with light," *Nat Phys* **6**, 69-U65 (2010).
56. J. Mauritsson, T. Remetter, M. Swoboda, K. Klunder, A. L'Huillier, K. J. Schafer, O. Ghafur, F. Kelkensberg, W. Siu, P. Johnsson, M. J. J. Vrakking, I. Znakovskaya, T. Uphues, S. Zherebtsov, M. F. Kling, F. Lepine, E. Benedetti, F. Ferrari, G. Sansone, and M. Nisoli, "Attosecond Electron Spectroscopy Using a Novel Interferometric Pump-Probe Technique," *Phys Rev Lett* **105** (2010).
57. D. G. W. F, "Springer Handbook of Atomic, Molecular and Optical Physics."
58. X. M. Tong, and N. Toshima, "Controlling atomic structures and photoabsorption processes by an infrared laser," *Phys Rev A* **81** (2010).
59. M. B. Gaarde, C. Buth, J. L. Tate, and K. J. Schafer, "Transient absorption and reshaping of ultrafast XUV light by laser-dressed helium," *Phys Rev A* **83**, 013419 (2011).
60. S. H. Chen, K. J. Schafer, and M. B. Gaarde, "Transient absorption of attosecond pulse trains by laser-dressed helium," *Opt Lett* **37**, 2211-2213 (2012).
61. S. Pabst, A. Sytcheva, A. Moulet, A. Wirth, E. Goulielmakis, and R. Santra, "Theory of attosecond transient-absorption spectroscopy of krypton for overlapping pump and probe pulses," *Phys Rev A* **86** (2012).
62. S. H. Chen, M. Wu, M. B. Gaarde, and K. J. Schafer, "Quantum interference in attosecond transient absorption of laser-dressed helium atoms," *Phys Rev A* **87** (2013).
63. X. W. Wang, M. Chini, Y. Cheng, Y. Wu, X. M. Tong, and Z. H. Chang, "Subcycle laser control and quantum interferences in attosecond photoabsorption of neon," *Phys Rev A* **87** (2013).

64. M. F. Kling, and M. J. J. Vrakking, "Attosecond electron dynamics," *Annu Rev Phys Chem* **59**, 463-492 (2008).
65. E. Goulielmakis, V. S. Yakovlev, A. L. Cavalieri, M. Uiberacker, V. Pervak, A. Apolonski, R. Kienberger, U. Kleineberg, and F. Krausz, "Attosecond control and measurement: Lightwave electronics," *Science* **317**, 769-775 (2007).
66. W. C. Chu, and C. D. Lin, "Photoabsorption of attosecond XUV light pulses by two strongly laser-coupled autoionizing states," *Phys Rev A* **85** (2012).
67. W. C. Chu, S. F. Zhao, and C. D. Lin, "Laser-assisted-autoionization dynamics of helium resonances with single attosecond pulses," *Phys Rev A* **84** (2011).
68. A. N. Pfeiffer, and S. R. Leone, "Transmission of an isolated attosecond pulse in a strong-field dressed atom," *Phys Rev A* **85** (2012).
69. P. Lambropoulos, and P. Zoller, "Autoionizing States in Strong Laser Fields," *Phys Rev A* **24**, 379-397 (1981).
70. M. Hentschel, R. Kienberger, C. Spielmann, G. A. Reider, N. Milosevic, T. Brabec, P. Corkum, U. Heinzmann, M. Drescher, and F. Krausz, "Attosecond metrology," *Nature* **414**, 509-513 (2001).
71. M. Wickenhauser, J. Burgdorfer, F. Krausz, and M. Drescher, "Time resolved Fano resonances," *Phys Rev Lett* **94** (2005).
72. X. M. Tong, and C. D. Lin, "Double photoexcitation of He atoms by attosecond xuv pulses in the presence of intense few-cycle infrared lasers," *Phys Rev A* **71** (2005).
73. Z. X. Zhao, and C. D. Lin, "Theory of laser-assisted autoionization by attosecond light pulses," *Phys Rev A* **71** (2005).

74. S. Gilbertson, M. Chini, X. M. Feng, S. Khan, Y. Wu, and Z. H. Chang, "Monitoring and Controlling the Electron Dynamics in Helium with Isolated Attosecond Pulses," *Phys Rev Lett* **105** (2010).
75. J. W. Mcconkey, and J. A. Preston, "Autoionizing States in Argon," *J Phys B-at Mol Opt* **6**, L138-L141 (1973).
76. S. I. Themelis, P. Lambropoulos, and M. Meyer, "Ionization dynamics in double resonance involving autoionizing states in helium: the effect of pulse shapes," *J Phys B-at Mol Opt* **37**, 4281-4293 (2004).
77. M. Chini, X. W. Wang, Y. Cheng, and Z. H. Chang, "Resonance effects and quantum beats in attosecond transient absorption of helium," *J Phys B-at Mol Opt* **47** (2014).
78. V. L. Carter, and R. D. Hudson, "Absorption spectra of krypton and xenon in their regions of autoionization," *J. Opt. Soc. Am.* **63**, 733-735 (1973).
79. Y. Cheng, M. Chini, X.-M. Tong, A. Chew, J. Biedermann, Y. Wu, E. Cunningham, and Z. Chang, "Quantum Beats in Attosecond Transient Absorption of Krypton Autoionizing States," in *CLEO: QELS_Fundamental Science*(Optical Society of America, 2015), p. FTh3C. 3.
80. D. C. Yost, T. R. Schibli, J. Ye, J. L. Tate, J. Hostetter, M. B. Gaarde, and K. J. Schafer, "Vacuum-ultraviolet frequency combs from below-threshold harmonics," *Nat Phys* **5**, 815-820 (2009).
81. M. Krebs, S. Hadrich, S. Demmler, J. Rothhardt, A. Zair, L. Chipperfield, J. Limpert, and A. Tunnermann, "Towards isolated attosecond pulses at megahertz repetition rates," *Nat Photonics* **7**, 555-559 (2013).

82. T. Udem, R. Holzwarth, and T. W. Hansch, "Optical frequency metrology," *Nature* **416**, 233-237 (2002).
83. S. Kim, J. H. Jin, Y. J. Kim, I. Y. Park, Y. Kim, and S. W. Kim, "High-harmonic generation by resonant plasmon field enhancement," *Nature* **453**, 757-760 (2008).
84. I. Y. Park, S. Kim, J. Choi, D. H. Lee, Y. J. Kim, M. F. Kling, M. I. Stockman, and S. W. Kim, "Plasmonic generation of ultrashort extreme-ultraviolet light pulses," *Nat Photonics* **5**, 678-682 (2011).
85. M. Sivi, M. Duwe, B. Abel, and C. Ropers, "Extreme-ultraviolet light generation in plasmonic nanostructures," *Nat Phys* **9**, 304-309 (2013).
86. E. P. Power, A. M. March, F. Catoire, E. Sistrunk, K. Krushelnick, P. Agostini, and L. F. DiMauro, "XFROG phase measurement of threshold harmonics in a Keldysh-scaled system," *Nat Photonics* **4**, 352-356 (2010).
87. T. J. Hammond, A. K. Mills, and D. J. Jones, "Near-threshold harmonics from a femtosecond enhancement cavity-based EUV source: effects of multiple quantum pathways on spatial profile and yield," *Opt Express* **19**, 24871-24883 (2011).
88. D. Shafir, H. Soifer, C. Vozzi, A. S. Johnson, A. Hartung, Z. Dube, D. M. Villeneuve, P. B. Corkum, N. Dudovich, and A. Staudte, "Trajectory-Resolved Coulomb Focusing in Tunnel Ionization of Atoms with Intense, Elliptically Polarized Laser Pulses," *Phys Rev Lett* **111** (2013).
89. J. A. Hostetter, J. L. Tate, K. J. Schafer, and M. B. Gaarde, "Semiclassical approaches to below-threshold harmonics," *Phys Rev A* **82** (2010).
90. A. Lhuillier, P. Balcou, and L. A. Lompre, "Coherence and Resonance Effects in High-Order Harmonic-Generation," *Phys Rev Lett* **68**, 166-169 (1992).

91. E. S. Toma, P. Antoine, A. de Bohan, and H. G. Muller, "Resonance-enhanced high-harmonic generation," *J Phys B-at Mol Opt* **32**, 5843-5852 (1999).
92. P. Ackermann, H. Munch, and T. Halfmann, "Resonantly-enhanced harmonic generation in Argon," *Opt Express* **20**, 13824-13832 (2012).
93. J. K. Crane, M. D. Perry, D. Strickland, S. Herman, and R. W. Falcone, "Coherent and Incoherent Xuv Emission in Helium and Neon, Laser-Driven Plasmas," *Ieee T Plasma Sci* **21**, 82-89 (1993).
94. E. Mevel, P. Breger, R. Trainham, G. Petite, P. Agostini, A. Migus, J. P. Chambaret, and A. Antonetti, "Atoms in Strong Optical-Fields - Evolution from Multiphoton to Tunnel Ionization," *Phys Rev Lett* **70**, 406-409 (1993).
95. M. Chini, X. W. Wang, Y. Cheng, H. Wang, Y. Wu, E. Cunningham, P. C. Li, J. Heslar, D. A. Telnov, S. I. Chu, and Z. H. Chang, "Coherent phase-matched VUV generation by field-controlled bound states," *Nat Photonics* **8**, 437-441 (2014).
96. I. J. Sola, E. Mevel, L. Elouga, E. Constant, V. Strelkov, L. Poletto, P. Villoresi, E. Benedetti, J. P. Caumes, S. Stagira, C. Vozzi, G. Sansone, and M. Nisoli, "Controlling attosecond electron dynamics by phase-stabilized polarization gating," *Nat Phys* **2**, 319-322 (2006).
97. T. Popmintchev, M. C. Chen, A. Bahabad, M. Gerrity, P. Sidorenko, O. Cohen, I. P. Christov, M. M. Murnane, and H. C. Kapteyn, "Phase matching of high harmonic generation in the soft and hard X-ray regions of the spectrum," *P Natl Acad Sci USA* **106**, 10516-10521 (2009).
98. M. B. Gaarde, J. L. Tate, and K. J. Schafer, "Macroscopic aspects of attosecond pulse generation," *J Phys B-at Mol Opt* **41** (2008).

99. E. Constant, D. Garzella, P. Breger, E. Mevel, C. Dorrer, C. Le Blanc, F. Salin, and P. Agostini, "Optimizing high harmonic generation in absorbing gases: Model and experiment," *Phys Rev Lett* **82**, 1668-1671 (1999).
100. H. Soifer, P. Botheron, D. Shafir, A. Diner, O. Raz, B. D. Bruner, Y. Mairesse, B. Pons, and N. Dudovich, "Near-Threshold High-Order Harmonic Spectroscopy with Aligned Molecules," *Phys Rev Lett* **105** (2010).
101. A. Cingoz, D. C. Yost, T. K. Allison, A. Ruehl, M. E. Fermann, I. Hartl, and J. Ye, "Direct frequency comb spectroscopy in the extreme ultraviolet," *Nature* **482**, 68-71 (2012).
102. R. L. Sandberg, A. Paul, D. A. Raymondson, S. Hadrich, D. M. Gaudiosi, J. Holtsnider, R. I. Tobey, O. Cohen, M. M. Murnane, H. C. Kapteyn, C. G. Song, J. W. Miao, Y. W. Liu, and F. Salmassi, "Lensless diffractive imaging using tabletop coherent high-harmonic soft-x-ray beams," *Phys Rev Lett* **99** (2007).
103. M. I. Stockman, M. F. Kling, U. Kleineberg, and F. Krausz, "Attosecond nanoplasmonic-field microscope," *Nat Photon* **1**, 539-544 (2007).
104. S. H. Chew, F. Sussmann, C. Spath, A. Wirth, J. Schmidt, S. Zherebtsov, A. Guggenmos, A. Oelsner, N. Weber, J. Kapaldo, A. Gliserin, M. I. Stockman, M. F. Kling, and U. Kleineberg, "Time-of-flight-photoelectron emission microscopy on plasmonic structures using attosecond extreme ultraviolet pulses," *Appl Phys Lett* **100** (2012).
105. M. N. Miranda, P. B. Oliveira, L. M. Bernardo, F. X. Kärtner, and H. M. Crespo, "Space-time focusing of phase-stabilized nanojoule-level 2.5-cycle pulses to peak intensities $\sim 3 \times 10^{13}$ W/cm² at 80 MHz," in *CLEO/Europe and EQEC 2009 Conference Digest* (Optical Society of America, Munich, 2009), p. CF1_2.

106. F. Lepine, M. Y. Ivanov, and M. J. J. Vrakking, "Attosecond molecular dynamics: fact or fiction?," *Nat Photonics* **8**, 195-204 (2014).
107. F. Lepine, G. Sansone, and M. J. J. Vrakking, "Molecular applications of attosecond laser pulses," *Chem Phys Lett* **578**, 1-14 (2013).
108. P. Ranitovic, C. W. Hogle, P. Riviere, A. Palacios, X. M. Tong, N. Toshima, A. Gonzalez-Castrillo, L. Martin, F. Martin, M. M. Murnane, and H. Kapteyn, "Attosecond vacuum UV coherent control of molecular dynamics," *P Natl Acad Sci USA* **111**, 912-917 (2014).
109. G. Sansone, F. Kelkensberg, J. F. Perez-Torres, F. Morales, M. F. Kling, W. Siu, O. Ghafur, P. Johnsson, M. Swoboda, E. Benedetti, F. Ferrari, F. Lepine, J. L. Sanz-Vicario, S. Zherebtsov, I. Znakovskaya, A. L'Huillier, M. Y. Ivanov, M. Nisoli, F. Martin, and M. J. J. Vrakking, "Electron localization following attosecond molecular photoionization," *Nature* **465**, 763-U763 (2010).
110. S. H. Chen, M. J. Bell, A. R. Beck, H. Mashiko, M. X. Wu, A. N. Pfeiffer, M. B. Gaarde, D. M. Neumark, S. R. Leone, and K. J. Schafer, "Light-induced states in attosecond transient absorption spectra of laser-dressed helium," *Phys Rev A* **86** (2012).
111. M. Chini, K. Zhao, and Z. H. Chang, "The generation, characterization and applications of broadband isolated attosecond pulses," *Nat Photonics* **8**, 178-186 (2014).
112. C. Ott, A. Kaldun, L. Argenti, P. Raith, K. Meyer, M. Laux, Y. Zhang, A. Blattermann, S. Hagstotz, T. Ding, R. Heck, J. Madronero, F. Martin, and T. Pfeifer, "Reconstruction and control of a time-dependent two-electron wave packet," *Nature* **516**, 374-378 (2014).
113. M. Schultze, E. M. Bothschafter, A. Sommer, S. Holzner, W. Schweinberger, M. Fiess, M. Hofstetter, R. Kienberger, V. Apalkov, V. S. Yakovlev, M. I. Stockman, and F.

- Krausz, "Controlling dielectrics with the electric field of light," *Nature* **493**, 75-78 (2013).
114. X. Wang, M. Chini, Y. Cheng, Y. Wu, and Z. Chang, "In situ calibration of an extreme ultraviolet spectrometer for attosecond transient absorption experiments," *Appl Optics* **52**, 323-329 (2013).
115. S. T. E, "Potential-Energy Curves for Molecular Hydrogen and Its Ions," *Atomic Data* **2**, 119 (1971).
116. Z. P. Zhong, W. H. Zhang, K. Z. Xu, R. F. Feng, and J. M. Li, "Experimental and theoretical study of photoabsorption spectra of molecular hydrogen in the energy region 11-19 eV," *Phys Rev A* **60**, 236-245 (1999).
117. C. H. B. Cruz, J. P. Gordon, P. C. Becker, R. L. Fork, and C. V. Shank, "Dynamics of Spectral Hole Burning," *Ieee J Quantum Elect* **24**, 261-266 (1988).
118. S. H. Autler, and C. H. Townes, "Stark Effect in Rapidly Varying Fields," *Physical Review* **100**, 703-722 (1955).
119. J. L. Sanz-Vicario, H. Bachau, and F. Martin, "Time-dependent theoretical description of molecular autoionization produced by femtosecond xuv laser pulses," *Phys Rev A* **73** (2006).
120. A. Palacios, H. Bachau, and F. Martin, "Excitation and ionization of molecular hydrogen by ultrashort vuv laser pulses," *Phys Rev A* **75** (2007).
121. "Private communication from Dr. Fernando Martin."
122. A. Assion, T. Baumert, M. Bergt, T. Brixner, B. Kiefer, V. Seyfried, M. Strehle, and G. Gerber, "Control of chemical reactions by feedback-optimized phase-shaped femtosecond laser pulses," *Science* **282**, 919-922 (1998).

123. E. Gustafsson, T. Ruchon, M. Swoboda, T. Remetter, E. Pourtal, R. Lopez-Martens, P. Balcou, and A. L'Huillier, "Broadband attosecond pulse shaping," *Opt Lett* **32**, 1353-1355 (2007).
124. C. Ott, A. Kaldun, P. Raith, K. Meyer, M. Laux, J. Evers, C. H. Keitel, C. H. Greene, and T. Pfeifer, "Lorentz Meets Fano in Spectral Line Shapes: A Universal Phase and Its Laser Control," *Science* **340**, 716-720 (2013).